Estimation of cutting feasibility on the example of Põhja-Kiviõli II mine

Master's thesis

Student: Siim Roov
Student ID: 242317LARM
Supervisor: Bruno Grafe, PhD
Co-supervisor: Sander Kanter, MSc
Study program: Earth Systems and Geotechnology

Tallinn 2026

Declaration

I hereby declare that I have compiled the paper independently and all works, important standpoints and data by other authors have been properly referenced and the same paper has not previously been presented for grading.

Author: Siim Roov

[Signature, date]

The paper conforms to requirements in force.

Supervisor: Bruno Grafe

[Signature, date]

Permitted to the defence.

Chairman of the Defence Committee: Olle Hints

[Signature, date]

Table of contents

Abstract

This thesis evaluates the applicability of a computational cutting model developed by Dr. Andreas Lemm for predicting surface miner productivity in Estonian limestones. The study stems from the need for more sustainable excavation methods, with a lower environmental and social impact. Surface miners offer an alternative to drilling and blasting, but their performance is strongly influenced by rock mechanical properties, rock mass structure, and operational conditions.

Field measurements were carried out at the Põhja-Kiviõli II mine on a Wirtgen 280 SMi surface miner, complemented by laboratory testing of UCS, BTS, elastic modulus, Poisson's ratio, and CERCHAR abrasivity. Mineralogical composition and equivalent quartz content were also determined using XRD/XRF. The rock showed significant variability between layers, with UCS ranging from 30 to over 100 MPa and generally low abrasivity (average CAI 0,42). Strong heterogeneity and anisotropy were observed.

Measured production rates ranged from 125 to 252 m^3/h. Initial model results overestimated specific energy consumption, but the modelling results improved after applying corrections for rock mass conditions and pick wear. However, deviations remained in certain layers due to heterogeneity and operational influences. The study concludes that while the Lemm model shows promise, additional research needs to be conducted. The model can be improved by implementing rock mass factor in the calculations.

Freesimise võimalikkuse hindamine Põhja-Kiviõli II karjääri näitel

Annotatsioon

See lõputöö hindab Dr. Andreal Lemmi loodud mudeli rakendatavust freeskombainide tootlikkuse hindamisel Eesti lubjakivide kaevandamisel. Töö vajadus tuleneb nõudlusest jätkusuutlikemate kaevandamismeetodite järele, millel oleks väiksem keskkonnamõju. Freeskombainid on alternatiiv puur- ja lõhketöödele, ent nende tootlikkus sõltub tugevalt kivimimehaanilistest parameetritest, massiivi omadustest ning töötingimustest.

Välitööd viidi läbi Põhja-Kiviõli II põlevkivikarjääris freeskombainil Wirtgen 280 SMi. Välitöid täiendasid laboratoorsed katsed, kus uuriti survetugevust (UCS), tõmbetugevust (BTS), elastusmoodulit, Poissoni tegurit and abrasiivsust CERCHAR katse meetodil. XRF ja XRD analüüside läbi uuriti ka kivimite mineraloogilist koostist ning arvutati kvartsi ekvivalentsisaldus. Eri kihtide lõikes varieerusid kivimi omadused märgatavalt – survetugevus oli vahemikus 30 kuni üle 100 MPa; abrasiivsus oli enamjaolt madal (keskmine CAI 0,42). Tulemustest oli näha selgelt kivimite heterogeensust ning anisotroopset käitumist.

Välitöödel mõõdetud tootlikkus jäi vahemikku 125 kuni 252 m^3/h. Esmased mudeldamise tulemused ülehindasid erienergiatarbimist, ent peale kivimimassiivi ning lõiketerade kulumisastme parandite rakendamist paranes tulemust oluliselt. Siiski oli mõningate kihtide puhul erisus mõõdetud ning mudeldatud tulemuste vahel, mis tulenes kivimi heterogeensusest ning freeskombaini enda tööst. Tööst järeldub, et esialgsed tulemused on paljulubavad, kuid selle kinnitamiseks oleks tarvis teha lisauuringuid. Mudelit saaks täiendada, lisades sinna kivimimasiivi omadusi arvestava teguri.

List of figures

List of tables

List of abbreviations

BTS	Brazilian tensile strength
CAI	CERCHAR abrasivity index
EM	Elastic modulus
EQV	Equivalent quartz value
GCP	Ground control point
HRC	Rockwell hardness
ISRM	International Society for Rock Mechanics
L/D	length to distance ratio
RQD	Rock quality designation
SM	surface miner
UCS	Uniaxial compressive strength
UPM	Ultrasonic pulse measurement
XRD	X-ray diffraction
XRF	X-ray fluorescence

1. Introduction

The construction material industry is of vital importance to the Estonian economy as a source for building materials for general construction and infrastructure development. In Estonia, the mineral resources mined are sand, gravel, limestone and dolostone. The latter two are the most important source of construction aggregates in the country (Kliimaministeerium, 2026).

While carbonate rocks are widely available in Northern Estonia, their quality is highly variable. The highest quality and most sought-after limestones for construction materials belong to the Lasnamäe Stage, which is mined in Harku and Väo deposits near Tallinn, and at the Aru-Lõuna quarry near Kunda. The deposits near the capital are of special importance, due to the large demand of high-quality limestone for infrastructure projects (Bauert et al., 2018).

Over time, the most accessible deposits for this limestone have gradually been depleting. Existing mines are running out of material and the development of new mines is difficult due to the urban sprawl of Tallinn, disqualifying many potential mine sites (Bauert et al., 2018; Kliimaministeerium, 2026). In other areas, mining is prohibited or limited due to environmental protection laws or the presence of cultural sites (Bauert et al., 2018). This forces miners towards less ideal deposits and using other technologies.

As outlined in document “General principles of Earth’s crust policy until 2050” (Kliimaministeerium, 2021), mineral resources should be managed sustainably, therefore existing deposits should be used to their fullest extent. This is often challenging to achieve, especially in quarries close to Tallinn, as the proximity of the city limits the technologies which can be used. For example, drilling and blasting might damage infrastructure, while hydraulic breakers generate significant noise and are disruptive to the local population.

This problem is addressed with the project Tem-TA143 “Construction Mineral Resources and Mineral Waste: Opportunities for Sustainable Mining and Circular Valorisation in Estonia”, funded by the Estonian Research Council. The project is carried out in collaboration between the Department of Geology and the Department of Civil Engineering and Architecture at Tallinn University of Technology. The aim is to investigate new methods and technologies to mine construction materials more sustainably and with reduced environmental and social, enabling the mining of deposits, in which traditional methods (drilling and blasting) are unsuitable.

Part of the project focuses on the applicability of mechanical excavation methods for construction aggregate production. One such technology is the surface miner, which offers a potential alternative for selective and controlled rock excavation. The evaluation of surface miner applicability can be carried out either through field trials or through predictive modelling based on rock mass and machine parameters. Since transporting heavy equipment into different mine sites is expensive, modelling the cutting performance would be a simpler and more economical option.

A comprehensive cutting model has been developed by Dr. Andreas Lemm, which could potentially be used to predict the performance of a surface miner in different limestone or dolostone quarries. The purpose of this thesis was to evaluate the applicability of this model in Estonian conditions, by comparing the results of real-world production rates of a surface miner working at the Põhja-Kiviõli II mine to the estimates calculated by the model.

The work consisted of 4 main parts (**Figure 1**) – field measurements of an active surface miner; laboratory testing of rock mechanical properties; cutting performance modelling by Dr. Andreas Lemm; and finally, comparison and analysis of the results. In addition, surface miner pick analysis was carried out. Based on the findings, suggestions were made on how to improve the model further, to better suit this application.

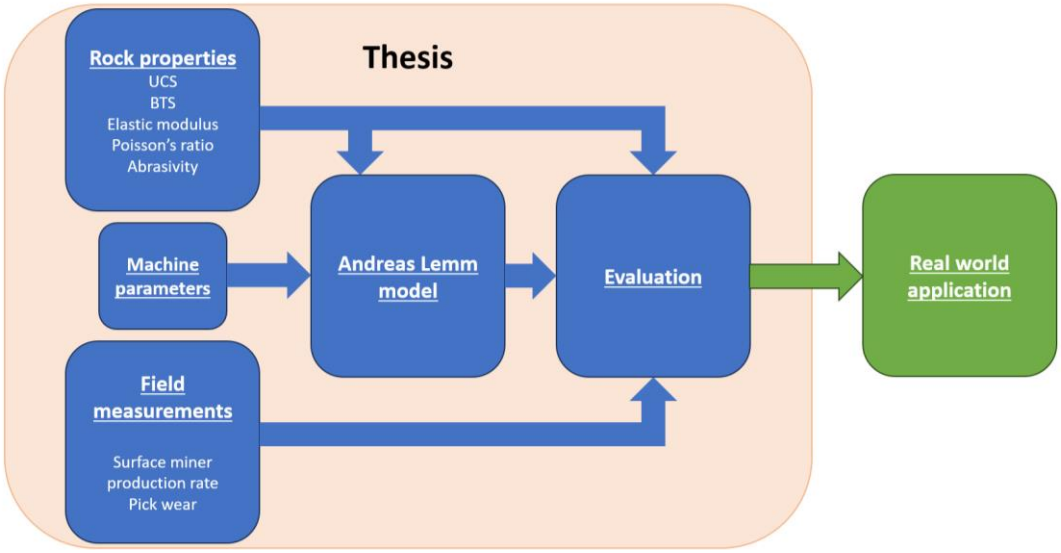

Figure 1. Components of this thesis

2. Surface miners

Surface miners are a type of continuous mining machine, which excavate rock by the means of a rotating drum lined with conical picks (Grafe, 2022). They can be used in production mining for the extraction of soft or medium strength rocks, such as coal, gypsum, iron ore, salt, phosphate, bauxite, limestone (Nikitin et al., 2007; Zajączkowski, 2021), and in Estonia, oil shale (Väizene et al., 2013). The same type of machine is used in the road construction industry for road milling (Grafe, 2022).

Surface miners can be subdivided based on the position of the cutting drum – front, rear and central drum (**Figure 2**). Front and rear drum designs allow for higher mobility, while central drum positioning sacrifices mobility for better penetration power (Vorona, 2012).

Figure 2. Surface miners with different drum configurations. **A** – front cutting drum (Takraf TSM 300) (Directindustry, 2026); **B** – rear cutting drum (Vermeer T1255) (Department of Mining, 2012); **C** – central cutting drum (Wirtgen 280 SMi) (author's photo, 2025)

The machines can also be divided into top-down and bottom-up cutting designs based on the rotational direction of the drum. Both designs offer advantages – top-down produces more uniform particle size distribution, while bottom-up designs have a higher production rate, especially in layered rocks, as cutting from the bottom can tear slabs of rock loose from layer boundaries (Grafe, 2022).

2.1. Excavation with a surface miner

Surface miners cut rock via a cutting drum lined with conical picks. These picks carry out the actual excavation, by cutting grooves into the rock mass as the drum rotates and the machine advances. The tools are generally arranged in a helical pattern around the drum (**Figure 3**). This ensures that the picks are evenly distributed along the drum, leading to more uniform force distribution. This also aids in the cutting process, as each pick breaks out material towards the groove made by the previous pick. A

helical pattern also helps guide excavated material towards the centre of the drum and the conveyor (Grafe, 2022).

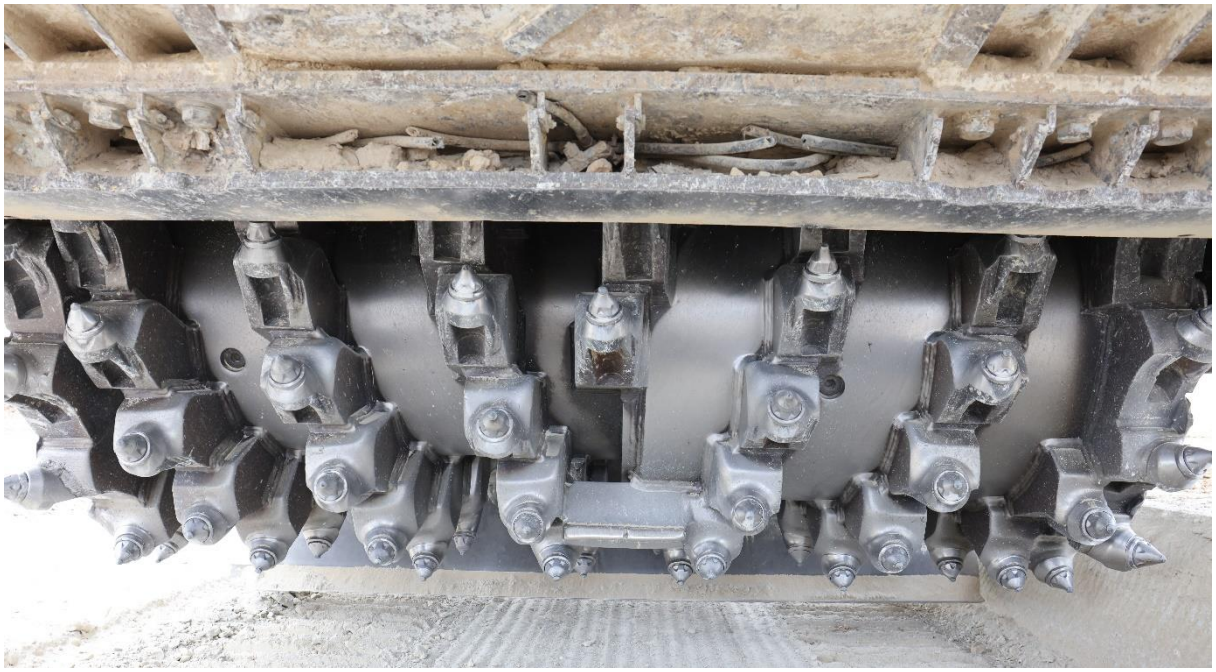

Figure 3. Cutting drum of the Wirtgen 280 SMi. The helical pick placement can be observed. (author's photo, 2025)

The picks in a cutting drum are set at an angle, called the skew angle, relative to the moving direction. This induces lateral forces in the pick, making them rotate. Rotation is a vital part of conical picks, as this reduces tool wear and prolongs their service life. When excavated materials enters the tool holder, the pick may get stuck and no longer rotate, resulting in asymmetrical wear (Yasar et al., 2023).

During operation, the surface miner cuts out a wedge-shaped area due to the rotation of the drum and the forward movement, as can be seen in **Figure 4**. This means the cutting depth varies throughout the cut. From the schematic, it can also be seen, that throughout most of the cut, the forces from the pick into the rock are oriented at an angle compared to the horizontal plane. The rotational movement also generates an upward force, which helps breaking out layers in the upper region of the cut (Grafe, 2022). Many factors influence the cutting operation, which are detailed in chapter 3.1.

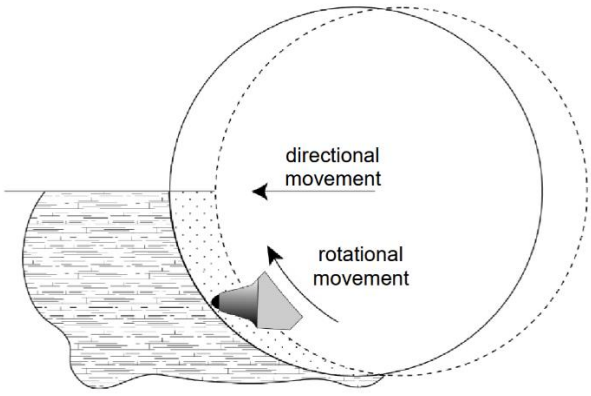

Figure 4. Schematic showing the cutting action (from Grafe, 2022)

2.2. Advantages of surface miners

Surface miners offer many advantages over traditional drilling and blasting, which is why their use has been increasing in the past decade. The main benefits of using a surface miner are explained below.

Elimination of drilling and blasting

While drilling and blasting is a very efficient and widely used method for extracting rock, there are situations where it is not applicable. As old mineral deposits deplete and settlements expand, new mines often must operate near residential areas or environmental protection zones, where there are heavy restrictions on mining operations. Due to the high environmental impact of blasting in the form of seismic waves, flyrock and the production of toxic gases, the use of explosives is often prohibited. Surface miners offer a high productivity mechanical excavation method with a smaller impact as an alternative to drilling and blasting (Pradhan & Dey, 2009; Zajączkowski, 2021).

Selective mining

Surface miners enable high-selective mining in layered deposits, where ore is interbedded with waste rock, such as in coal (Pradhan & Dey, 2009) or oil shale deposits (Väizene et al., 2013; Väli, 2011). Surface miners also enable more accurate extraction on layer boundaries, leading higher recovery rates of ore and lower dilution (Pradhan & Dey, 2009). For example in the Narva oil shale mine, surface miner use reduced the ore loss from 12% down to 5%, which is advantageous from both economic and environmental standpoint (Väli, 2011).

Simplified operations

A surface miner combines several operations into a single machine. It performs the roles of rock extraction, primary crushing, and if necessary, loading into a truck, without the need of additional vehicles. This means that other mining machinery can be utilized elsewhere and the mining process can be performed with minimal personnel (Hutchins & Oppelaar, 2016; Pastarus et al., 2008). Moreover, it allows for a more continuous process by reducing the number of separate operations in the mining cycle (Zajączkowski, 2021).

2.3. Disadvantages of surface miners

While surface miners offer many benefits over other mining methods, such as drilling and blasting, there are several downsides to consider. The most important disadvantages are outlined below.

Limited applicability

Whether a surface miner can be used in a mine is heavily dependent on the conditions at the mine, namely the geological parameters of the deposit. The range of conditions a surface miner can operate in depends on the specific model (Pastarus et al., 2008; Zajączkowski, 2021). Rock type and strength are the biggest factors defining the usability of a surface miner. According to the WIRTGEN Surface Mining Manual, in certain rocks, surface miners start to become unusable at around 100 MPa compressive strength range and beyond 160 MPa, they are no longer applicable in any rock type (Wirtgen Group, 2017).

Cost

A surface miner, being a complex machine which does many operations, is typically more expensive than other mining machines of equivalent size. Therefore, should a mine want to acquire one, it would be a significant capital investment. Furthermore, depending on the conditions at the mine site, a surface miner can have high operating costs as well. The cost per ton of material may be as much as 3 times that of drilling and blasting method (Zajączkowski, 2021).

2.4. Surface miners in Estonia

The working principle of a surface miner allows for high-selective mining of layered deposits, which makes it an ideal mining machine in the Estonian oil shale deposit (Väli, 2011). The oil shale productive layer consist of relatively thin (sub 1 m) oil shale layers interbedded with limestone (Bauert & Hints, 2024). A surface miner allows for the oil shale layers to be extracted separately from the limestone more efficiently than other methods, leading to higher oil yields when used for shale oil production (Nikitin et al., 2007).

Surface miners appeared in Estonia over 3 decades ago. The first surface miner in this country was the Wirtgen 2600 SM, which operated in Väo limestone quarry between 1989 and 1991 (Nikitin et al., 2007; Pastarus et al., 2008) The same surface miner was also used for construction work (Sayankin, 1990). Between 1992…2014, several surface miners were tested in Estonia, such as the Wirtgen 2100 SM in Kurevere, Väo and Aru-Lõuna quarries and Wirtgen 2200 SM, 2500 SM and Tackraf TM25 in the Põhja-Kiviõli mine (Pastarus et al., 2008; Väizene et al., 2013); also a Vermeer T1255 at the Väo quarry and Põhja-Kiviõli mine (Väizene et al., 2013). Starting in 2007, the state oil shale company Eesti Põlevkivi used a Wirtgen 2500 SM to great effect at the Narva mine for some years (Väli, 2011).

Starting from 2006, surface miners have been continuously operating at the Põhja-Kiviõli mine, owned by Kiviõli Keemiatööstus. The first model bought was the Wirtgen 2500 SM, followed by another one in 2012 (Kiviõli Keemiatööstus, 2026a). In 2021, Kiviõli Keemiatööstus acquired a new surface miner, the Wirtgen 280 SMi (Wirtgen, 2022).

As of 2026, Põhja-Kiviõli remains the only mine in Estonia, where surface miners are operating, with two active machines. The company has ceased the mining of oil shale with the machines, due to excessive generation of fine-grained material unsuitable for the shale oil production process. Instead surface miners are used to remove limestone overburden without the need for drilling and blasting (K. Sulp, personal communication, 2025).

In spring 2026, Kiviõli Keemiatööstus rented out the older 2500 SM to aid in the construction of Rail Baltica. The specific construction site is near the Tallinn Airport, which precludes the use of blasting to remove limestone, hence the need for mechanical excavation. The company managing this site opted to try to use a surface miner as opposed to hydraulic breakers, due to the former having higher productivity (Kiviõli Keemiatööstus, 2026b). This shows that there is potential for surface miner use outside of traditional mining.

3. Foundations of cutting efficiency computation

Though surface miners have been increasingly used over the years, they are only suitable within a certain range of condition. The applicability of a surface miner is dependent on the properties of the rock needing to be mined. The simplest and most accurate way to find out the efficiency of a machine in specific conditions is to run machine trials at the mine. This however is costly, and there might not be a machine readily available for testing. To avoid the need for expensive *in situ* machine trials, several computational models and formulas have been developed, which attempt to evaluate the productivity of surface miners based on the characteristics of the machine and the rock mass itself.

3.1. Factors affecting cutting productivity

There are many parameters, which influence the productivity of a surface miner. These can be broadly divided into three categories: intact rock parameters, rock mass parameters and machine parameters (Origliasso et al., 2014; Prakash & Murthy, 2017). The first group contains attributes of the rock itself, such as compressive and tensile strength, density, abrasivity etc. The second group are parameters which describe the rock mass, such as rock quality designation (RQD), rock mass rating (RMR), Schmidt rebound hardness number (RN) etc. The final group encompasses parameters of the surface miner, such as engine power, drum width, drum radius, tool configuration etc (Prakash & Murthy, 2017; Singh et al., 2026). Some of these will be discussed in more detail below.

Uniaxial compressive strength

Uniaxial compressive strength (UCS, also unconfined compressive strength) is one of the most important rock mechanical parameters to assess machine performance (Origliasso et al., 2014; Prakash & Murthy, 2017; Singh et al., 2024). UCS represents the maximum axial strain the rock can resist before failure; thus, the cuttability of the rock is mainly dependent on this value. Increase in UCS also raises the energy required to fracture the rock mass, therefore it is directly tied to the production rate of a surface miner (Singh et al., 2025). UCS is measured in laboratory setting via the UCS test.

Tensile strength

During mining, rocks can be affected by both compressive and tensile stresses. Therefore, the tensile strength is an important characteristic for assessing rock behaviour during excavation (Jamshidi & Akbay, 2025; Prakash & Murthy, 2017). There are two methods for measuring tensile strength in laboratory setting – the direct tensile strength (DTS) and the Brazilian tensile strength (BTS). The BTS test, also known as splitting tensile strength or indirect tensile strength, is the more common of the two, due to the simplicity of performing the test (Jamshidi & Akbay, 2025), and it is the method generally used when discussing cutting technology (Lemm, 2016).

Elastic modulus

The elastic modulus (E, also Young's modulus) is another rock mechanical parameter, which holds importance in some surface miner productivity models (Prakash et al., 2015). Elastic modulus is a measure of a materials ability to resist elastic deformation – larger value means higher stress level, at which the rock experiences elastic deformation (Hu et al., 2024). This means that more force is

required to break rocks with high elastic modulus (Yang et al., 2024). The elastic modulus can be found as the slope of the elastic region of the stress-strain curve during UCS testing (Lemm, 2016).

Poisson's ratio

The Poisson's ratio (v) is the relationship between strain in different axes, that is how much a material expands laterally when it is compressed axially. In natural rocks, the value range is small, typically ranging from 0,15 to 0,30 (Lemm, 2016). There are several ways to determine the Poisson's ratio of rocks. The Poisson's ratio can be calculated from the strain data during UCS or triaxial compression strength tests (Narimani et al., 2025; Shustov et al., 2024), or by using dynamic methods, such as the resonance method and the ultrasonic pulse measurement (UPM) (Amaral et al., 2005).

Abrasivity

Abrasivity in a rock defines its ability to wear down other materials it comes into contact with. It is determined by the mineral composition and grain size of a rock (Mucha, 2023). Abrasivity is an important factor to consider in cutting operations. It greatly affects the performance of the machine and high abrasion increases tool wear (Hartlieb & Bock, 2018; Origliasso et al., 2014). There are many methods for determining the abrasivity of a rock, such as the CERCHAR, LCPC, Shimazek etc. The most commonly used is the CERCHAR scratch test (Mucha, 2023).

Machine parameters

Several parameters of the cutting machine itself play a key role in the productivity calculations, most importantly the power of the machine, either the raw engine power or the power of the cutting organ(Origliasso et al., 2014). Other important factors are relating specifically to the cutting organ, such as drum width and diameter, tool configuration, tool type, pick wear etc (Prakash & Murthy, 2017). Most of this information can generally be procured from the manufacturer's brochures.

3.2. Computational models for surface miners

Several empirical models have been developed to predict the performance of different types of cutting machines. These models generally incorporate few parameters into the equation and are only valid in specific sites. Several of these models are for roadheaders, though due to the similarity of the cutting tools, they can be applied for surface miners as well, to an extent.

One of those models was formulated by Bilgin et al. (1997), which tries to predict the net cutting rate (NCR) – meaning productivity of the cutting operation – using the formula:

$$NCR = 0{,}28 \cdot P \cdot 0{,}974^{RMCI} \quad (1)$$

Where:
NCR – net cutting rate (m^3/h)
P – cutting power of the machine (kW)
$RMCI$ – rock mass cuttability index

The RMCI in turn can be found according to this formula:

$$RMCI = UCS \cdot \left(\frac{RQD}{100}\right)^{\frac{2}{3}} \quad (2)$$

Where:
UCS – uniaxial compressive strength of the rock (MPa)
RQD – rock quality designation, the % of core pieces >10 cm in a drill core (%)

This model incorporates both UCS and machine power, and also properties of the rock mass on a basic level. However, it was developed with roadheaders in mind and does not account for other aspects, such as abrasivity, which play an important role in surface miner operations.

A formula specifically for surface miners was created by Jones & Kramadibrata (1995), which found the relationship between UCS and production rate (PR) as a logarithmic function:

$$PR = 1005 - 559 \cdot \log UCS \quad (3)$$

Where:
PR – production rate (m^3/h)

This method has several shortcomings however, namely that it only works of soft rocks (UCS ≤ 60 MPa). Furthermore, it only relies on the compressive strength of the rock, without accounting for machine parameters or rock mass properties.

Based on the machine data from different manufacturers and empirical testing, Origliasso et al. (2014) developed a model, which calculates the PR of surface miners. The predicted value already considers the time for ancillary tasks, such as repositioning and changing of picks. They found that the PR can be represented by the formula:

$$PR = (2 \cdot P_w - 600) \cdot e^{-0{,}024 \cdot UCS} \quad (4)$$

Where:
P_w – machine power (kW)

This equation however assumes a low-abrasivity rock (CAI ≤ 0,5); in harder deposits, abrasivity becomes and important factor in production rates, hence Origliasso et al. (2014) proposed the following modifications to the formula:

$$PR = (2 \cdot P_w - 600) \cdot e^{-0{,}024 \cdot (UCS + 10 \cdot (CAI - 0{,}5))} \quad (5)$$

Where:
CAI – CERCHAR Abrasivity Index

This model has several advantages over the one proposed by Jones & Kramadibrata (1995), in that it incorporates the UCS, machine power and abrasivity into the calculation, though it still does not account for many of the parameters affecting the operation of a surface miner.

One of the more comprehensive models was developed by Prakash et al. (2015), which not only evaluates the productivity of the surface miner, but also fuel and pick consumption. This model

incorporates many more parameters in its calculation than the previous examples. The main formula for productivity is as follows:

$$TPH = 181{,}5 \cdot {RCI_{SM}}^{0{,}245} \tag{6}$$

Where:
TPH – production rate (t/h)
RCI_{SM} – rock cuttability index for surface miners

The RCI_{SM} in turn can be found by the following relationship:

$$RCI_{SM} = \frac{1000 \cdot MF}{IRF \cdot RMF} \tag{7}$$

Where:
MF – Machine Factor
IRF – Intact Rock Factor
RMF – Rock Mass Factor

These three factors can be found according to the following equations:

$$MF = \frac{P_w \cdot CA \cdot CS}{1000} \tag{8}$$

$$IRF = E \cdot CAI \cdot LV_p \tag{9}$$

$$RMF = \frac{IV_p}{RN} \tag{10}$$

Where:
CA – cutting area of the drum (m^2)
CS – cutting speed (m/min)
E – elastic modulus (GPa)
LV_p – laboratory p-wave velocity (km/s)
IV_p – *in-situ* p-wave velocity (m/s)
RN – rebound hardness number

The CA of the drum can be found using the following formulas:

$$CA = L_a DW \tag{11}$$

$$L_a = \frac{2\pi R \cos^{-1}[(R - D)/R]}{360} \tag{12}$$

Where:
L_a – length of the arc in contact with the rock (m)
DW – drum width (m)
R – drum radius (m)
D – cutting depth (m)

As can be seen, the model developed by Prakash et al. (2015) is quite complex, incorporating 10 different variables in the calculation. When applied in coal and limestone mines, the model produced decent results, with an error between 9,9…15,4% in productivity calculation compared to real production rate. However, it is not known whether this model generates decent results in other geologic conditions as well.

3.3. Andreas Lemm cutting model

The computational model developed by Dr. Andreas Lemm is principally a model for evaluating forces generated during the cutting process in different types of machines, as described by his dissertation (Lemm, 2016). From these forces, cutting energy and performance can be predicted.

What sets this model apart from other empirical or semi-empirical models is the use of the so-called cutting plane method. In this method, a 3D representation of the cutting tool is "sliced" into planes; for each plane, the interactions between tool and the cut material are modelled and the resulting forces calculated. The total cutting force is obtained by adding the forces of all planes together. Because of this, the model offers a more realistic portrayal of the cutting process and therefore a more accurate estimation of the forces involved.

The model incorporates many different parameters in its calculations, which can be seen in **Table 1**. Aside from those, the model considers drum configuration, rotation speed, pick spacing and other factors.

Table 1. Parameters incorporated into the Lemm model

	Parameter	Symbol	unit
Geometrical	Wedge angle	β	°
Geotechnical	Compressive strength	σD	MPa
	Splitting tensile strength	σZ	MPa
	Brittleness	κ	-
	Internal friction angle	ϕ	°
	Cohesion	c'	MPa
	Axial strain at failure	εB	mm/mm
	Poisson's ratio	ν	-
	Young's modulus	E	Gpa
Geo-/process-technical	Attack angle	δ	°
	Rotation angle	ε	°
Process-technical	Penetration depth	ζ	m, mm
	Cutting depth	hs	m, mm

Within this work, the model outputs the average forces acting on the cutting tools and specific energy consumption. Based on the specific energy consumption, a comparison of computed results with measured cutting performance is made (described in chapter 5.8).

4. Materials and methods

4.1. Study area

The research site (**Figure 5**) was in Põhja-Kiviõli II oil shale mine located 5 kilometres west of Kiviõli in Ida-Viru County, Estonia. The mine is owned by Kiviõli Keemiatööstuse OÜ (KKT) and has been operating since 2011. Oil shale is mined using the strip-mining method, where the overburden is removed in long strips, and the overburden from each strip is deposited into the pit left behind by the previous strip. In the Põhja-Kiviõli II mine, overburden is removed by either drilling and blasting, or by using a surface miner (K. Sulp, personal communication, 2025).

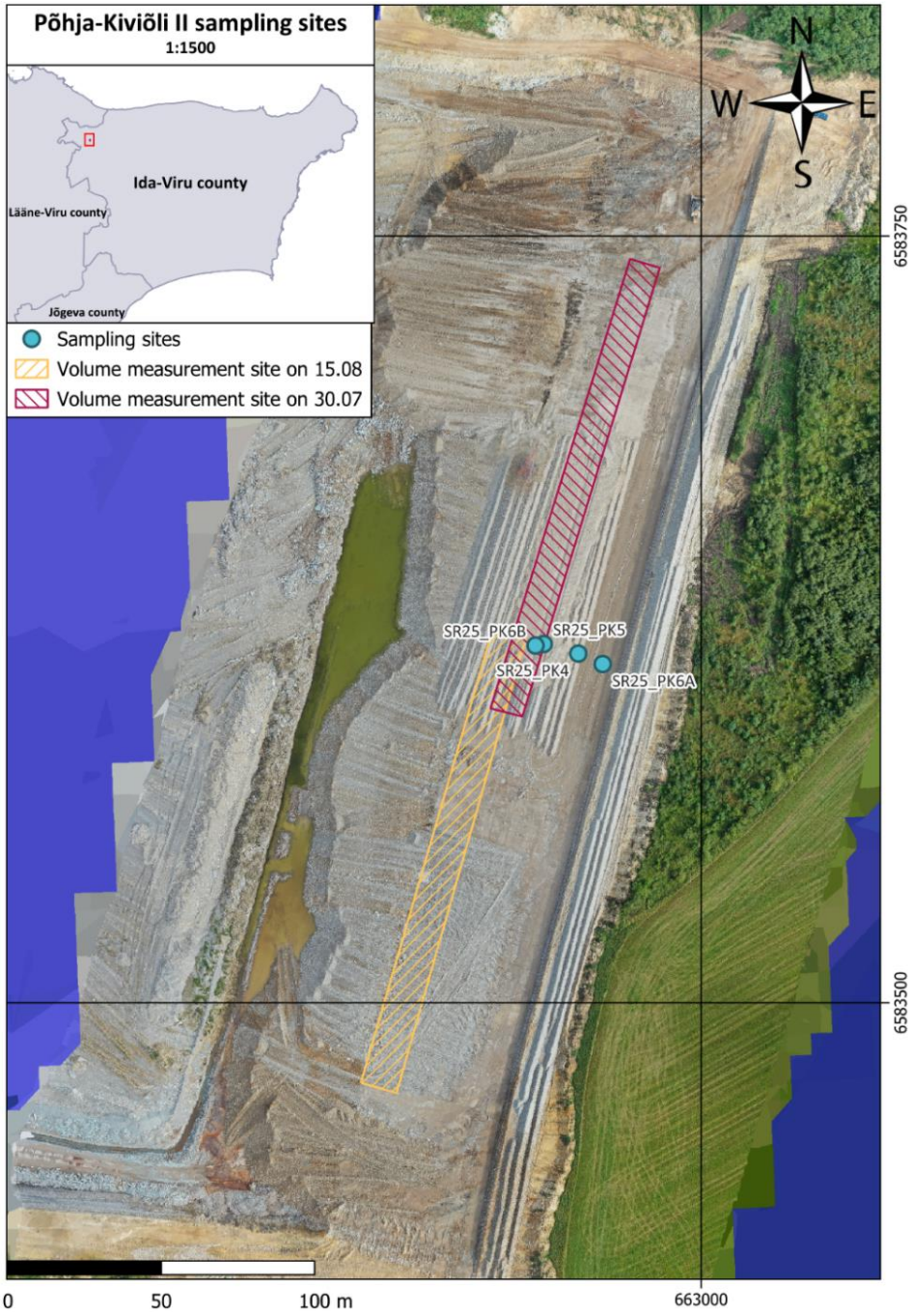

Figure 5. Overview of the study area in the Põhja-Kiviõli II mine

The study area was determined by the workflow in the mine. Since the surface miners in this mine are exclusively used for the removal of overburden, only active pits currently in the stripping phase would be viable. Furthermore, since production rate measurements were only to be carried out on the newer, Wirtgen 280 SMi surface miner, there were only two possible study areas to consider – one in the south-western and one in the south-eastern part of the mine.

The final decision was made based on the on-site conditions at each location. The south-eastern site was chosen for its wide-open space compared to the other location, as to minimize the disruption of the mining process. At the other site, the mining process had reached the oil shale extraction phase in one end of the pit, leading to high traffic and increased heavy equipment presence. The pit was also deeper, and the operating area of the surface miner closer to the pit walls, which can disrupt the sightlines between the GNSS receiver and satellites, leading to problems with setting up ground control points. Furthermore, the rock mass at the south-eastern location was mostly uncompromised by severe geologic fractures and karsts, which cause localized changes in rock mechanical properties and can therefore introduce unwanted variables to the results. Based on the reasons given above, the south-eastern location (**Figure 6**) was chosen as the study area for this project.

Figure 6. Aerial view of the chosen study area in the south-eastern part of the mine. (author's photo)

4.2. Surface miner production rate measurement

The field studies at the mine were conducted by the author between the 28th of July and 22nd of August 2025. The studied surface miner was the Wirtgen 280 SMi, the newest model currently operating at the mine. The production rate for the surface miner was measured and calculated for 7 separate mined strips in 5 rock layers.

The field work consisted of the following operations:

- marking down and measuring the coordinates of Ground Control Points (GCP);
- timing each operation of the machine;
- scanning the volume of each strip extracted by the surface miner.

This was followed by desk work, which consisted of:

- transferring data from the equipment onto a computer;
- processing said data;
- calculating extracted volumes and production rates.

Ground Control Points

The Ground control points (GCP) were created by hammering a small divot into the rock surface with a chisel. The point was marked using orange paint and all points were numbered in sequence. New GCP-s were created as required, whenever old ones were lost due to mining operations or adverse weather. The points were arranged in a grid in a manner that covered the full length of one cut by the surface miner.

Figure 7. Measuring the coordinates of GCP-29 using the Trimble R10 (author's photo)

The coordinates of the points were measured using the Trimble R10 GNSS Receiver and the TSC3 controller (**Figure 7**). The GNSS reference station network of the Estonian Land and Spatial Development Board was used for further accuracy. The precision of the device was validated prior to taking any measurements using the Level 2 Local Geodetic Network point with GPD ID 228812. The *Ground Control Point* mode of the device, with a measurement time of 3 minutes, was used for all points. All coordinates were taken in the plane coordinate system L-EST97 and all elevations were

taken in the EH2000 height system, as described by the Geodetic system regulation (Geodeetiline Süsteem [Geodetic System], 2025).

Time study analysis

Every operation of the surface miner was timed during its operation using the built-in stopwatch of an android smartphone and the data was analysed in Microsoft Excel. Total time spent for each different operation was calculated. Using the time spent specifically on extracting rock and the measured volumes, the cutting production rate was calculated for different rock layers.

Volume measurements

The cut volume was measured using the Stonex X120GO SLAM Laser Scanner, which was controlled through the dedicated mobile application GO*app* on an android smartphone. This method was chosen for the high degree of accuracy given by the LiDAR scanning technology and the fast speed at which data could be gathered on site. Speed was of specific importance, as each pass of the machine had to be scanned prior the beginning of the next pass.

Each mined strip was scanned in two parts, as to make the scanning process easier and less disruptive to the operation of the mine. Every scan was tied to at least 4 GCP-s, with at least two points being shared between the two scans of a single strip.

Data processing and calculation

The scan results were transferred onto a computer, and the initial processing was conducted in the Stonex dedicated software GO*post* on the Windows 10 operating system. GCP coordinates were input into the software, to automatically tie the generated point clouds to the L-EST97 coordinate system. During processing, default software settings were used, apart from the *Stability Parameter*, which was varied depending on which scan was being worked on, and the *Distance* parameter, which was decreased to 30 m from 100 m, to reduce the amount of data noise caused by dust clouds. After creation, all point clouds were exported in an optimized and colorized format.

The point clouds were imported into the open-source 3D point cloud processing software CloudCompare (**Figure 8**). This software was used to verify, and if necessary, manually correct the alignment of each point cloud pair making up the scan of each strip, and then combine each pair into a singular point cloud. The software was also used to clean up the scans of noise. Completed point clouds were again exported from the software.

The final volume measurements were made in the Autodesk Civil 3D engineering software using an educational license through the Autodesk Education Community. The point clouds were first converted into suitable format using the Autodesk ReCAP software. In Civil 3D, a TIN surface was generated from each point cloud. To calculate the volumes, surfaces created from sequential scans were compared to each other to find the cut volume. All values were transferred to an Excel table and using the data collected from the time study, cutting production rate of the surface miner was calculated.

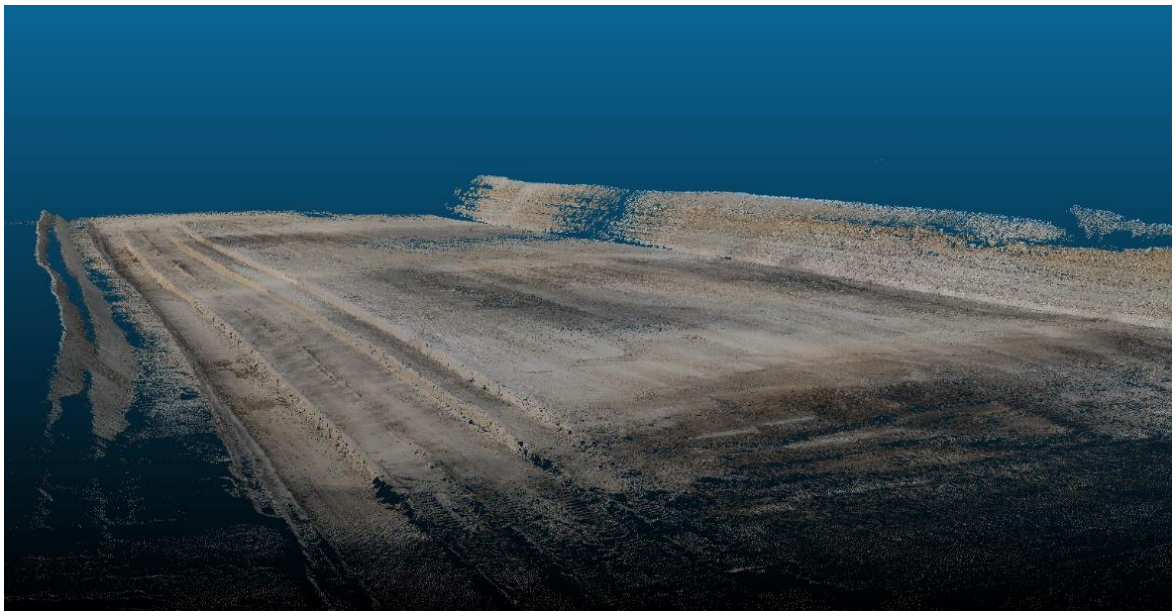

Figure 8. Point cloud of the scan from strip 5, rendered in CloudCompare.

4.3. Sample material

The material for the rock-mechanical tests was procured from the study area in the Põhja-Kiviõli II mine on the 27th of August 2025 by the author, accompanied by Dr. Bruno Grafe and early-stage researcher Sander Kanter. The samples were gathered from 4 different sampling sites (**Table 2**,

Figure 5. Overview of the study area in the Põhja-Kiviõli II mine

). However, material from only layers 4 to 6 was gathered, as sampling the upper layers proved to be unsuccessful by the means available to the extraction team at that time.

Table 2. Sampling sites at the Põhja-Kiviõli II mine

Sampling site	Coordinates*		Elevation** (m)
	x	y	
SR25_PK4	6583613	662960	51.9
SR25_PK5	6583617	662949	51.4
SR25_PK6A	6583610	662968	51.0
SR25_PK6B	6583616	662946	50.9

*Coordinates given in the L-EST97 coordinate system

**Elevations given in the EH2000 height system

The lumps were cut with a concrete saw from slabs of limestone loosened from the larger rock mass by the operation of the surface miner (**Figure 9**). The blocks were cut to a size allowing the drilling of cores of suitable length, while remaining light enough to be carried by hand. A total of 14 blocks of material were procured from the mine site.

Figure 9. Sampling at the Põhja-Kiviõli mine. **A** – Limestone blocks being cut for sampling by Bruno Grafe, assisted by Sander Kanter. **B** – a block cut from layer 5. (photos by the author)

Sample geology

The sampled rock consists mostly of grey fine-grained biomicritic limestone, with occasional interbedded kukersite oil shale. The oil shale is a fine-grained sedimentary rock containing a high amount of kerogen, which can be turned into shale oil and gas through destructive distillation (Bauert & Hints, 2024). Both the limestone and oil shale are rich in fossils, leading to localized weaknesses in the rock.

Stratigraphically the layers belong to the Maidla Member of the Viivikonna Formation, Kukruse Regional Stage (international Sandbian Stage), based on the descriptions by Männil (1984). The studied layers lie around 2 m above the easily recognizable oil shale layer “H” of the Kiviõli Member of the Viivikonna Formation (**Figure 10**).

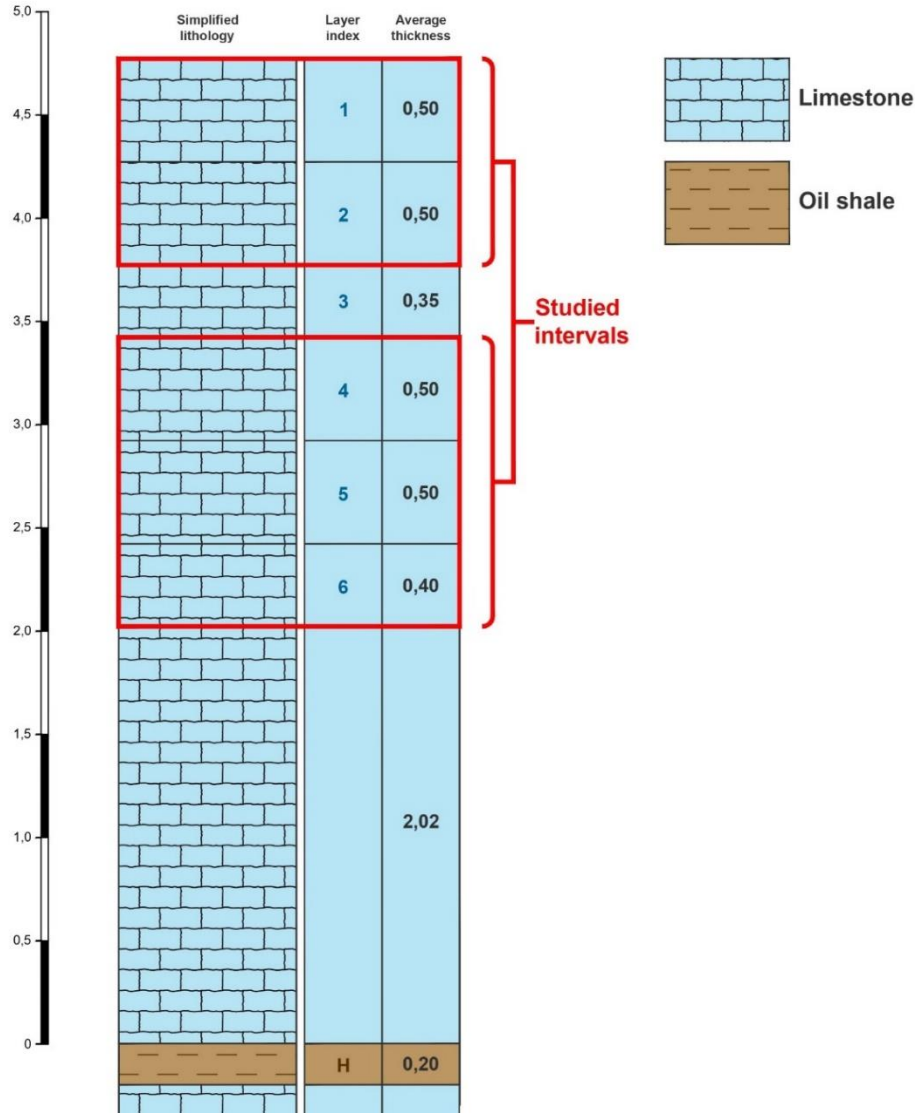

Figure 10. Cross-section and location of the studied intervals in relation to the oil shale layer "H".

4.4. Sample preparation and testing

The initial cores were prepared by the author, assisted by fellow master's student Reet Männik, at the Department of Geology Särghaua Earth Science Centre in Pärnu county. Cores with a diameter of around 54 mm were drilled using a hand-operated drill press (**Figure 11**). The core samples were prepared in accordance with the ISRM suggested methods, whenever applicable (Bieniawski & Bernede, 1979). To account for anisotropy, cores were drilled in three different orientations – perpendicular, parallel and at a 45° angle to the bedding of the rock. A total of 109 cores were drilled from the three collected layers.

The initial cores were cut into proper length for testing. For the UCS test, mainly cores with a length-to-diameter ratio of 2:1 were prepared (**Figure 12**), with some cores having a ratio of 1:1. It was necessary to diverge from the ISRM suggestions (Bieniawski & Bernede, 1979) in this instance, as making cores with the suggested 2,5…3:1 ratio would not have been feasible due to the presence of cracks within the rock.

Figure 11. Sample preparation at Särghaua. **A** – diamond drill used for coring of rocks; **B** – raw cores drilled from rock (photos by Reet Männik)

Disk-shaped specimen with a length-to-diameter ratio of 1:2 were cut for the BTS tests (**Figure 12**), in accordance with the ISRM guidelines (Bieniawski & Hawkes, 1978). The leftover material from the coring process was used for the CERCHAR abrasivity test and for the creation of thin sections, which were meant for evaluation equivalent quartz content.

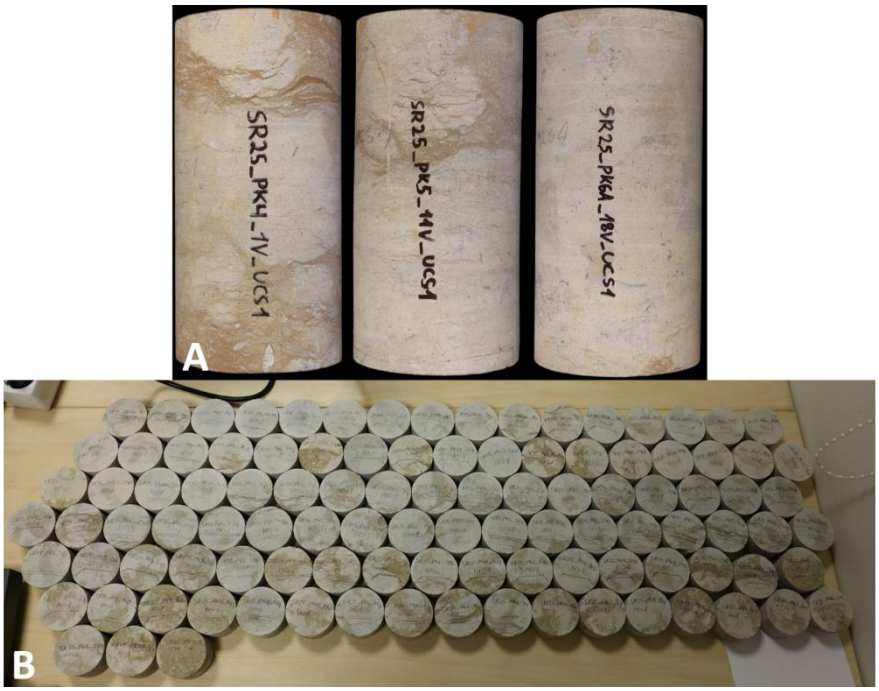

Figure 12. Examples of prepared samples. **A** – single UCS core from each layer; **B** – all BTS samples prepared for this thesis (photos by the author)

A total of 93 UCS samples and 105 BTS samples were prepared for a grand total of 197 samples. The total number of samples analysed for each test can be seen in **Table 3**. The diameters and lengths of all UCS and BTS samples were calculated as an average of 3 measurements to an accuracy of 0,1 mm using a mechanical calliper. All laboratory tests and analyses were conducted at the Department of Geology laboratories at Tallinn University of Technology.

Table 3. Total number of samples analysed in each test

Test	No. Of samples	Purpose
UCS	93	Finding compressive strength and elastic modulus of rocks
BTS	105	Finding tensile strength of rock
UPM	27	Finding Poisson's ratio of rock
CERCHAR	4	Finding abrasivity
XRD & XRF	12	Analysing abrasive mineral content

4.5. Uniaxial compressive strength (UCS)

The UCS tests were conducted in accordance with the ISRM standards (Bieniawski & Bernede, 1979). The prepared samples were tested using the AUTOMAX PRO-M Compact-Line Compression Machine by CONTROLS (**Figure 13**). The data was logged using the CONTROLS DATAMANAGER software. The axial load was applied at a constant rate of 0,5 MPa/s until sample failure. Peak load at failure was recorded, and the UCS was calculated by the as the ratio of the maximum axial load to the original cross-sectional area of the specimen. The calculation was done automatically by the software.

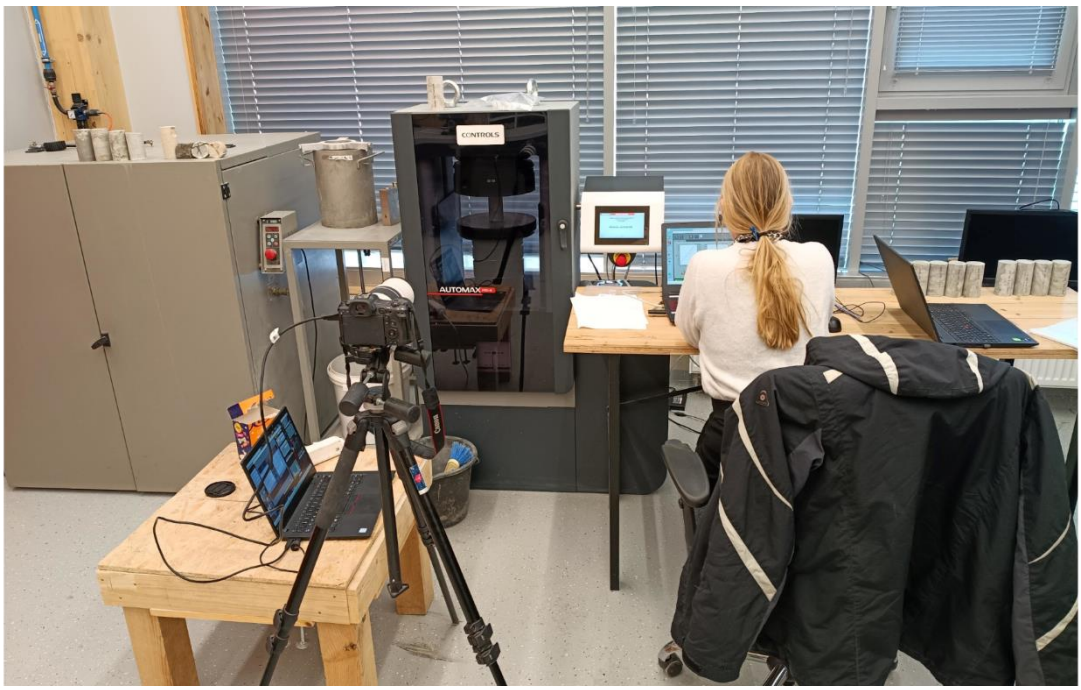

Figure 13. Setup for the UCS test (author's photo)

To monitor deformation behaviour and evaluate the elastic properties of the rocks, the testing apparatus was outfitted with a displacement sensor. Strain data was recorded synchronously with load

and displacement data, allowing for the determination of elastic modulus (EM) using the linear elastic portion of the stress–strain curve. The points, from which the EM was derived, was marked by the user in the software, and the EM itself was calculated by the software. All samples were photographed before and after test.

The UCS test were conducted on samples drilled in each direction (**Figure 14**), to study effect of anisotropy on the compressive strength of the rock.

To account for the overestimation of UCS in the case of cores with a L/D ratio of 1:1, the values were converted to a L/D ratio of 2:1 using a correction formula outlined by (Tuncay & Hasancebi, 2009):

$$UCS_C = \frac{UCS}{(0{,}88 + 0{,}24 \cdot D/L)} \tag{13}$$

Where UCS_C is the corrected UCS value;
UCS is the measured UCS value;
D/L is the diameter to length ratio, in our case 1.

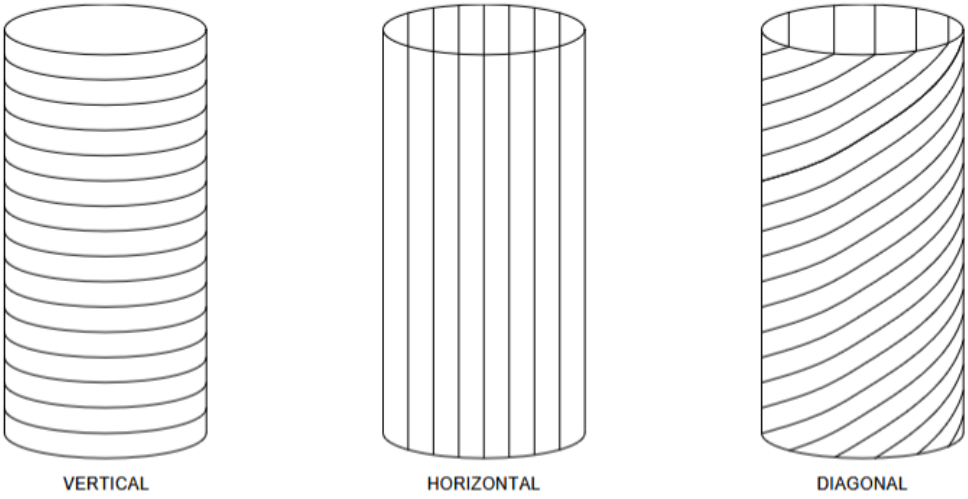

Figure 14. Rock layer orientations in the UCS samples.

4.6. Brazilian tensile strength (BTS)

The Brazilian tensile strength tests were carried out according to the suggestions by the ISRM (Bieniawski & Hawkes, 1978). The same testing apparatus and software was used as with the UCS tests, with a BTS test adapter used to hold the samples (**Figure 15**). BTS tests were carried out on disc-shaped specimens with a diameter of around 54 mm and a thickness of approximately 27 mm, following ISRM recommendations. Samples were wrapped with masking tape around their circumference. Each sample was diametrically loaded at a constant loading rate of 200 N/s until initial failure of the sample. The tensile strength was computed using the following formula:

$$\sigma_t = \frac{0{,}636P}{Dt} \tag{14}$$

where σ_t is the tensile strength;
P is the peak load at failure;
D is the diameter;
t is the thickness of the specimen.

Figure 15. Setup for BTS tests (author's photo)

Tests were conducted for all three orientations relative to bedding to investigate directional dependence of tensile strength. In the case of horizontally and diagonally drilled cores, the samples were subdivided into two groups, each group being loaded with the bedding at a 90-degree angle in relation to one another (**Figure 16**).

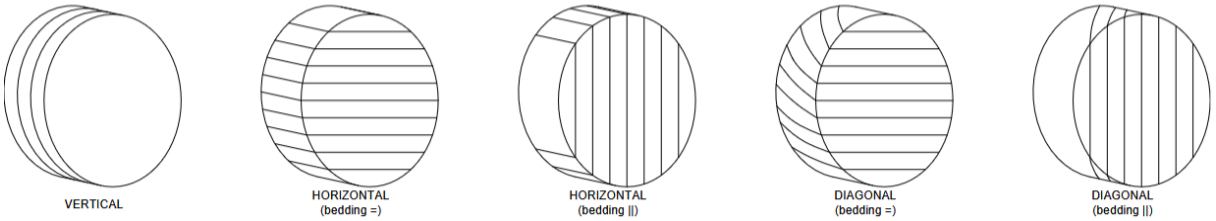

Figure 16. Rock layer orientation in the BTS samples.

4.7. Abrasivity

Two different methods were used to quantify the abrasivity of the samples – the CERCHAR abrasivity index and the quartz equivalent value (QEV).

4.7.1. CERCHAR abrasivity index

The CERCHAR abrasivity index (CAI) was determined using the procedure defined in ISRM Suggested Methods (Alber et al., 2014). West Cerchar Rock Abrasiveness Tester by Wille Geotechnik was used to conduct the tests. A single sample was tested for each sampling site, so 4 samples in total. Excess material from UCS and BTS sample preparation was used to cut cylindrical disks, to serve as test material.

A steel stylus with a Rockwell hardness of 55 HRC was drawn across the surface of the samples under a normal load of 70 N over a 10 mm stroke length, at a rate of around 1 mm/s. For each sample, 5 repetitions in two directions – perpendicular and along the bedding of the rock – were carried out.

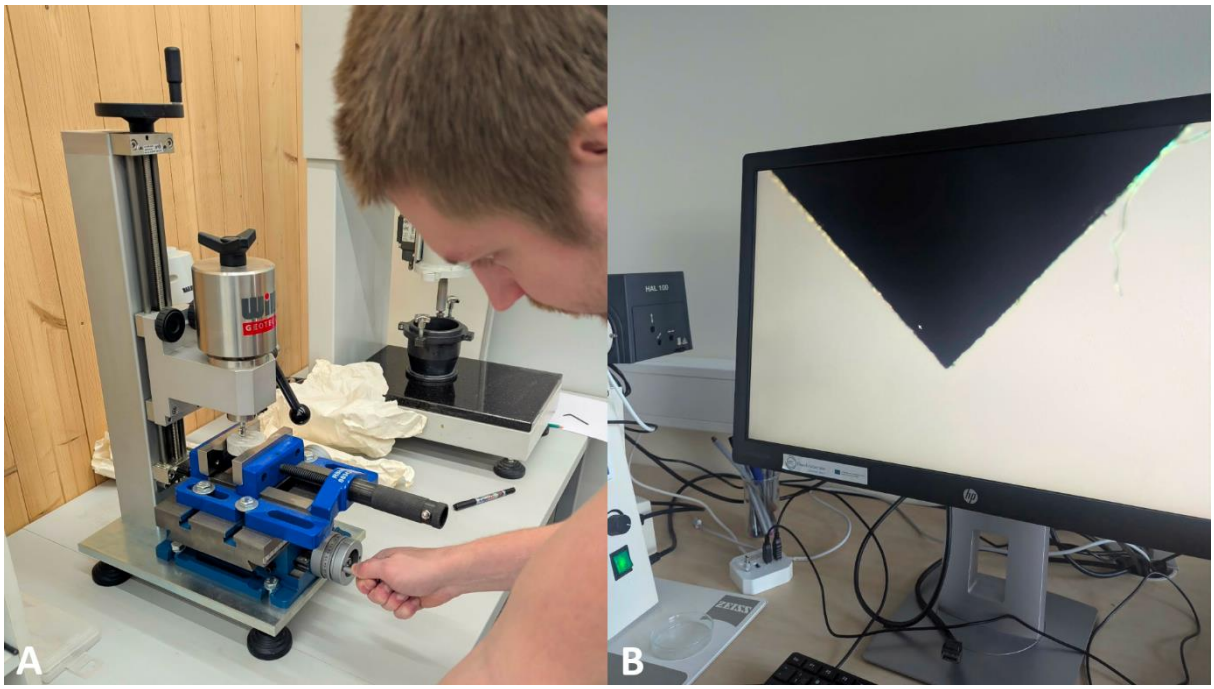

Figure 17. CERCHAR testing. **A** – the test apparatus and setup; **B** – CERCHAR pin under a microscope (author's photo)

The wear on the stylus tip was measured under a microscope using 24X magnification and reported with an accuracy of 0,01 mm. Tip wear of each pin was measured from four directions and averaged; the results from 5 pins was averaged and the CAI was calculated using the formula:

$$CAI = d \cdot 10 \tag{15}$$

where CAI is the CERCHAR Abrasivity Index;
d is the wear tip surface measured to an accuracy of 0.01 mm.

To account for the influence of saw-cut surfaces on the CAI value, the wear flat tip measurement was corrected according to the equation specified in the ISRM Suggested Methods, which is:

$$d_C = 1{,}14 \cdot d_s \tag{16}$$

where d_C is the corrected wear tip surface;
d_s is the wear flat diameter on a pin used on saw-cut surface.

4.7.2. Equivalent quartz value

Thin sections

The equivalent quartz value, along with the BTS value and median grain size of the rock, is used to calculate the Schimazek abrasiveness factor within the model. Initially, the EQV was planned to be derived from thin section analysis. For this reason, thin sections were created by the author from the same core material, as was used for the CERCHAR tests. Rectangular blocks roughly 20x40x10 mm in size were glued onto glass plates using two-part heat-cure epoxy resin, so that the rock layering was perpendicular to the glass surface.

The glued blocks were cut to around 2 mm thickness using a diamond saw, then ground to around 100-micron thickness using a diamond grinding wheel on the Buehler PetroThin this section machine. Finally, the rock was wet sanded down to roughly 30 microns in thickness by hand, using 3-micron aluminium oxide powder as the abrasive agent.

The thin sections were then analysed using a microscope equipped with a polarizing filter. However, the microscopy analysis proved to be unsuccessful, as the grain size of the limestones of all layers was very small and no abrasive minerals, such as quartz or feldspars, could be discerned from the image (**Figure 18**). Hence an XRD and XRF analysis was ordered.

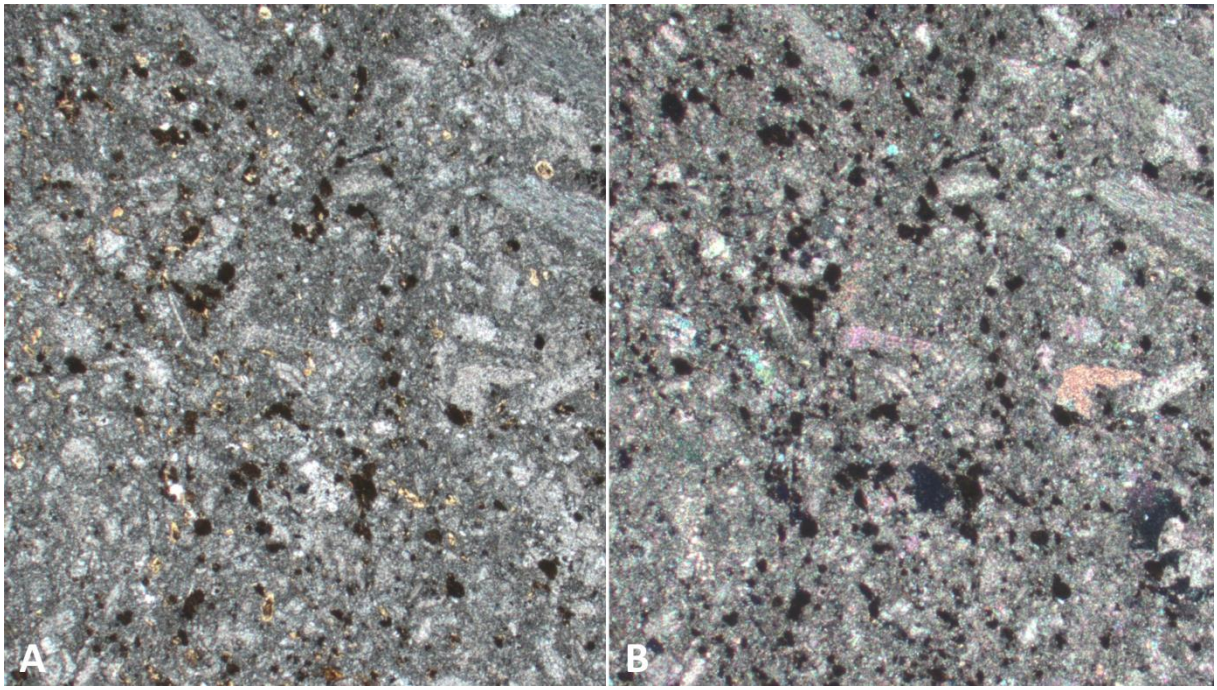

Figure 18. Thin section of layer 5 as seen under a microscope. **A** – normal light; **B** – polarized light (photos by the author)

XRD and XRF

The XRD and XRF analysis was conducted at the Department of Geology Laboratory of Geochemistry and Mineralogy by Toivo Kallaste, Nata-Ly Pantšenko and Erki Leht. The author of the thesis prepared the samples for the analyses by crushing the sample material, which was the same core material used for the CERCHAR tests, using a laboratory jaw crusher. The crushed material was divided into smaller increments using a sample splitter, until a final sample size of around 50 g was reached. This material was then milled into fine powder using a bench top ring mill.

XRF analysis was conducted in two parts: pressed powder pellet for trace element analysis and fused bead disk for macro elements. Pellets were made by the author (**Figure 19**), by mixing 8 g of pulverized sample with 0.5% Mowiol glue solution and pressing the powder into a pellet with a hydraulic press, after which the sample was dried at 105 °C.

Disks were made by the lab staff, by drying around 2 g of pulverized sample at 105 °C and weighing the dried sample, after which it is heated to 950 °C and held there for 4 hours. After heating, the sample is weighed again to determine the loss on ignition. Then, 1 g of the heated sample is mixed with 10 g of lithium metaborate and fused into a disk using Claisse M4 burner.

A total of 8 disks and 8 tablets were created. 4 of each type of sample were made from the same material as was used for the CERCHAR tests. The other 4 were made by crushing all the BTS samples from a single sample site and homogenizing the resulting crushed material and splitting it as explained above.

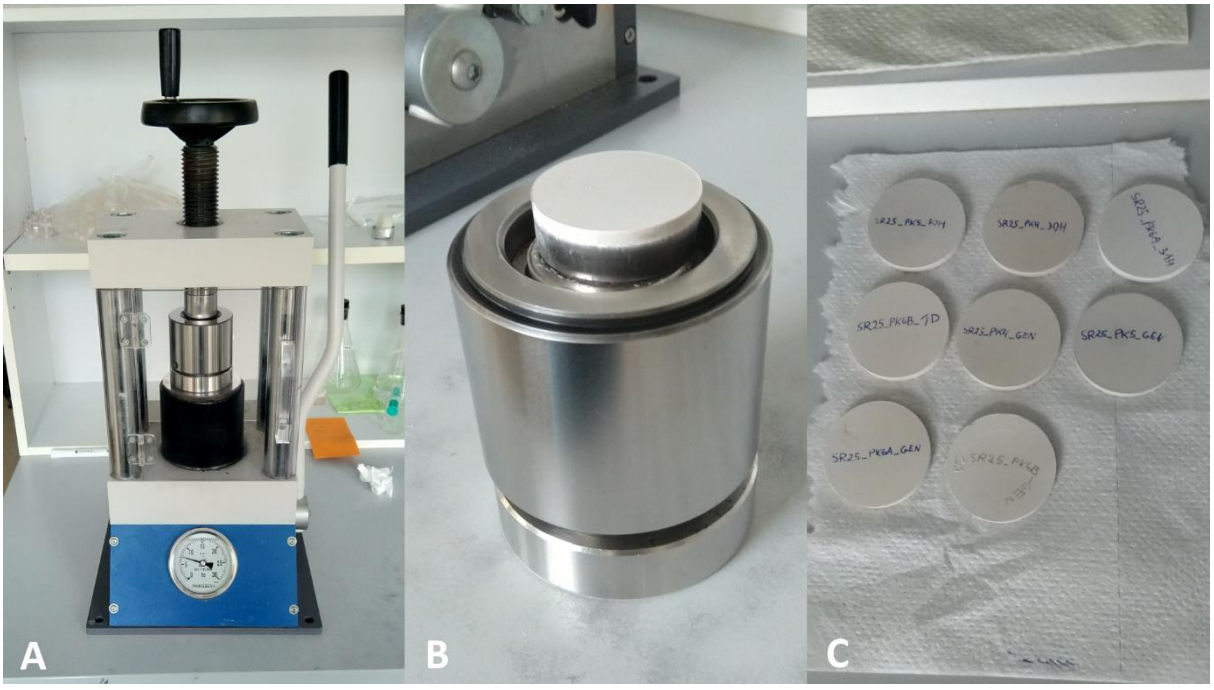

Figure 19. Creation of tablets for XRF analysis. **A** – hydraulic press for tablet making; **B** – finished tablet as it comes out of the press; **C** – all finished tablets. (photos by the author)

XRD samples were prepared by the lab staff, by spreading 0,1 g of pulverized material was spread on a sample tray using ethanol solution, after which it was dried and analysed. The mineral content of the samples was derived using semi-quantitative Rietveld analysis.

In the Rietveld model, the mineral contents are derived on a calcium basis. For this set of samples, there were two calcium-bearing minerals: calcite and dolomite. The Rietveld model determines the relative proportions of all minerals except illite, as it cannot be reliably modelled. The Rietveld results are then multiplied by an appropriate coefficient so that the total calcium content in calcite and dolomite matches the XRF result. This coefficient is determined using a fitting method (the Goal Seek function in Excel). In limestones, the sum of the modelled mineral contents is therefore below 100%, with the missing fraction consisting of illite and organic matter (T. Kallaste & N.-L. Pantšenko, personal communication, April 24, 2026).

Calculating the equivalent quartz content

To find the EQV of a rock sample, the hardness values of each mineral present in the rock are normalised to quartz, which has a Rosiwal hardness H_R of 100. The normalised Rosiwal hardness values of any given mineral are multiplied with the relative abundance of said mineral within the rock and summed together to obtain the equivalent quartz content, as shown by the formula (Kaspar & Latal, 2022):

$$EQV = \sum_{i=1}^{n} \frac{A_i \cdot H_{Ri}}{100} \tag{17}$$

Where EQV is the equivalent quartz content of the rock;
A_i is the concentration of mineral i in %;
H_{Ri} is the Rosiwal hardness of mineral i normalized to quartz.

The H_R values of minerals used in this thesis can be found in **Table 4**.

Table 4. Normalized Rosiwal hardness values used in the calculation of the equivalent quartz content of samples (Kaspar & Latal, 2022).

Mineral	Quartz	Calcite	Orthoclase	Dolomite	Pyrite
Normalized Rosiwal hardness	100	3	45	4	55

4.8. Poisson's ratio

To determine the Poisson's ratio of the rock layers, ultrasonic wave measurements were conducted on the samples by the author. The method is based on the difference in propagation speeds of the P- and S-waves generated within the rock by the ultrasonic pulse. By measuring the difference in wave speeds, the Poisson's ratio can be calculated using the formula (Proceq, 2022):

$$v = \frac{V_P^2 - 2V_S^2}{2(V_P^2 - V_S^2)} \quad (18)$$

Where v is Poisson's ratio;
V_P is the pulse velocity of the P-wave;
V_S is the pulse velocity of the S-wave.

The measuring of the ultrasonic pulse velocity was carried out in accordance to the standard EN 12504-4:2021 (CEN, 2021). The Pundit Lab (+) Ultrasonic Test Instrument by Proceq was used for the test, while the Punditlink software was used to operate the device, record the measurements and calculate the Poisson's ratio. Tests were carried out using 500 kHz ultrasonic transducers in direct transmission, meaning the transducer were situated on opposite sides to one another (**Figure 20**). Natural honey was used as ultrasonic couplant, as per the recommendation of Senior Researcher Madis Ratassepp from the Department of Civil Engineering and Architecture.

9 UCS test cores were chosen from each layer – 3 in every drilling orientation – for a total of 27 cores across all ultrasonic tests. The cores were chosen based on their condition – cores with cracks, fissures, chipped layers etc. were avoided, as to keep the wave signals as clear as possible. Only cores with a L/D ratio of 2:1 were used, meaning cores with a length of around 108 mm.

Prior to testing the samples, the apparatus was calibrated using the calibration cylinder. To perform the test, both ends of the core were first covered with a thin layer of honey, then the core was placed on a transducer situated on the table and the other transducer was held against the top of the core (**Figure 20**). The transducers were shifted around, and singular pulses were sent through the core, until an adequate waveform was seen in the software. The voltage and frequency of the pulse was also varied whenever necessary to produce a better signal.

Once the received signal was good, two individual measurements were taken. In the software window, the arrivals of the S and P-waves were marked on the graphs, and the software calculated the Poisson's ratio automatically based on that information. The Poisson's ratios were marked down in a table and the results were analysed.

Figure 20. Transducer placement during the ultrasonic wave measurements.

4.9. Pick and drum analysis

Additional information about the vehicle was gathered on site by the author and supervisors. The drum diameter and pick spacing on the cutting drum was measured. The cutting drum was filmed while rotating and the wear state of the individual picks was assessed from 0…1, with 0 being no wear and 1 being complete wear. Several fresh picks and a worn picks were acquired for modelling the pick shapes. A collection of discarded used picks was sorted and photographed, to assess the different types of wear pattern and their prevalence.

4.10. Cutting modelling

The cutting modelling was conducted by Dr. Andreas Lemm using the data gathered through the aforementioned tests. A total of 12 calculations series were ordered. The series were divided into two groups – 6 calculations modelled with fresh picks and 6 calculations with completely worn picks, to see the effect of pick condition on the productivity. Of each group, two calculations were made for each layer, one with average rock conditions and one with “worst-case scenario” conditions.

For the average working conditions, the mean values of 2:1 ratio diagonal cores for UCS and elastic modulus and mean values of diagonal cores samples for BTS were used in all cases. The quartz equivalent values of generalized samples for each layer were used. For the worst-case scenario calculations, the maximal UCS, BTS and elastic modulus values were used, regardless of core direction. The maximum quartz equivalent values were used in this case.

Due to the average Poisson’s ratio values being similar in all layers, this was taken as a constant in all calculations, derived from the overall average of all layers. The same principle was applied for CAI values.

Additional information was provided as well, such as the depth of the cut, cutting drum diameter, pick spacing on the drum and a drawing of a fresh and completely worn pick. The latter data was of great importance, because it was used by Dr. Lemm to create a 3D representation of the picks for the calculations.

Results conversion

Dr. Lemm’s model gave specific energy consumption as an output, which was then compared to theoretical specific energy consumption based on the cut volume, time and engine power of the surface miner.

The rock mass condition has a significant effect on the cutting performance. In the case of the 2500 SM surface miner, which is similar to 280 SMi studied in this thesis in power and size, the Wirtgen Surface Miner Manual (Wirtgen Group, 2017) specifies a productivity difference of up to 3 times between solid and shattered rock. Based on the descriptions in the manual, the rock at the Põhja-Kiviõli mine can be classified as “micro-seamy”, due to its horizontal layering and weak, thin oil shale beds in between the limestone. In this type of rock at a UCS of 40…80, the manual predcits a production rate of 170…220 m^3/h, which is comparable to values measured in the field.

Based on this, a correction factor of 1,9 was applied to the modelled specific energy consumption, to account for the influence of rock mass.

4.11. Data analysis and visualizations

Test results were combined into tables and analysed in Microsoft Excel. The raw test data can be seen in Appendixes 7…9. Visualizations of the data were made using Python with the matplotlib library. To assist in the writing of Python scripts for the creation of graphs, the AI assistant GitHub Copilot was used. AI was not used for any data analysis or for making any deductions from the results.

The map of the study area was created using open-source software QGIS (version 3.34.11). The orthophoto was created using the free photogrammetry software RealityScan. Drawings were made using Autodesk AutoCAD 2025.

5. Results

5.1. UCS and elastic modulus

Viable results were attained for 92 cores in total, of which 78 were full-length cores (L/D ratio of 2:1). 31 of the cores were from layer 4 (22 when counting 2:1 ratio cores), 25 from layer 5 (20 2:1 cores) and 36 from layer 6. The UCS values ranged between 28…104 MPa with an average of 55,62 MPa (**Figure 21**). 1:1 ratio cores had on average higher values, than 2:1 cores, even after applying the correction formula. Over 50% of the values fell within the range 30…60 MPa, while >75% of values fell within the range 30…70 MPa. Detailed table can be seen in **Appendix 2A**.

Overall, layer 4 samples had the lowest UCS, with an average of 40,97 MPa (38,80 MPa when only considering 2:1 cores). Layer 5 was the second strongest layer, with the samples having an average UCS of 57,65 MPa (55,63 MPa for 2:1 cores). Layer 6 samples had the highest average UCS at 66,83 MPa (there were no 1:1 ratio cores for layer 6) and the highest overall recorded UCS. In every layer, vertical cores had the lowest average UCS, followed by diagonal and then horizontal cores. Horizontal cores generally produced the widest value range as well.

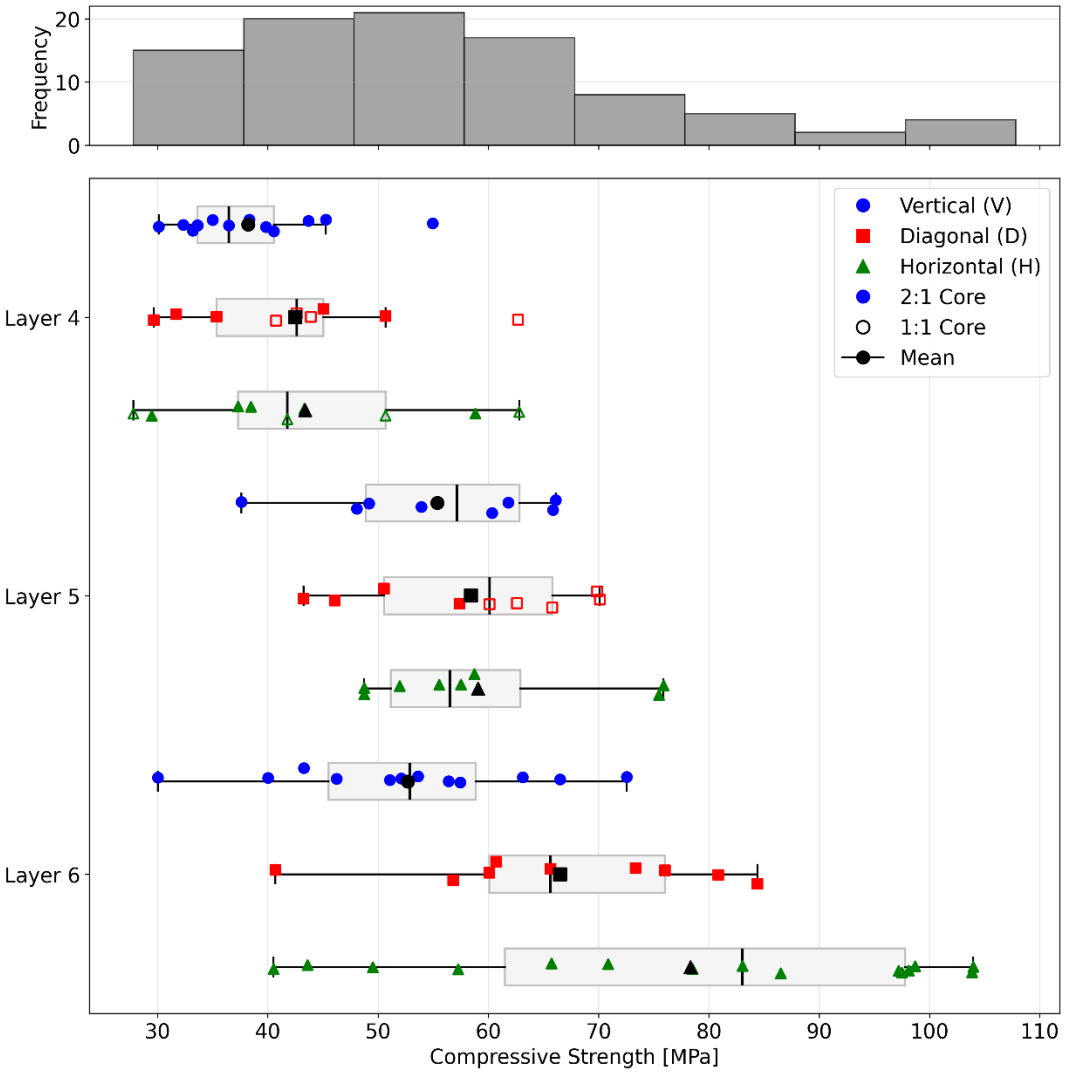

Figure 21. UCS values results by layer and core direction

Elastic modulus of the UCS samples (**Figure 22**) was around 4,8…33,6 Gpa, with a mean value of around 13,9 Gpa. When considering 2:1 cores separately, the average inceases to 14,2 GPa. More detailed figures can be seen in **Appendix 3A**. Generally, the elastic modulus values followed the same trend as the compressive strength values – layer 4 had the lowest average value of 9,8 GPa (9,5 GPa with only 2:1 cores), followed by layer 5, with an average of 14,2 GPa (13,9 GPa for only 2:1 cores) and then layer 6 cores, with an average of 17,2 GPa. Regarding core directions, the same relationship applies as in UCS samples – vertical cores had the lowest average elastic modulus, followed by diagonal and then horizontal cores, though in this case, the differences were more pronounced.

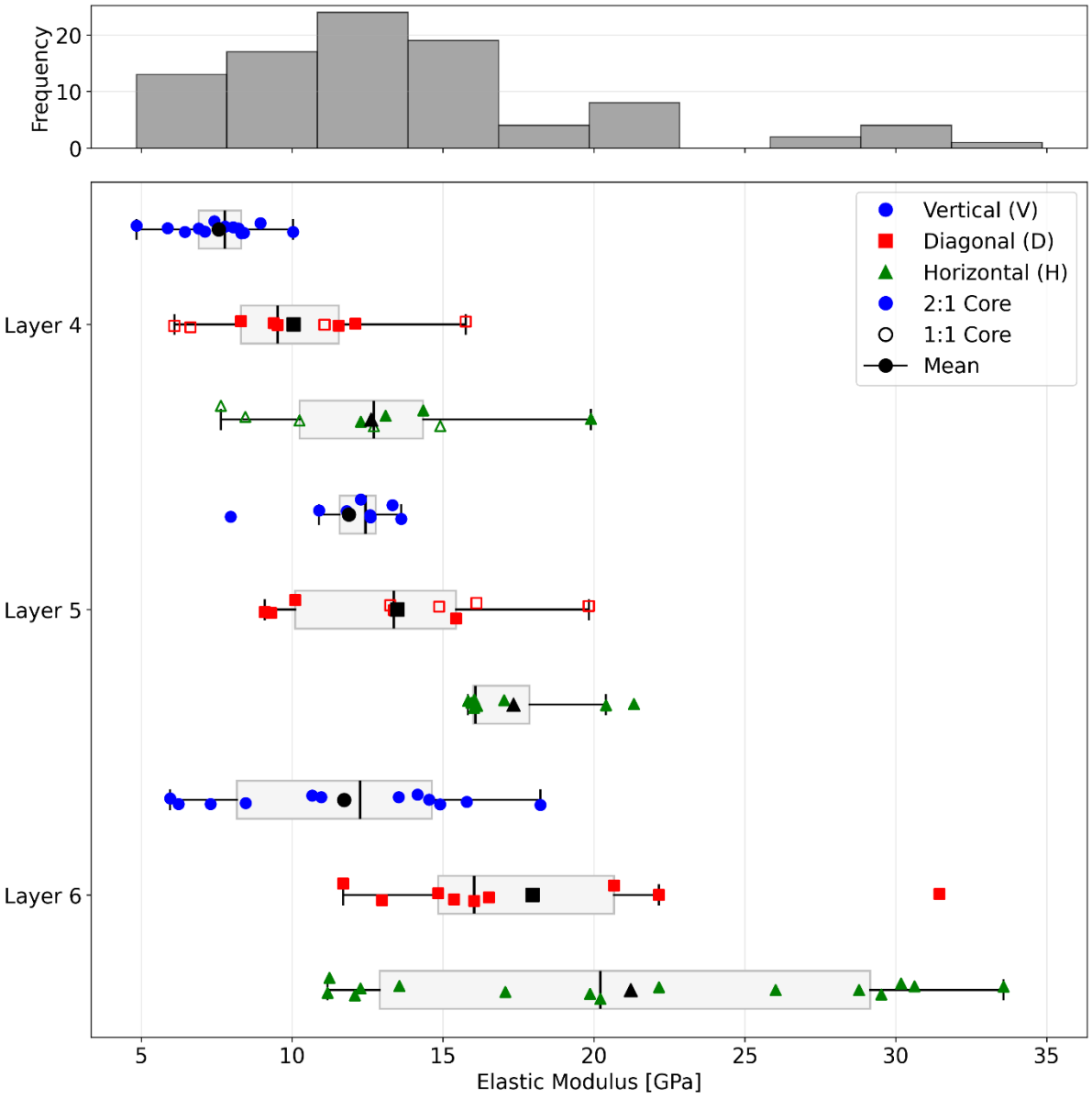

Figure 22. Elastic modulus values by layer and core direction

Layer 4

The UCS test results for Layer 4 are summarized in **Appendix 2B**. In general, the UCS ranged from 28…63 MPa, with a mean value of 40,97 MPa. Orientation wise, vertical cores showed values between

30…55 MPa, diagonal cores between 30…63 MPa and horizontal cores between 28…63 MPa. The aerage values in different orientations were 38,23 MPa, 42,50 MPa and 43,39 MPa respectively.

Elastic modulus results for Layer 4 are presented in **Appendix 3B**. Overall, the elastic modulus varied from 4,8…19,9 GPa, with an average of 9,8 GPa. In vertical cores, values ranged between 4,8…10,0 GPa, in diagonal cores from 6,0…15,8 GPa and in horziontal cores from 7,6…19,9 GPa. The mean elastic modulus for these orientations was 7,6 GPa, 10,0 GPa and 12,6 GPa respectively.

Layer 5

The UCS results for Layer 5 are summarized in **Appendix 2C**. Overall, the UCS of this layer was 38…76 MPa, with an average of 57,65 MPa. Vertically drilled cores showed values ranging from 38…66 MPa, diagonal cores from 43…70 MPa and horizontal cores from 49…76 MPa. The average UCS for these orientations were 55,36 MPa, 58,42 MPa and 59,07 MPa respectively.

For Layer 5, Elastic modulus results are given in **Appendix 3C**. Across all samples, the elastic modulus ranged from 8,0…21,3 GPa, with a mean of 14,2 GPa. For vertical cores, results were between 8,0…13,6 GPa, for diagonal cores between 9,0…19,8 GPa and in horizontal cores between 15,8…21,3 GPa. The average values for these orientations were 11,9 GPa, 13,5 GPa and 17,3 GPa respectively.

Layer 6

The UCS test results for Layer 6 are summarized in **Appendix 2D**. Overall, the UCS values ranged from 30…104 MPa, with a mean value of 66,83 MPa. Vertical cores had values between 30…73 MPa, diagonal cores between 41…84 MPa and horizontal cores between 41…104 MPa. The average values for these orientations were 52,70 MPa, 66,51 MPa and 78,32 MPa respectively.

Elastic modulus results for Layer 6 are presented in **Appendix 3D**. The elastic modulus ranged from 6,0…33,6 GPa, with an average of 17,2 GPa. In vertical cores, values weree between 6,0…18,2 GPa, for diagonal cores between 11,7…31,4 GPa and for horizontal cores between 11,2…33,6 GPa. The mean values were 11,7 GPa, 18,0 GPa and 21,2 GPa respectively.

5.2. BTS test

Of all BTS samples, 103 gave viable test results, which can be seen in **Figure 23**. Of those, 32 were layer 4, 34 layer 5 and 37 layer 6 samples. The BTS values ranged from 1,9 MPa to 10,0 MPa, with an average of 5,46. The lowest values were in layer 4, with an average of 4,03. This was followed by layer 5 with an average of 5,15, though the range of values was narrower than in layer 4. The highest values were recorded in layer 6, with an average of 6,98; however, this layer also had the widest distribution of values. More detailed figures are in **Appendix 4A**.

Layer 4

In layer 4, BTS values were in the range 1,9…7,3, with a mean value of 4,03. the lowest average BTS was 2,73 MPa, measured in samples which were drilled horizontally and the layering was oriented horizontally during testing. The highest average result of 4,32 MPa was seen in the case of diagonally

drilled samples with layering oriented horizontally during the test. These samples also had the narrowest value distribution. The widest vlue range was measured in diagonally drilled samples which were tested with the layering oriented vertically. More detailed results can be seen in **Appendix 4B**.

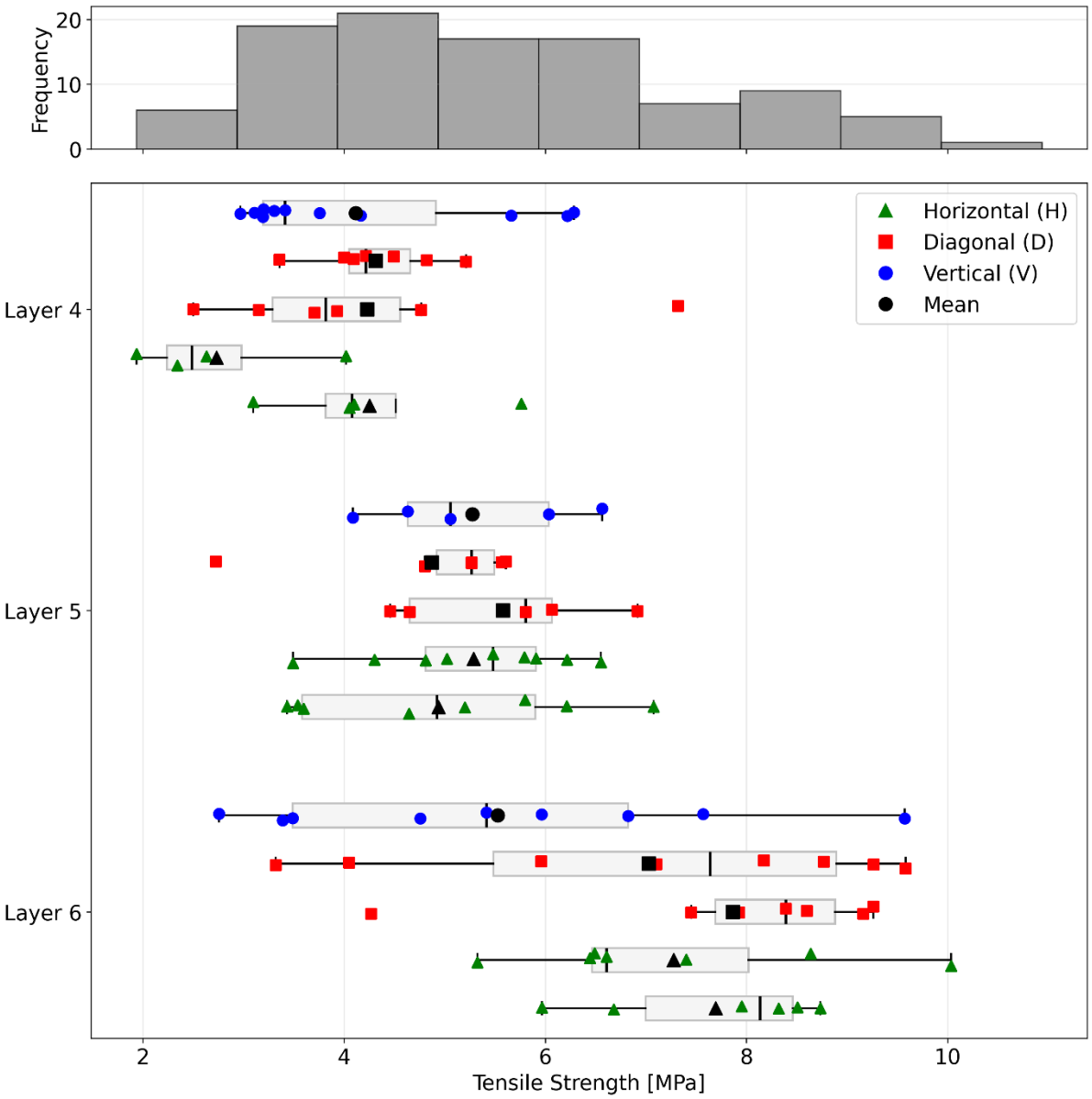

Figure 23. BTS values by layer and core direction

Layer 5

BTS values in layer 5 were between 2,7…7,1, with an average of 5,15. The lowest average BTS measured in layer 5 was 4,87 MPa in the case of horizontally drilled cores with bedding oriented vertically. The highest average BTS was 5,58 MPa in diagonally drilled cores with vertically oriented layering during testing. These samples also had the narrowest value distribution. The widest distribution of values was seen in the case of horizontally drilled samples which were tested with vertically oriented layering. Detailed table about layer 5 is visible in **Appendix 4C**.

Layer 6

In layer 6, BTS results ranged from 2,8…10,0, with a mean of 6,98. The lowest average BTS in layer 6was measured in samples from vertical cores, where it was 5,53 MPa. The highest tensile strength of 7,87 MPa was again found in diagonally drilled cores with vertically oriented layering during the test. The smallest distribution of values was seen in the case of horizontally drilled cores tested with vertically aligned layering, while the widest value distribution was recorded in vertically drilled samples. Full table is available in **Appendix 4D**.

5.3. CERCHAR abrasivity

The results of the CERCHAR abrasivity tests are summarized in **Table 5**. The wear of individual pins is depicted in **Appendix 5**. The CAI of each test series (5 individual pins) ranged from 0,30 to 0,68. In test series PK4_A and PK6A_A, uncharacteristically high wear was recorded with a single pin, which were qualified as outliers using the Interquartile Range Method and discarded from the results. Thus, the CAI among all test series with outliers removed ranged from 0,30 to 0,55.

The lowest CAI was recorded in layer 5, with an average of 0,36. The highest was layer 4 with a CAI of 0,51, layer 6 was similar with an average CAI of 0,50. Without outliers however, the highest average CAI value was found in layer 6 at 0,45, with layer 4 having a slightly lower average CAI of 0,43.

The overall average CAI across all layers was 0,47; when discarding outliers, it was 0,42. According to the classification table outlined in the ISRM guidelines, the sampled rocks can on average be categorized as having “Very low” abrasivity. When looking at the layers individually, layers 4 and 6 would classify as “Very low abrasivity”, while layer 5 would be “Extremely low abrasivity”.

Table 5. Results of the CERCHAR abrasivity tests

Test series*	**PK4_P**	**PK4_A**	**PK5_P**	**PK5_A**	**PK6A_P**	**PK6A_A**	**PK6B_P**	**PK6B_A**
CAI	0.38	0.64	0.42	0.30	0.41	0.68	0.55	0.37
CAI without outliers	-	0.47	-	-	-	0.48	-	-
Average CAI per layer		**Layer 4**			**Layer 5**			**Layer 6**
CAI		0.51			0.36			0.50
CAI without outliers		0.43			0.36			0.45
Avg. CAI					0.47			
Avg. CAI without outliers					0.42			
CAI classification					Very low abrasivity			

*PK4…6B – individual sampling sites; P – pin was dragged perpendicular to layering; A – pin was dragged along the layering.

5.4. Equivalent quartz value

The results of the XRD analysis and the calculated EQV of the samples can be seen in **Table 6**. Expectedly, carbonates dominate the mineral composition – calcite is the main mineral in all samples, with a ratio of 55…86%, followed by dolomite with a concentration of 6…26%. The pyrite content according to the XRD results was below detection limit and thus negligible – the values ranged from 0 % to 0,35 % across all samples.

For the purposes of this thesis, the most important were the concentration of quartz, which was between 1,92…6,66 %, and orthoclase, the concentration of which was 2,53…6,10 %, found in samples PK6B_1D and PK4_30H respectively. In the generalized samples, quartz concentration was in the range 2,18…5,72 % in samples PK6B_GEN and PK5_GEN respectively. Orthoclase content ranged from 2,35…4,15 %, with the highest value in sample site PK5 and lowest in site PK6A.

Table 6. Mineral composition and EQV of the tested samples based on XRD analysis in %

Mineral	Quartz	Calcite	Orthoclase	Dolomite	Pyrite*	EQV
PK4_30H	6.66	55.02	6.10	18.68	0.28	13.79
PK4_GEN	4.17	66.61	3.36	18.61	0.03	9.10
PK5_30H	4.76	60.52	4.25	25.81	0.29	10.13
PK5_GEN	5.72	63.18	4.15	24.03	0.35	10.91
PK6A_31H	2.87	86.43	2.78	6.60	0.14	7.14
PK6A_GEN	2.48	79.39	2.35	12.18	0.00	6.65
PK6B_1D	1.92	83.73	2.53	7.71	0.03	6.15
PK6B_GEN	2.18	81.36	2.67	12.33	0.09	6.45

*Below detection limit

Based on the normalized Rosiwal hardness values of minerals found in **Table 4**, EQV of the samples was found, which can be seen in **Table 6**. Despite its low concentration, quartz had the highest contribution to the EQV of all samples, except for those from sampling site PK6B, due to its high abrasivity. Calcite was the second largest contributor in the case of most samples, followed by orthoclase. Dolomite had a small impact on the results, and the effect of pyrite was negligible due to its very low presence in the samples.

The final calculated EQVof the samples was 6,15…13,79 %, with the highest value in layer PK4_30H and the lowest value in sample PK6B_1D. Among the generalized site samples, the lowest value was again in the site PK6B sample at 6,45 %; however, the highest value was calculated for sample PK5_GEN with 10,91 %.

5.5. Poisson's ratio

The calculated Poisson's ratio values for layers 4 through 6 can be seen in **Figure 24**. Across all layers, the Poisson's ratio ranged from 0,13 to 0,35, with an overall average of 0,23. Layers 4 and 5 showed similar behaviour, with averages of 0,23 and 0,22 respectively. Layer 6 had a similar mean value of 0,24, though the overall value range was a lot narrower.

Across all layers, horizontally drilled cores had consistently higher values with an average of 0,27. Vertically and diagonally drilled cores had a lower but very similar values, with the averages being 0,21 and 0,22 in vertical and diagonal cores respectively.

Within layer 4, the average Poisson's ratio varied between 0,20 and 0,28 depending on drilling orientation. Highest values were seen in horizontal cores, with vertical and diagonal cores having lower averages. The range of values was the smallest in vertical core, with diagonal and horizontal cores having a wide distribution.

A similar trend was observed in layer 5. The average Poisson's ratio ranged from 0,18 to 0,27 depending on the core drilling direction. The highest average value was again among the horizontal cores. In this layer however, the lowest average value was in vertical cores, with diagonal cores falling between them. Both horizontal and vertical cores showed a similar variance, while in diagonal cores the value range was smaller.

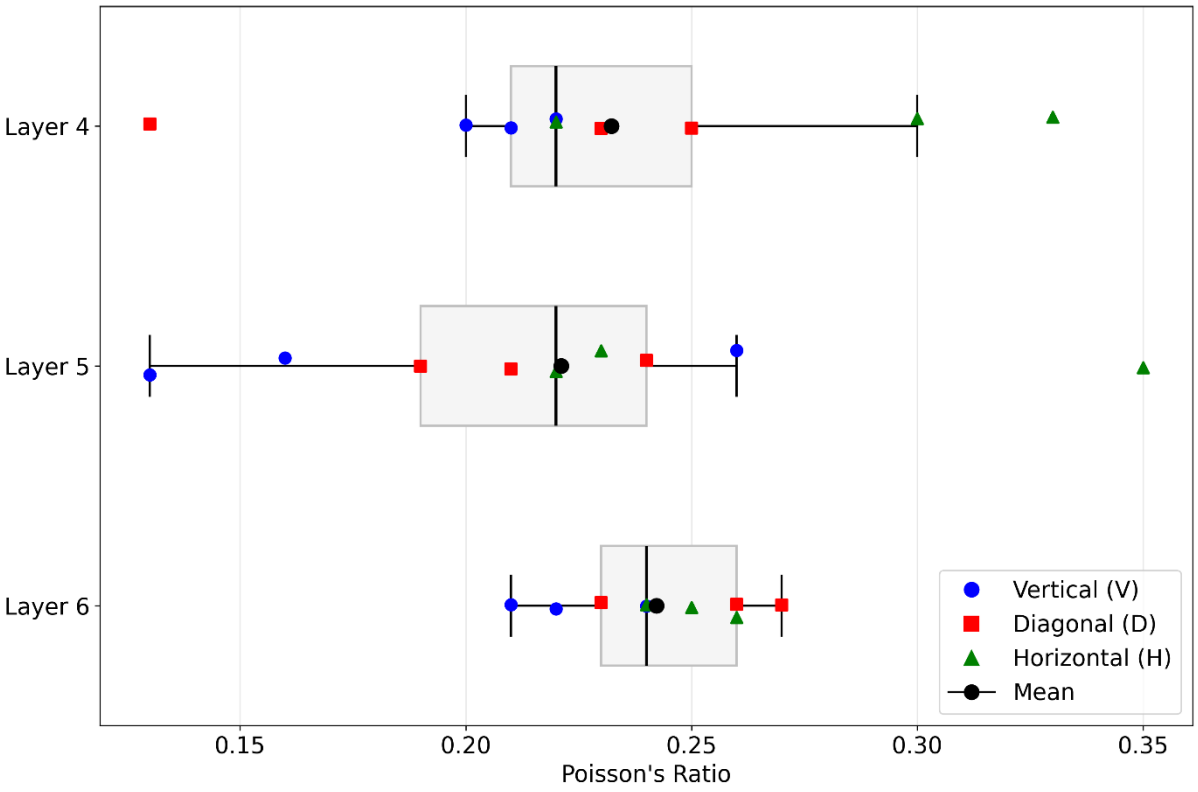

Figure 24. Poisson's ratio value by layer and core orientation

Layer 6 showed the most uniform behaviour, with Poisson's ratio values ranging from 0,22 to 0,27. Both horizontal and diagonal cores had a similar mean value, while in vertical cores, the Poisson's ratio was slightly lower. In general, there was little variance between different orientations, and the value range was narrow.

5.6. Pick analysis

A collection of discarded picks was sorted through and the picks divided into groups based on wear pattern (**Figure 25**), in accordance to the system by Thuro & Plinninger (2002). A total of 91 picks were sorted (**Table 7**). The most common wear pattern was asymmetrical wear, with 47 total picks or 52%. This was followed by brittle failure of the carbide tip, with 21 or 23% of all picks. Other types of wear were less common, with preferential tool carrier wear being the least prevalent. Uniform wear pattern was not observed in this case.

Table 7. Wear types and their abundance in used picks

Wear type	Count	Prevalence	Description
M-A2	2	2%	Preferential wear of tool carrier
M-A3	14	15%	Breakout of the carbide pin due to tool carrier wear
M-S1	21	23%	Brittle fracture of the carbide tip, leading to its destruction
M-So1	7	8%	Total wear
M-So3	47	52%	Pronounced one-sided wear

Figure 25. Different pick wear patterns observed in the discarded picks

The wear of the picks on the cutting drum was also assessed. The picks were given a subjective grading depending on the wear of the pick, on a scale 0…1. On average, the wear across all picks was 0,2. This value was later used as a correction factor when analysing modelling results.

5.7. Measured production rate

Surface miner production rate was measured for 7 individual cut strips in 5 different layers – 1, 2, 4, 5 and 6. Layer 5 had 3 individual measurements, while all other layers had a single measurement. All cut strips had a length of around 140 m, width of 2,7 m (the maximum cutting width of the drum) and a depth of 0,5 m. Only exception was strip 7, with a depth of 0,4 m. Because of this the measured volume was roughly 180 m^3 in all strips, except strip 7, where it was around 145 m^3 due to the shallower cutting depth (**Table 8**). The average cut volume across all strips was 177,3 m^3.

Cutting time varied strip by strip, ranging from 34:30 in strip 7 to 1:30:24 in strip 3 (**Table 8**) with an average time of 53:23. Time spent on the cutting process took up from 51% in strip 7 and 79% of all time in strips 2 and 6, with an average of 69% across all runs. More detailed results can be seen in **Appendix 1A**.

Cutting productivity varied greatly across different strips (**Table 8**). The lowest production rate was observed in strip 3 with 124,7 m^3/h, while the highest was seen in strip 7, with 251,8 m^3/h, a difference of 202%. Within layer 5, where there were 3 measurements, the productivity was relatively consistent, ranging from 219,7 to 243,4 m^3/h, with a mean value of 234,5 m^3/h. The overall average across all strips was 212,2 m^3/h. Detailed results can be seen in **Appendix 1B**.

Table 8. Cut volume, cutting time and productivity in each strip

Strip	Layer index	Measured volume (m^3)	Cutting time	Cutting productivity (m^3/h)
1	2	185.7	00:48:37	229.2
2	1	179.4	01:01:02	176.3
3	4	187.9	01:30:24	124.7
4	5	180.7	00:45:03	240.6
5	5	184.6	00:45:30	243.4
6	5	177.8	00:48:34	219.7
7	6	144.8	00:34:30	251.8

5.8. Computational production rate

The cutting modelling by Dr. Lemm estimated specific energy consumption in 12 different conditions, which can be seen in **Table 9** (strips 4…6 have identical values, as they were all in layer 5). The range of specific energy consumption was 4,84…10 kW/m^3 for new picks and 10,03…25,98 kW/m^3 for old picks. The value difference between layers mirrors the difference in UCS values. The specific energy consumption in the worst-case conditions is expectedly higher than in the case of average conditions, as is the energy consumption with worn picks, compared to the new picks.

Table 9. Specific energy consumption (kWh/m^3) in based on rock properties and pick condition

Strip		**3**	**4**	**5**	**6**	**7**
Layer		**4**	**5**	**5**	**5**	**6**
New pick	**Avg.**	4.84	5.43	5.43	5.43	7.97
	Max.	8.41	7.02	7.02	7.02	10.00
Worn pick	**Avg.**	10.03	12.48	12.48	12.48	16.96
	Max.	17.31	18.87	18.87	18.87	25.98

Based on the cutting time, measured volume and the engine power of the surface miner (783 kW), total energy consumption for each strip was calculated (**Table 10**). In this case, the calculation was done with the assumption of 100% energy consumption for the cutting drum. The specific energy consumption based on actual measured values is between 3,11…6,28 kW/m^3.

Table 10. Specific energy consumption of each mined strip based measured values

Strip	**3**	**4**	**5**	**6**	**7**
Layer	**4**	**5**	**5**	**5**	**6**
Cutting time	01:30:24	00:45:03	00:45:30	00:48:34	00:34:30
Measured volume (m^3)	187.9	180.7	184.6	177.8	144.8
Total energy consumption (kWh)	1179.7	587.9	593.8	633.8	450.2
Specific energy consumption (kWh/m^3)	6.28	3.25	3.22	3.56	3.11

As can be seen, there is a significant difference between the modelled specific energy consumption compared to values calculated from field measurements (**Table 11**). This was expected, since the model assumes a solid, undisturbed rock mass in its calculations, therefore a correction factor of 1,9 was applied, as explained in chapter 4.10.

Table 11. Deviation between specific energy consumption based on field measurements and computationally modelled specific energy consumption

Strip	**3**	**4**	**5**	**6**	**7**
Layer	**4**	**5**	**5**	**5**	**6**
New pick	-23%	67%	69%	52%	156%
Worn pick	60%	283%	288%	250%	445%
Average	18%	175%	178%	151%	301%

The corrected specific energy values (**Table 12**) ranged from 2,55…4,19 kW/m^3 with new picks and 5,28…8,93 kW/m^3 with worn picks. The values deviated from those in **Table 10** by -59…35% in the case of new picks and -16…187% in the case of worn picks. The lowest deviation was with new picks in layer 5, ranging from -20…-11%.

Table 12. Modelled specific energy values after applying correction factor along with the deviation from measured value

Strip	**3**	**4**	**5**	**6**	**7**
Layer	**4**	**5**	**5**	**5**	**6**
New pick	2.55	2.86	2.86	2.86	4.19
Deviation	-59%	-12%	-11%	-20%	35%
Worn pick	5.28	6.57	6.57	6.57	8.93
Deviation	-16%	102%	104%	84%	187%

After calculating production rates using the corrected modelled specific energy consumption values, the cutting performance for new picks ranges from 186,7…307,4 m^3/h and for worn picks between 87,7…148,3 m^3/h (**Table 13**). A pick wear factor was found, based on pick condition on the cutting drum. After interpolating between the values based on the measured pick wear factor (0,2), the modelled cutting rates are 275,6 m^3/h, 243,0 m^3/h and 166,9 m^3/h for layers 4, 5 and 6 respectively. The deviation is nearly non-existent in strips 4 and 5, and very low in strip 6 (+11%), which were all layer 5 measurements. In layers 4 and 6 the deviation is +121% and -34% respectively.

Table 13. Production rates based on corrected specific energy; the interpolated value between new and worn pick production rate based on pick wear factor and the deviation from measured results

Strip	**3**	**4**	**5**	**6**	**7**
Layer	**4**	**5**	**5**	**5**	**6**
New pick	307.4	274.0	274.0	274.0	186.7
Worn pick	148.3	119.2	119.2	119.2	87.7
Interpolated	275.6	243.0	243.0	243.0	166.9
Deviation	+121%	+1%	-0%	+11%	-34%

6. Discussion

In this chapter, the results of the experiments are critically reviewed and compared to prior research. Connections between different parameters are discussed and interpretations are made from any correlations. Possible explanations are given for any deviations from expected outcomes. In the end of the chapter, future research possibilities are discussed.

6.1. Sampling

The samples were extracted from the same layers in which the surface miner was operating. However, the material was taken from a singular point (two points close to each other in the case of layer 6), therefore they may not be representative of the layer as a whole. To account for any geological variation, samples should ideally be taken from multiple points throughout the same layer. This however would have required tools which were not available at the time.

6.2. Mechanical properties of the rock layers

Compressive strength

A total of 92 UCS samples were tested from 3 layers, which is enough repetitions for statistical analysis. The compressive strength range found through experiments is within believable boundaries for kerogenous Estonian limestones (between 20…120 MPa) (Pastarus et al., 2008; Reinsalu et al., 2014). The difference in strength between the layers (65% increase in compressive strength in layer 6 compared to 4) is caused by the presence of kukersite layers in the limestone, because the soft shale acts as a localized weakness within the rock. A clear correlation between the visual abundance of kukersite and compressive strength could be seen.

Unexpectedly, the vertically drilled cores had the lowest average compressive strength in all layers, while horizontally drilled cores had the highest, despite studies on limestones (Liu et al., 2023; Mo et al., 2022) and other layered anisotropic rocks (Chu et al., 2020; Liu et al., 2023; Song et al., 2018; You et al., 2021) have found the compressive strength to be highest when compressing perpendicular to layering and lowest when the load is diagonal to bedding planes. This effect of anisotropy is most apparent in layer 6.

This could be the result of the interbedded oil shale. Since the oil shale in mechanically much weaker, whenever the cores are compressed perpendicular to bedding, the oil shale inclusions are preferentially crushed leading to the failure of the entire sample. In the case of horizontal cores however, the layers are parallel to the loading axis, meaning that the stronger limestone layers can support the load, thus leading to higher strength.

This could also be caused by sampling bias, as when drilling cores vertically, the core includes all the layers within the cross-section of the rock, including the weaker oil shale interbeds. However, when drilling horizontal cores, the core might be situated entirely within a stronger or a weaker rock horizon. This would also explain why horizontal cores had the widest distribution of compressive strength values.

Some cores for layers 4 and 5 were cut with a 1:1 length to diameter ratio. With an increase in length, the compressive strength decreases rapidly, until reaching a L/D ratio of around 2,5:1, after which the UCS value stabilizes (Sadeghi et al., 2022; Sujatono, 2024; Tuncay & Hasancebi, 2009). Specifically for limestone, Sujatono (2024) has suggested an optimal L/D ratio of 2,2:1. However for this thesis, a higher L/D ratio than 2:1 would have been difficult to achieve, as the lithology prevented from cutting enough cores of sufficient length.

1:1 ratio cores in our experiments showed a consistently higher average compressive strength than the regular 2:1 ratio cores, as was expected. A correction formula given by Tuncay & Hasancebi (2009) was applied to the UCS values, however the results were still on average noticeably higher than those of 2:1 cores. This formula cannot be used reliably in this type of lithology. Though outside the scope of this study, modifications should be made to the formula to make it usable in this geological setting.

Elastic modulus

The value range of elastic modulus in the samples is within reasonable limits for Estonian limestones of the Viivikonna formation (4…37 GPa) (Reinsalu et al., 2014); similar values have been found for limestones in other geological settings as well (Liu et al., 2023; Sadeghi et al., 2022; Sujatono, 2024). The elastic modulus values followed the same general trends as the UCS values. As can be seen in **Figure 26**, there is moderate correlation between the elastic modulus and compressive strength of the samples, with an R^2 = 0,61, which explains the similar distribution trends.

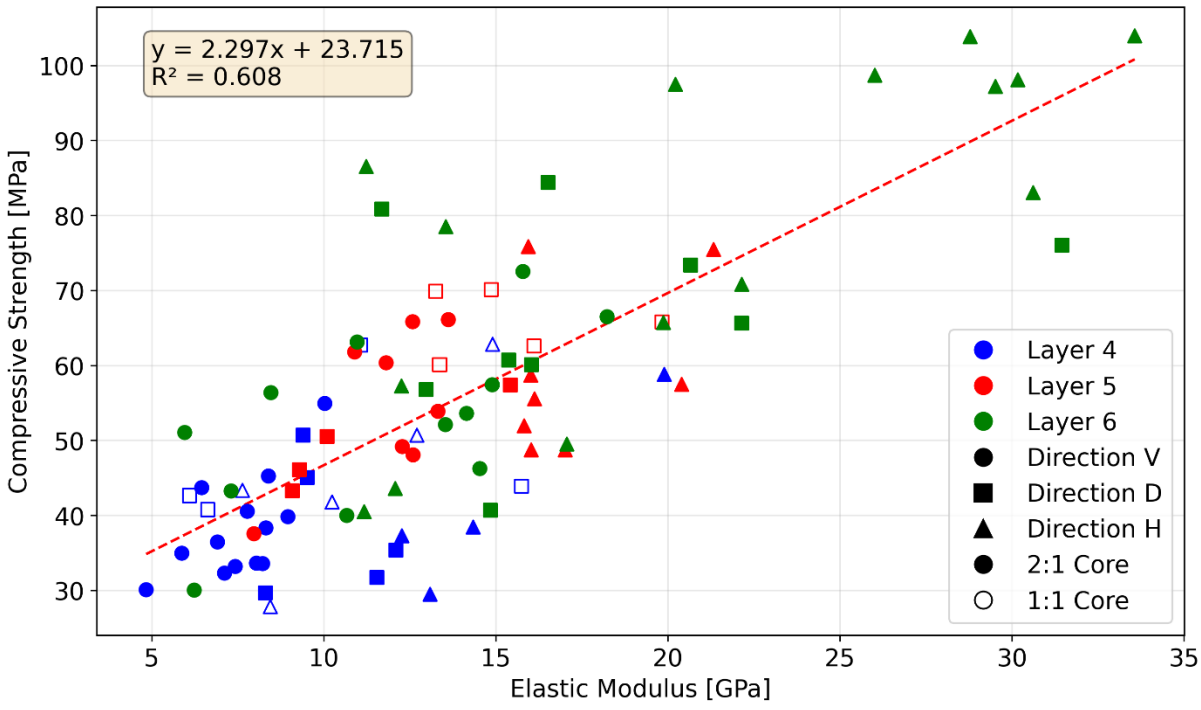

Figure 26. Correlation between the UCS and elastic modulus values

The correlation between UCS and elastic modulus can vary significantly between different rock formations, results of this thesis are on the lower end of this range (Palchik, 2011; Wen et al., 2019). The lower correlation coefficient in this study can be explained by the testing methodology. Instead of using strain gauges to measure the deformation, a displacement sensor attached to the hydraulic

cylinder was used to evaluate the strain. This method has flaws however, since the sensor also measures any deformations to the cylinder and platens themselves during the test, thus introducing variance into the results.

Tensile strength

The range of splitting tensile strength values found in testing fall within expected bounds (2…10 MPa) for Estonian rocks, according to Reinsalu et al. (2014). Prior research on limestones in general also supports this value range (Packulak et al., 2025; Zhong et al., 2020). When comparing tensile strength values, one should differentiate between Brazilian Tensile Strength (BTS) test and Direct Tensile Strength (DTS) test results. BTS test tends to overestimate the tensile strength of the rock; furthermore, anisotropic rocks may not follow predicted behaviour characteristic to isotropic rocks (Packulak et al., 2024). True tensile strength for carbonate rocks can be on average 75% of the measured BTS value (Packulak et al., 2025).

On a layer basis, the BTS values follow the same trend as UCS values. There seem to be no strong correlations between loading direction and tensile strength. Moreover, the results show unexpected behaviour. Studies indicate, that the rock is mechanically weakest when the tensile forces are acting perpendicular to the layering (Horizontal II in **Figure 16**) and the strongest when the forces are pulling parallel to bedding (Horizontal = in **Figure 16**) (Packulak et al., 2024; Tao et al., 2026; Zhong et al., 2020). However, in layers 4 and 6, the opposite is observed. The highest average tensile strength in layers 5 and 6 is shown in the case of diagonally applied tension, which again contradicts expected behaviour.

This seemingly random and uncharacteristic behaviour could be explained by the high heterogeneity of the rock and low sample volume for any given loading condition. Since the rock layers contain quite thick oil shale interlayers and BTS samples are small, some samples consisted mostly of oil shale, while other were mainly limestone. Thus, there was high degree of variance in the strength of a rock even within a single layer and loading condition.

When comparing the compressive and tensile strength along a single axis, a moderate correlation can be found as seen in **Figure 27**, though studies would suggest a much higher correlation between the two parameters (Nazir et al., 2013; Sadeghi et al., 2022). The low correlation value can be attributed to the heterogeneity of the rock. Due to the low amount of data points, no concrete conclusions can be made.

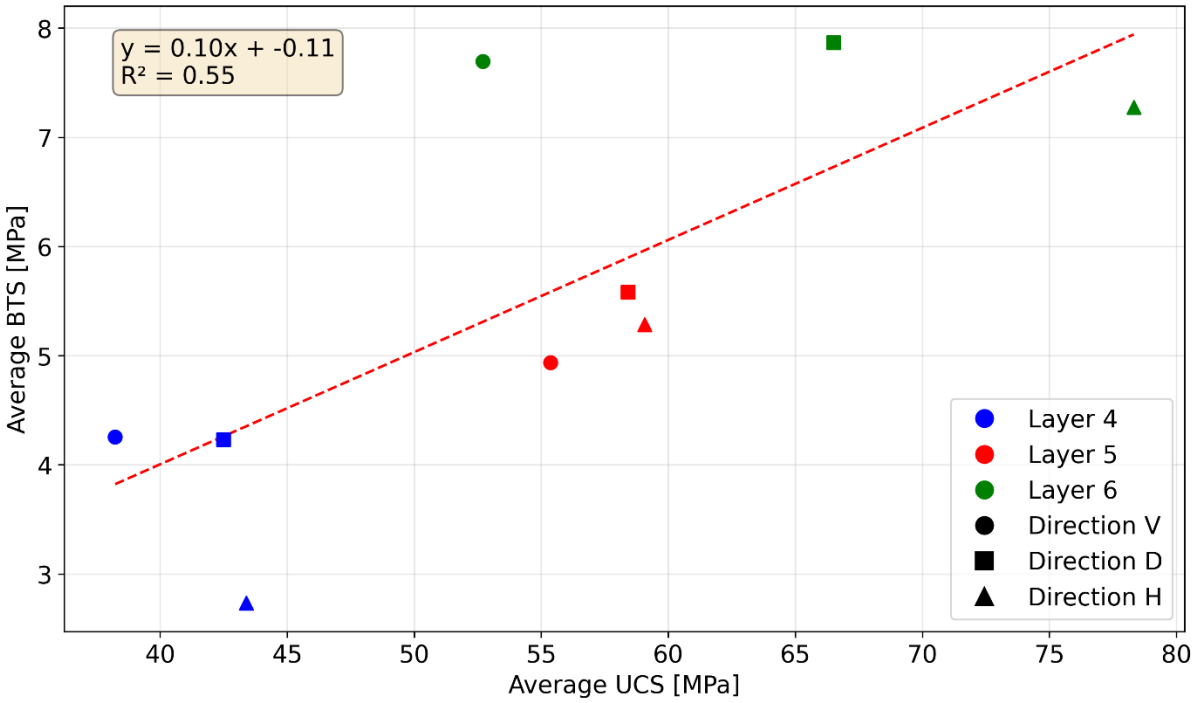

Figure 27. Correlation between UCS and BTS values

Poisson's ratio

The average Poisson's ratio in all layers fits within reasonable bounds for its lithology (average of 0,23 compared to 0,24 in literature (Reinsalu et al., 2014)), though individual data points can show lower values than expected. In general, the values fit the expected bounds for carbonate rocks (Liu et al., 2023; Palchik, 2011; Sujatono, 2024; Wen et al., 2019).

The average Poisson's ratio in every layer converges around 0,23. Layers 4 and 5 show high degree of variance in individual results, while layer 6 has quite consistent values throughout. This can be attributed to the high heterogeneity of layers 4 and 5. Layer 6 cores in comparison were more homogenous and therefore had more consistent results.

Bedding orientation influences the Poisson's ratio, as in vertical cores, values tended to be on the lower end of the range, and in horizontal cores at the higher end in all layers. However, more samples in each direction would need to be tested to draw concrete conclusions.

There seems to be no correlation between Poisson's ratio with neither compressive strength nor elastic modulus (**Figure 28**). This is in contrast to previous research on different sedimentary rocks (Arslan et al., 2008; Wen et al., 2019; You et al., 2021), though some studies have found a similar lack of correlation between these values (Jamshidi et al., 2014).

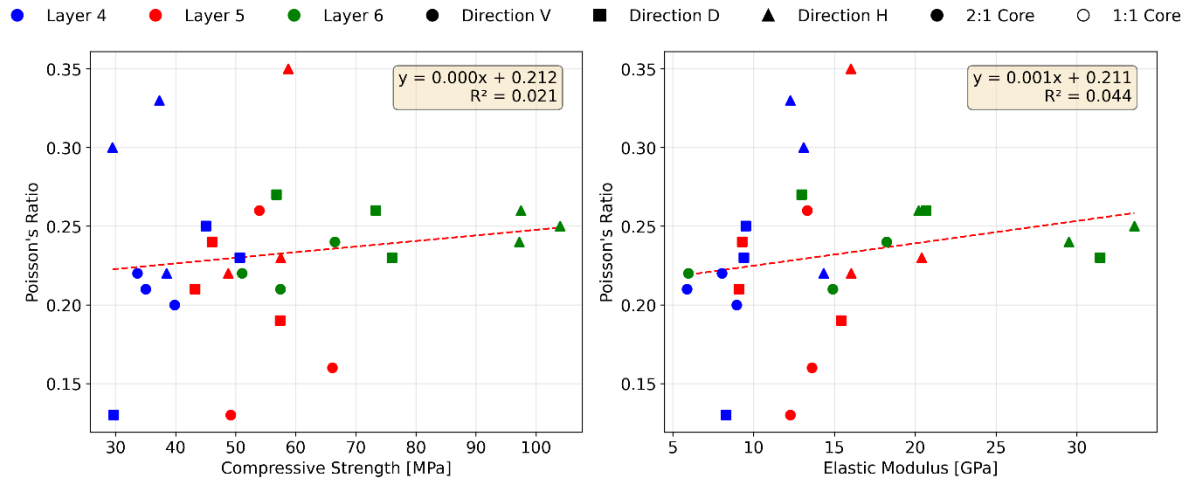

Figure 28. Correlations between different parameters. **Left** – compressive strength and Poisson's ratio; **Right** – clastic modulus and Poisson's ratio

The Poisson's ratio was determined by measuring the speeds of P- and S-waves generated with an ultrasonic pulse generator. Heterogeneities of the rocks, including layering, microfractures, porosity etc., increase variability of ultrasonic wave propagation and thus the calculation of Poisson's ratio (Kłopotowska, 2018). Precise positioning of the transducers is also a factor, along with the couplant used during testing (Vaneghi et al., 2021; Xu et al., 2024).

Operator error can also play a role in the variance of the results. While the P-wave was detected by the software automatically, the S-wave was marked by the operator on a wave graph. This means that the result can vary slightly depending on where the beginning of the S-wave is indicated to be, especially when the received signal quality is poor. While these introduced variances mean that a completely accurate Poisson's ratio value can't be determined for a singular sample, across multiple samples a believable average value can still be achieved.

Abrasivity

The average CERCHAR values in all samples were quite similar (0,36…0,45), with only PK5 sample showing a larger difference from other samples. The CAI value was expectedly low, as carbonate rocks have low abrasivity (Dipova, 2012).

There is no discernible relation between the lithology and CAI value. No correlation can be seen in the pin dragging direction either – in samples PK4 and PK6A, perpendicularly drawn pins had a lower average wear and pins dragged along the layering had higher average wear. In samples PK5 and PK6B the opposite was observed.

The EQV of the samples were higher than those seen in pure limestones (Aderhold et al., 2023), though the inclusion of oil shale in the samples explains the elevated values, as oil shale contains terrigenous material. This is apparent when comparing the oil shale content in the different layers to the equivalent quartz content.

Higher concentration of abrasive terrigenous minerals in the oil shale bearing layers would imply a higher abrasiveness as well, which is what has been reported in previous studies (Reinsalu et al., 2014).

This has also been indicated by the surface miner operators, who claimed that cutting oil shale requires more frequent change of picks. Abrasive action of the microcrystalline quartz in the rock layers at the Põhja-Kiviõli mine would also explain the “polishing” of the cutting drum and picks of the surface miner.

Between the two factors, there seems to be no positive correlation, as indicated by **Figure 29**. In fact, there is a negative correlation between the average CAI and the quartz equivalent value and a stronger negative correlation between perpendicularly dragged pins and the quartz equivalent value. As the limestone in this study is soft, CERCHAR test does not give as accurate results, compared to harder rocks.

Due to the nature of the CERCHAR test, only a small area is affected by one pin. Therefore, in heavily heterogeneous rocks, more samples should be tested per layer or more pins should be used per sample. Also, careful consideration should be put into selecting representative samples.

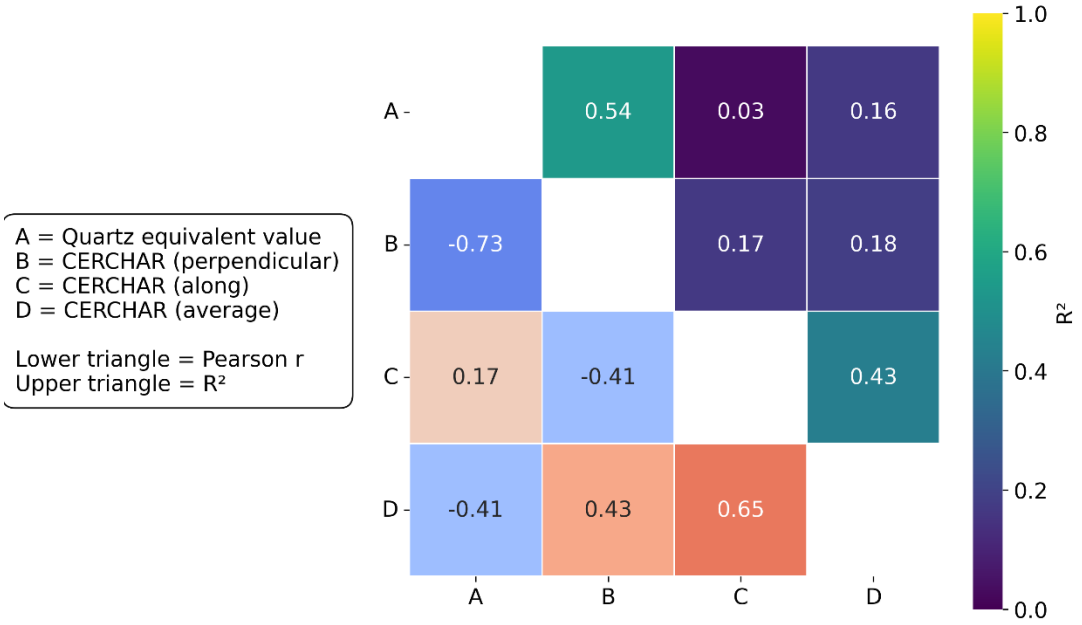

Figure 29. Correlation matrix of the mineral content and abrasivity indices

There are no apparent correlations between the CAI and rock mechanical properties, though such a connection would be expected (Teymen, 2020). There is however a negative correlation between the quartz equivalent value and the mechanical properties of the rock, due to the value being associated with the presence of oil shale, which in turn affects the behaviour of the rock.

6.3. Pick wear patterns

Around half of all discarded picks showed asymmetrical (one-sided) wear pattern. This shows that the picks are prone to getting stuck in position and not rotating, leading to uneven wear and premature failure. This is caused by the tool holder being blocked by fine-grained material, of which there is an abundance of due to the oil shale content in the rock. Yasar et al. (2023) showed that changing the angle or using springs might improve the rotation of picks, though more research would be needed to say whether this is applicable in this case.

The second most common wear pattern was carbide tip failure. According to Thuro & Plinninger (2002), this is caused mainly by the geology, rock strength and machine factors. This sort of breakage could be attributed to stronger layers (such as layer 6), where the compressive strength can be significantly higher than adjacent layers. This could be mitigated, by lowering speed in more difficult layers and thus reducing the forces acting on the picks. This of course lowers the production rate, so a compromise must be made. Carbide tip breaking could be somewhat lessened also by changing worn picks more proactively and thus reducing the load on non-broken picks.

The third wear pattern most common in discarded picks was carbide tip breakout due to pick wear. In general, the preferential wear of the steel body of the pick is the most common wear seen in picks on the cutting drum. As reported by Thuro & Plinninger, this pattern is typical to low-strength rocks, since the rock breaks into smaller fragments and therefore the body of the pick comes into contact with rock particles more frequently. The lower hardness of the steel in turn leads to higher wear compared to the carbide tip. This explanation suits the type of geology seen at the mine.

In general, the wear seen in both discarded picks and those still in use on the drum show that a majority of the picks are not used to their full potential. Wear to the pick body leads to premature breakout of the carbide tip, while in harder rock, the carbide pins can suffer brittle failure. In both cases, the carbide tip, and therefore the main cutting tool, is lost, leading to lower cutting performance. Moreover, when one pick fails, the adjacent picks encounter higher forces, increasing the chance of those breaking too, which can lead to a cascading failure. This shows that there is room for optimization of the picks for this specific locality.

6.4. Surface miner productivity

Measured productivity

As the calculated volumes were similar in all strips, the values can be considered reliable. The highest cutting performance was recorded in layer 6, while the lowest in layer 4. This contradicts the laboratory test results, where layer 6 showed the highest UCS, BTS and elastic modulus values, whereas layer 4 was the weakest layer.

This contradiction in layer 4 can be best explained by operational, rather than lithological factors. The surface miner was experiencing mechanical issues, evidenced by the repeated stops by the operator. This would have influenced the machine performance. Furthermore, the operator switched out picks after cutting layer 4, which would have improved the cutting rate in layers 5 and 6. However, geological influence can not be entirely dismissed; as there was only one measurement in layer 4, it can not be said for certain, how representative the production rate was.

In layer 6 however, the difference from expected results cannot be reliably explained by machine factors and therefore must be related to rock mass parameters. Layer 6 samples were taken from loosened slabs of rock, up to around 20 cm thick. The layer itself was 40 cm thick, meaning the samples possibly did not represent the layer as a whole. Significant heterogeneity of the rock mass could explain the higher production rate. As with layer 4, the singular measurement precludes reliable assessment of the representativity of the cutting performance in layer 6.

Comparison to prior works

A prior study in 2009 on surface miner productivity outlined by Väizene et al. (2013) reported a cutting production rate of 379,4 m^3/h using a Wirtgen 2500 SM. This is significantly higher than the maximum value of 251,8 m^3/h reached in this study. There are several factors which can cause this difference.

The main factors which would explain the performance variance is rock mass properties. Though the cut layer in the 2009. study is designated as "H/J" which would put it above the oil shale layer "H" same as in the current study, the exact position of the layer is unknown. As can be seen from the current study, rock mechanical properties can change drastically with little vertical distance. Therefore, the limestone mined in the 2009 study was most likely weaker. However, other factors cannot be ruled out either, such as differences in pick conditions, state of repair of the machine and even operator skill and performance.

Modelled productivity

The Dr. Lemm model overestimated the specific energy consumption during cutting compared to field observations, regardless of pick wear. This was expected, as the model assumes a homogeneous rock mass, while the actual rock layer contains weakness planes, such as cracks, and mechanically weaker oil shale interlayers. After applying the correction factor derived from the Wirtgen Surface Mining Manual cutting performance graph, the specific energy consumption was underestimated when modelling with new picks and overestimated when modelling with worn picks. Inversely, the cutting performance was overestimated with new picks and underestimated with worn picks.

After interpolating between the new pick and worn pick values based on the pick wear factor, the final production rate estimations improved drastically, with almost no deviation in layer 5 compared to field measurements. In layers 4 and 6 however, the estimation is still off by a significant factor. This can be explained by the same reasons outlined in the previous section.

This shows us that while mechanical properties of the rock, such as UCS, play an important part in cutting performance, other factors have a key role as well. The model cannot account for all possible aspects affecting cutting performance. The state of repair of the surface miner itself, along with operator skill can significantly affect machine performance. Furthermore, the model does not currently take rock mass condition into account, which as can be seen, has a significant effect on the cutting performance. To make the model more reliable, rock mass properties, such as Rock Quality Designation should be implemented.

It should be noted that correction factor derived from the Surface Mining Manual is a very rough estimate, and though it led to a believable result in this case, it may not be applicable in every lithology. Furthermore, the pick wear factor, which is based on the visual inspection of picks, is largely subjective and can vary a lot depending on the observer. This would lead to notable differences in estimations; therefore, a more scientific and repeatable method should be created to estimate pick wear and ideally added to the model calculations.

Overall, the initial results of the model seem promising; however, there is currently a lack of reliable real-world measurement data to compare the modelling results to. More field measurements should be conducted before the model can be properly assessed.

Summary

This thesis evaluates the applicability of a cutting performance model developed by Dr. Andreas Lemm for predicting the productivity of a surface miner in Estonian conditions. This work is part of the Tem-TA143 project, the aim of which is to study alternative methods for more sustainable mining of construction minerals. Surface miners offer a potentially sustainable alternative for selective mechanical excavation, but their performance depends strongly on rock properties, machine parameters and rock mass conditions, which are not fully captured in existing predictive models.

In this study, field work was conducted at the Põhja-Kiviõli II oil shale mine to gather performance data of the Wirtgen 280 SMi surface miner to form a baseline for comparison with the model. Samples were extracted from the mine site from three distinct layers to evaluate the mechanical properties of the rock. The parameters studied by laboratory tests included uniaxial compressive strength (UCS), Brazilian tensile strength (BTS), elastic modulus, Poisson's ratio and abrasivity by the CERCHAR method. Additionally, chemical and mineralogical composition of the rocks was determined through XRF and XRD analyses to find the quartz equivalent content of the samples. There parameters were used to characterize the rock and to study the anisotropic effects of layering.

The results show significant variability in mechanical properties between layers, with UCS ranging from around 30 to over 100 MPa and elastic modulus from around 5 to over 33 GPa. Tensile strength values ranged from about 2 to 10 MPa and broadly followed UCS trends, although correlations were weakened by strong heterogeneity of the rock and the presence of oil shale interbeds. Poisson's ratio values were relatively consistent (average 0,23), while CERCHAR abrasivity remained low across all samples (average CAI 0,42), consistent with predominantly carbonate lithology. However, pick wear analysis showed frequent asymmetrical wear and carbide tip failures, suggesting significant operational impacts from fine-grained material and pick rotation issues.

Measured surface miner productivity varied between roughly 125 and 252 m^3/h, with an average around 212 m^3/h. In contrast, initial model predictions overestimated specific energy consumption and therefore underestimated productivity when rock mass effects were not included. After applying correction factors for rock mass conditions and incorporating the pick wear factor, model predictions improved significantly, particularly for layer 5. However, discrepancies remained in layers 4 and 6, stemming from heterogeneity of the rock and mechanical difficulties of the machine.

Overall, the Lemm model shows promising results in predicting the surface miner performance in Estonian conditions, though more studies would need to be conducted to solidify this position. Further development could be done on the model as well, key improvements being incorporation of rock mass influence into the calculations. A more objective way of assessing pick wear is necessary as well. The study concludes that while mechanical rock properties are essential inputs, rock mass heterogeneity and field-scale operational conditions are equally critical in accurately predicting surface miner productivity.

Acknowledgements

First and foremost, I would like to thank my supervisor Dr. Bruno Grafe, who offered me this subject for research. His experience and knowledge were invaluable for this work, and his guidance got me through this thesis. I would also like to thank my co-supervisor Sander Kanter, who assisted in sampling and other tasks, and who gave valuable input in our project discussions.

I would like to offer my gratitude to Dr. Andreas Lemm, on who's model this thesis is mainly based on and who very kindly used his model to run our calculations. Dr. Lemm's vast knowledge of the cutting process was vital to this work, as it helped us plan our testing procedures and methods.

My fellow master's student Reet Männik was an exceptional assistant during the sample preparation and testing processes. She helped keep me on track throughout the whole thesis and never forgot to remind me of important deadlines, which I myself had forgotten about. She was always willing to bounce ideas back and forth and her cheerful disposition brightened up even the dullest days of work.

I want to thank my boss and head of the Mining Division at the Department of Geology, Dr. Erik Väli, who invited me to join this project. I would also like to thank the Estonian Research Council for funding this project. In addition, I am grateful to Kiviõli Keemiatööstus and especially Kaidi Sulp for having me at their mine and offering their support in my work.

Toivo Kallaste, Nata-Ly Pantšenko and Erki Leht are also deserving of thanks, for their work on the geochemical and mineralogical analysis. As is Kristina Vilba from the Department of Civil Engineering and Architecture, who kindly let us borrow their equipment for testing purposes. I would also like to thank the surface miner operator Urmas at the Põhja-Kiviõli mine, who offered insight into the operation of the machine.

And finally, I offer my sincerest gratitude to all my family, friends and coworkers, too numerous to name them all, for their unwavering support throughout my whole journey at the university.

References

Aderhold, M., Disselkamp, C., Formanski, R., Grimberg, M., Grineisen, A. M., Kroenert, L. M., Ogan, M. S., Romahn, H., Sandkühler, R., Skonetzki, C., Ullah, F., Zinke, B. H., Duda, M., Witte, L. C., Brajer, C., & Backers, T. (2023). Comparison of different methods to characterise the abrasivity potential and mechanical properties of carbonates with respect to its relevance for practical purposes in excavation technologies. *IOP Conference Series: Earth and Environmental Science*, *1124*(1), 012044. https://doi.org/10.1088/1755-1315/1124/1/012044

Alber, M., Yaralı, O., Dahl, F., Bruland, A., Käsling, H., Michalakopoulos, T. N., Cardu, M., Hagan, P., Aydın, H., & Özarslan, A. (2014). ISRM Suggested Method for Determining the Abrasivity of Rock by the CERCHAR Abrasivity Test. *Rock Mechanics and Rock Engineering*, *47*(1), 261–266. https://doi.org/10.1007/s00603-013-0518-0

Amaral, P. M., Rosa, L. G., & Fernandes, J. C. (2005). Experimental Evaluation of Dynamic Test Methodologies for Assessing the Elastic Constants of Granitic Rocks. *Journal of Nondestructive Evaluation*, *24*(4), 135–142. https://doi.org/10.1007/s10921-005-8781-y

Arslan, A. T., Koca, M. Y., Aydogmus, T., Klapperich, H., & Yılmaz, H. R. (2008). Correlation of Unconfined Compressive Strength with Young's Modulus and Poisson's Ratio in Gypsum from Sivas (Turkey). *Rock Mechanics and Rock Engineering*, *41*(6), 941–950. https://doi.org/10.1007/s00603-007-0145-8

Bauert, H., & Hints, O. (2024). Stop 4: Põhja-Kiviõli II open-pit mine. In O. Hints, P. Männik, & U. Toom (Eds.), *XI Baltic Stratigraphical Conference. Abstracts and Field Guide* (pp. 83–90). Geological Society of Estonia. https://kirjandus.geoloogia.info/en/reference/49824

Bauert, H., Tamm, J., Liivamägi, S., Hade, S., Kaasik, T., & Kattai, V. (2018). *Ehitusmaavarade levik, kaevandamine ja kasutamine Harju maakonnas*. Eesti Geoloogiateenistus.

Bieniawski, Z. T., & Bernede, M. J. (1979). Suggested methods for determining the uniaxial compressive strength and deformability of rock materials. *International Journal of Rock Mechanics and Mining Sciences & Geomechanics Abstracts*, *16*(2), 137–138.

Bieniawski, Z. T., & Hawkes, I. (1978). Suggested methods for determining tensile strength of rock materials. *International Journal of Rock Mechanics and Mining Sciences & Geomechanics Abstracts*, *15*(3), 99–103. https://doi.org/10.1016/0148-9062(78)90003-7

Bilgin, N., Balcı, C., Eskikaya, Ş., & Ergunalp, D. (1997). Full scale and small scale cutting tests for equipment selection in a Celestite Mine. In V. Strakoš, V. Kebo, R. Farana, & L. Smutný (Eds.), *Mine Planning and Equipment Selection* (1st ed., pp. 387–392). CRC Press. https://doi.org/10.1201/9781003078166-67

CEN. (2021). *Testing concrete in structures—Part 4: Determination of ultrasonic pulse velocity* (EN 12504-4:2021).

Chu, C., Wu, S., Zhang, S., Guo, P., & Zhang, M. (2020). Mechanical behavior anisotropy and fracture characteristics of bedded sandstone. *Zhongnan Daxue Xuebao (Ziran Kexue Ban)/Journal of Central South University (Science and Technology)*, *51*(8), 2232–2246. https://doi.org/10.11817/j.issn.1672-7207.2020.08.018

Department of Mining. (2012). *Vermeer freeskombain*. Department of Geology Archive.

Dipova, N. (2012). Investigation of the relationships between abrasiveness and strength properties of weak limestones along a tunnel route. *Jeoloji Muhendisligi Dergisi*, *36*(1), 23–34.

Directindustry. (2026). *Surface miner* [Graphic]. https://img.directindustry.com/images_di/photo-g/58547-7578335.webp

Geodeetiline Süsteem [Geodetic System], RT I, 28.12.2024 (2025). https://www.riigiteataja.ee/akt/128122024053?leiaKehtiv

Grafe, B. (2022). *Cutting Force Component-Based Rock Differentiation Utilising Machine Learning*. https://doi.org/10.13140/RG.2.2.10463.88484

Hartlieb, P., & Bock, S. (2018). Theoretical Investigations on the Influence of Artificially Altered Rock Mass Properties on Mechanical Excavation. *Rock Mechanics and Rock Engineering*, *51*(3), 801–809. https://doi.org/10.1007/s00603-017-1355-3

Hu, G., Wang, B., Guo, W., Xing, Y., Zhou, J., Zha, L., & Meng, S. (2024). Study on the size effect of rock elastic modulus considering the influence of joint roughness. *Frontiers in Materials*, *11*. https://doi.org/10.3389/fmats.2024.1367006

Hutchins, J., & Oppelaar, S. (2016). Precision Surface Mining, the Next Steps. *Procedia Engineering, SYMPHOS 2015 - 3rd International Symposium on Innovation and Technology in the Phosphate Industry*, *138*, 40–48. https://doi.org/10.1016/j.proeng.2016.02.050

Jamshidi, A., & Akbay, D. (2025). A Comparative Investigation on the Brazilian Tensile Strength (BTS) of the Various Rocks and Development a BTS-Based Rock Classification. *Journal of Mining and Environment*, *16*(4), 1297–1318. https://doi.org/10.22044/jme.2025.15591.2989

Jamshidi, A., Nikudel, M., & Khamehchiyan, M. (2014). Investigating the Effect of Specimen Diameter Size on Uniaxial Compressive Strength and Elastic Properties of Travertines. *Journal of Sciences, Islamic Republic of Iran*, *25*, 135–143.

Jones, I., & Kramadibrata, S. (1995). An excavating power model for continuous surface miners. *AusIMM Proceedings*, *300*.

Kaspar, M., & Latal, C. (2022). Der äquivalente Quarzgehalt – Historischer Rückblick und seine Zukunft in der Anwendung der Abrasivitätsprognose. *geotechnik*, *45*(2), 86–97. https://doi.org/10.1002/gete.202100023

Kiviõli Keemiatööstus. (2026a). *Ajalugu*. KKT - 100 Aastat Väge.

Kiviõli Keemiatööstus. (2026b, March 26). *Wirtgeni kombain läheb appi Rail Balticu ehitusele*. KKT. https://www.keemiatoostus.ee/uudised/wirtgeni-kombain-laheb-appi-rail-balticu-ehitusele/

Kliimaministeerium. (2021). *General principles of Earth's crust policy until 2050*. https://kliimaministeerium.ee/sites/default/files/documents/2021-06/General%20principles%20of%20Earth%E2%80%99s%20crust%20policy%20until%202050%20%28eng%29.pdf

Kliimaministeerium. (2026, May 19). *Ehitusmaavarad*. https://kliimaministeerium.ee/energeetika-maavarad/maavarad/ehitusmaavarad

Kłopotowska, A. (2018). Ultrasonic constraint of the microfracture anisotropy of flysch rocks from the Podhale Synclinorium (Poland). *International Journal of Earth Sciences*, *107*(6), 1941–1953. https://doi.org/10.1007/s00531-017-1579-1

Lemm, A. (2016). *Die absetzbare Schneidleistung in Abhängigkeit der Kräfteverhältnisse an Schneidwerkzeugen* [Dissertation]. Bergakademie Freiberg.

Liu, M., Luo, X., Bi, R., Zhou, J., & Du, K. (2023). Impacts of bedding angle and cementation type of bedding planes on mechanical behavior of thin-layer structured bedded rocks under uniaxial compression. *Geomechanics for Energy and the Environment*, *35*, 100473. https://doi.org/10.1016/j.gete.2023.100473

Männil, R. (1984). О стратиграфической схеме расчленения кукрузеского горизонта в стратотипической области [On the stratigraphic scheme of dissection of the kukruzesky

horizon in the stratotypical region]. *Proceedings of the Academy of Sciences of the Estonian SSR. Geology*, *33*(2), 46–54. https://doi.org/10.3176/geol.1984.2.02

Mo, Y., Zuo, S., & Wang, L. (2022). Mechanical characteristics of thick-bedded limestone with different bedding angles subjected to acid corrosion. *Bulletin of Engineering Geology and the Environment*, *81*(4), 166. https://doi.org/10.1007/s10064-022-02667-2

Mucha, K. (2023). Application of Rock Abrasiveness and Rock Abrasivity Test Methods—A Review. *Sustainability*, *15*(14), 11243. https://doi.org/10.3390/su151411243

Narimani, S., Kovács, L., & Vásárhelyi, B. (2025). An innovative method to determine the stress-dependency of Poisson's ratio of granitic rocks. *Scientific Reports*, *15*(1), 16111. https://doi.org/10.1038/s41598-024-75892-2

Nazir, R., Momeni, E., Jahed Armaghani, D., & Mohd Amin, M. (2013). Correlation between unconfined compressive strength and indirect tensile strength of limestone rock samples. *Electronic Journal of Geotechnical Engineering*, *18 I*, 1737–1746.

Nikitin, O., Väli, E., Sabanov, S., & Pastarus, J.-R. (2007). The surface miner sustainable technology introduction for oil-shale mining in Estonia. *ENVIRONMENT. TECHNOLOGY. RESOURCES. Proceedings of the International Scientific and Practical Conference*, *1*, 55–61. https://doi.org/10.17770/etr2007vol1.1735

Origliasso, C., Cardu, M., & Kecojevic, V. (2014). Surface Miners: Evaluation of the Production Rate and Cutting Performance Based on Rock Properties and Specific Energy. *Rock Mechanics and Rock Engineering*, *47*(2), 757–770. https://doi.org/10.1007/s00603-013-0393-8

Packulak, T. R. M., Day, J. J., McDonald, M. R., Jacksteit, A. C., & Diederichs, M. S. (2025). Measurement of true tensile strength from Brazilian tensile strength laboratory tests. *Canadian Geotechnical Journal*, *62*, 1–14. https://doi.org/10.1139/cgj-2023-0204

Packulak, T. R. M., Gagnon, É., Day, J. J., & Diederichs, M. S. (2024). Effects of Foliation Type and Orientation on Tensile Strength of Low Porosity Rocks. *Geotechnical and Geological Engineering*, *42*(7), 5557–5585. https://doi.org/10.1007/s10706-024-02847-9

Palchik, V. (2011). On the Ratios between Elastic Modulus and Uniaxial Compressive Strength of Heterogeneous Carbonate Rocks. *Rock Mechanics and Rock Engineering*, *44*(1), 121–128. https://doi.org/10.1007/s00603-010-0112-7

Pastarus, J.-R., Adamson, A., Sabanov, S., Väli, E., & Nikitin, O. (2008). Wirtgen 2500 sm ja killustiku tootmime karjäärides. In *Killustiku kaevandamine ja kasutamine* (pp. 26–28). TTÜ mäeinstituut. https://files.geocollections.info/a143bd3e-69d4-481a-a4c5-7c7dca7f5702.pdf

Pradhan, P., & Dey, K. (2009). Productivity improvement through selection of operating mode of surface miner—A computational approach. *J Mines Met Fuels*, *57*(3–4), 67–74.

Prakash, A., & Murthy, V. M. S. R. (2017). Hierarchy of Parameters Influencing Cutting Performance of Surface Miner through Artificial Intelligence and Statistical Methods. *Current Science*, *112*(06), 1242. https://doi.org/10.18520/cs/v112/i06/1242-1249

Prakash, A., Sita Ramachandra Murthy, V. M., & Bahadur Singh, K. (2015). A new rock cuttability index for predicting key performance indicators of surface miners. *International Journal of Rock Mechanics and Mining Sciences*, *77*, 339–347. https://doi.org/10.1016/j.ijrmms.2015.04.016

Proceq. (2022, July). *Determination of Poisson's Ration and the Modulus of Elasticity by measuring with P- and S-wave transducers.*

Reinsalu, E., Anepaio, A., Karu, V., Lüütre, E., Roots, R., Saarnak, M., Sein, O., & Väizene, V. (2014). Nõrkade kihiliste kivimite tugevusomadused. *Mäenduse Strateegiline Planeerimine*, 36–65.

Sadeghi, E., Nikudel, M. R., Khamehchiyan, M., & Kavussi, A. (2022). Estimation of Unconfined Compressive Strength (UCS) of Carbonate Rocks by Index Mechanical Tests and Specimen Size Properties: Central Alborz Zone of Iran. *Rock Mechanics and Rock Engineering*, *55*(1), 125–145. https://doi.org/10.1007/s00603-021-02532-w

Sayankin, A. (1990, September 28). “Кильт”, “Wirtgen” и “красная деревня” ["Kilt", “Wirtgen” and “the red village”]. *Soviet Estonia*, (223), 2.

Shustov, D. V., Kashnikov, Yu. A., Kukhtinskii, A. E., & Efimov, A. A. (2024). On the relationship of Poisson’s ratio with geophysical characteristics of rocks. *Georesources*, *26*(2), 69–75. https://doi.org/10.18599/grs.2024.2.7

Singh, O. P., P Y, D., & Pradhan, M. (2025). Bivariate Analysis of the Geotechnical Properties and the Key Performance Indicators of the Surface Miners. *International Journal of Engineering Trends and Technology*, *73*(12), 162–173. https://doi.org/10.14445/22315381/IJETT-V73I12P113

Singh, O. P., P Y, D., Pradhan, M., & Mishra, R. (2026). Stepwise Multiple Regression Analysis for Development of a Model to Predict the Performance of Surface Miners. *International Journal of Engineering Trends and Technology*, *74*(1), 259–274. https://doi.org/10.14445/22315381/IJETT-V74I1P120

Singh, O. P., P Y, D., Pradhan, M., & N, S. (2024). Modelling the Performance Indicators of Surface Miners in Coal Mines using Coal Cuttability Factor. *International Journal of Engineering Trends and Technology*, *72*(4), 238–248. https://doi.org/10.14445/22315381/IJETT-V72I4P125

Song, H., Jiang, Y., Elsworth, D., Zhao, Y., Wang, J., & Liu, B. (2018). Scale effects and strength anisotropy in coal. *International Journal of Coal Geology*, *195*, 37–46. https://doi.org/10.1016/j.coal.2018.05.006

Sujatono, S. (2024). Optimum Length-to-diameter Ratio of Floatstone under Uniaxial Compressive Strength Test. *Geotechnical and Geological Engineering*, *42*(3), 2045–2060. https://doi.org/10.1007/s10706-023-02660-w

Tao, W., Guo, L., Guo, Y., Zhang, J., Zhao, S., Li, S., & Wang, G. (2026). Mechanical Properties and Fracture Evolution of Transversely Isotropic Gneiss Under Tensile Stress. *Rock Mechanics and Rock Engineering*, *59*(4), 4209–4230. https://doi.org/10.1007/s00603-025-04949-z

Teymen, A. (2020). The usability of Cerchar abrasivity index for the estimation of mechanical rock properties. *International Journal of Rock Mechanics and Mining Sciences*, *128*, 104258. https://doi.org/10.1016/j.ijrmms.2020.104258

Thuro, K., & Plinninger, R. J. (2002). Geologisch-felsmechanische Aspekte der Gebirgslösung im Tunnelbau: Bohren, Sprengen, Fräsen [Geological and rock mechanical aspects of rock excavation in tunnel construction: Drilling, blasting, milling]. *Proceedings of the 3rd Colloquium “Bauen in Boden und Fels,”* 35–54. https://www.plinninger.de/images/pdfs/2002_tae_kolloquium.pdf

Tuncay, E., & Hasancebi, N. (2009). The effect of length to diameter ratio of test specimens on the uniaxial compressive strength of rock. *Bulletin of Engineering Geology and the Environment*, *68*(4), 491–497. https://doi.org/10.1007/s10064-009-0227-9

Väizene, V., Valgma, I., Iskül, R., Kolats, M., Nurme, M., & Karu, V. (2013). High selective oil shale mining. *Oil Shale*, *30*(2S), 305–325. https://doi.org/10.3176/oil.2013.2S.10

Väli, E. (2011). Analysis of oil shale high-selective mining with surface miner in estonia. *Oil Shale*, *28*(1), 49–57. https://doi.org/10.3176/oil.2011.1.06

Vaneghi, R. G., Saberhosseini, S. E., Dyskin, A. V., Thoeni, K., Sharifzadeh, M., & Sarmadivaleh, M. (2021). Sources of variability in laboratory rock test results. *Journal of Rock Mechanics and Geotechnical Engineering*, *13*(5), 985–1001. https://doi.org/10.1016/j.jrmge.2021.03.007

Vorona, M. (2012). *Optimierung des Schneidprozesses und Prognose der relevanten Arbeitsgrößen bei der Gesteinszerstörung unter Berücksichtigung des Meißelverschleißes [Optimization of the cutting process and prediction of relevant operating parameters in rock breaking, taking into account bit wear]* [Doctoral dissertation, TU Bergakademie Freiberg]. https://nbn-resolving.org/urn:nbn:de:bsz:105-qucosa-96367

Wen, L., Luo, Z. Q., Yang, S. J., Qin, Y. G., & Wang, W. (2019). Correlation of Geo-Mechanics Parameters with Uniaxial Compressive Strength and P-Wave Velocity on Dolomitic Limestone Using a Statistical Method. *Geotechnical and Geological Engineering*, *37*(2), 1079–1094. https://doi.org/10.1007/s10706-018-0665-x

Wirtgen. (2022). *Wirtgen 280 SMi delivers full performance in the selective mining of different materials*. Wirtgen Group: A John Deere Company. https://www.wirtgen-group.com/en-cn/magazine/the-rock/passion/the-280-smi-delivers-full-performance/

Wirtgen Group. (2017). *WIRTGEN Surface Mining Manual* (2nd ed.).

Xu, R., Beltrán-Gutiérrez, R. E., Käding, M., Lange, A., Marx, S., & Ostermann, J. (2024). Frequency dependent amplitude response of different couplant materials for mounting piezoelectric sensors. *NDT & E International*, *141*, 102993. https://doi.org/10.1016/j.ndteint.2023.102993

Yang, Y., Cheng, H., Liu, M., Haeri, H., Fu, J., & Hou, R. (2024). Numerical Investigation of Rock-Breaking Force Analysis of TBM Disk-Cutters. *Strength of Materials*, *56*(2), 419–430. https://doi.org/10.1007/s11223-024-00659-z

Yasar, S., Odoom, K., Shepel, T., Bretschneider, J., & Drebenstedt, C. (2023). Rotation Enhancement of Conical Picks Coupled with Springs. *Rock Mechanics and Rock Engineering*, *56*(7), 5447–5453. https://doi.org/10.1007/s00603-023-03338-8

You, S., Sun, J., & Wang, H. (2021). Bedding Plane Effects on Mechanical Behavior of Surrounding Rock in Mountain Tunneling. *Shock and Vibration*, *2021*(1), 7346061. https://doi.org/10.1155/2021/7346061

Zajączkowski, M. (2021). Technological and Economic Analysis of the Application of Surface Miner on the Example of a Limestone Deposit in Poland. *Inżynieria Mineralna*, *1*(2). https://doi.org/10.29227/IM-2021-02-21

Zhong, S., Zuo, S., Mao, L., Luo, S., & Wang, X. (2020). Mechanism of anisotropic characteristics of layered limestone and a constitutive model for different bedding angles based on a Brazilian tensile test. *Arabian Journal of Geosciences*, *13*(22), 1228. https://doi.org/10.1007/s12517-020-06222-9

Appendix 1. Surface miner productivity measurement results

Appendix 1A. Cutting time, work time and downtime for each strip

Strip	Layer index	Cutting time		Work time		Downtime		Total time
		hh:mm:ss	%	hh:mm:ss	%	hh:mm:ss	%	
1	2	00:48:37	66%	01:07:12	92%	00:05:55	8%	01:13:07
2	1	01:01:02	79%	01:11:47	93%	00:05:13	7%	01:17:00
3	4	01:30:24	71%	01:55:56	91%	00:12:02	9%	02:07:58
4	5	00:45:03	57%	00:58:31	74%	00:20:21	26%	01:18:52
5	5	00:45:30	78%	00:58:00	100%	00:00:00	0%	00:58:00
6	5	00:48:34	79%	01:01:16	100%	00:00:00	0%	01:01:16
7	6	00:34:30	51%	00:50:09	74%	00:18:02	26%	01:08:11

Appendix 1B. Cutting productivity, real productivity and productivity without downtime

Strip	Layer index	Cutting productivity (m^3/h)	Productivity without downtime (m^3/h)	Real productivity (m^3/h)
1	2	229.2	165.8	152.4
2	1	176.3	149.9	139.8
3	4	124.7	97.2	88.1
4	5	240.6	185.2	137.4
5	5	243.4	190.9	190.9
6	5	219.7	174.1	174.1
7	6	251.8	173.2	127.4

Appendix 2. UCS results

Appendix 2A. Minimum, maximum and average UCS by layer

	All cores	All 2:1 cores	Layer 4 cores	Layer 4 2:1 cores	Layer 5 cores	Layer 5 2:1 cores	Layer 6 cores
N	92	78	31	22	25	20	36
Min	27.82	29.48	27.82	29.48	37.60	37.60	30.03
Max	103.97	103.97	62.80	58.82	75.88	75.88	103.97
Average	55.62	56.05	40.97	38.80	57.65	55.63	66.83

Appendix 2B. Minimum, maximum and average UCS of layer 4 by core direction

	Vertical	Horizontal all cores	Horizontal 2:1 cores	Diagonal all cores	Diagonal 2:1 cores
N	13	9	4	9	5
Min	30.12	27.82	29.48	29.68	29.68
Max	54.96	62.80	58.82	62.70	50.67
Average	38.23	43.39	41.02	42.50	38.50

Appendix 2C. Minimum, maximum and average UCS of layer 5 by core direction

	Vertical	Horizontal	Diagonal all cores	Diagonal 2:1 cores
N	8	8	9	4
Min	37.60	48.73	43.25	43.25
Max	66.10	75.88	70.10	57.40
Average	55.36	59.07	58.42	49.32

Appendix 2D. Minimum, maximum and average UCS of layer 6 by core direction

	Vertical	Horizontal	Diagonal
N	12	15	9
Min	30.03	40.52	40.69
Max	72.54	103.97	84.40
Average	52.70	78.32	66.51

Appendix 3. Elastic modulus results

Appendix 3A. Minimum, maximum and average elastic modulus by layer

	All cores	All 2:1 cores	Layer 4 cores	Layer 4 2:1 cores	Layer 5 cores	Layer 5 2:1 cores	Layer 6 cores
N	92	78	31	22	25	20	36
Min	4842.49	4842.49	4842.49	4842.49	7967.24	7967.24	5952.54
Max	33567.82	33567.82	19895.81	19895.81	21324.66	21324.66	33567.82
Average	13892.00	14193.77	9751.50	9490.18	14203.62	13882.66	17241.03

Appendix 3B. Minimum, maximum and average elastic modulus of layer 4 by core direction

	Vertical	Horizontal all cores	Horizontal 2:1 cores	Diagonal all cores	Diagonal 2:1 cores
N	13	9	4	9	5
Min	4842.49	7640.84	12274.12	6098.77	8301.23
Max	10030.99	19895.81	19895.81	15753.06	12096.90
Avg	7562.66	12617.15	14899.43	10047.50	10174.33

Appendix 3C. Minimum, maximum and average elastic modulus of layer 5 by core direction

	Vertical	Horizontal	Diagonal all cores	Diagonal 2:1 cores
N	8	8	9	4
Min	7967.24	15822.43	9093.99	9093.99
Max	13615.41	21324.66	19831.11	15427.50
Avg	11882.08	17333.90	13484.74	10981.34

Appendix 3D. Minimum, maximum and average elastic modulus of layer 6 by core direction

	Vertical	Horizontal	Diagonal
N	12	15	9
Min	5952.54	11176.67	11689.90
Max	18226.03	33567.82	31449.51
Avg	11725.91	21217.20	17967.58

Appendix 4. BTS results

Appendix 4A. Minimum, maximum and average BTS by layer

	All samples	Layer 4	Layer 5	Layer 6
N	103	32	34	37
Min	1.94	1.94	2.73	2.76
Max	10.03	7.32	7.08	10.03
Average	5.46	4.03	5.15	6.98

Appendix 4B. Minimum, maximum and average BTS of layer 4 by loading direction in relation to bedding

	Vertical	Horizontal (bedding II)	Horizontal (bedding =)	Diagonal (bedding II)	Diagonal (bedding =)
N	11	4	4	6	7
Min	2.97	3.10	1.94	2.50	3.36
Max	6.28	5.76	4.02	7.32	5.21
Average	4.12	4.25	2.73	4.23	4.32

Appendix 4C. Minimum, maximum and average BTS of layer 5 by loading direction in relation to bedding

	Vertical	Horizontal (bedding II)	Horizontal (bedding =)	Diagonal (bedding II)	Diagonal (bedding =)
N	5	9	9	5	6
Min	4.09	3.43	3.49	4.46	2.73
Max	6.57	7.08	6.55	6.92	5.61
Average	5.28	4.87	5.29	5.58	4.87

Appendix 4D. Minimum, maximum and average BTS of layer 6 by loading direction in relation to bedding

	Vertical	Horizontal (bedding II)	Horizontal (bedding =)	Diagonal (bedding II)	Diagonal (bedding =)
N	9	6	7	7	8
Min	2.76	5.97	5.32	4.27	3.32
Max	9.57	8.73	10.03	9.26	9.58
Average	5.53	7.69	7.28	7.87	7.03

Appendix 5. Average CERCHAR pin wear by sampling site

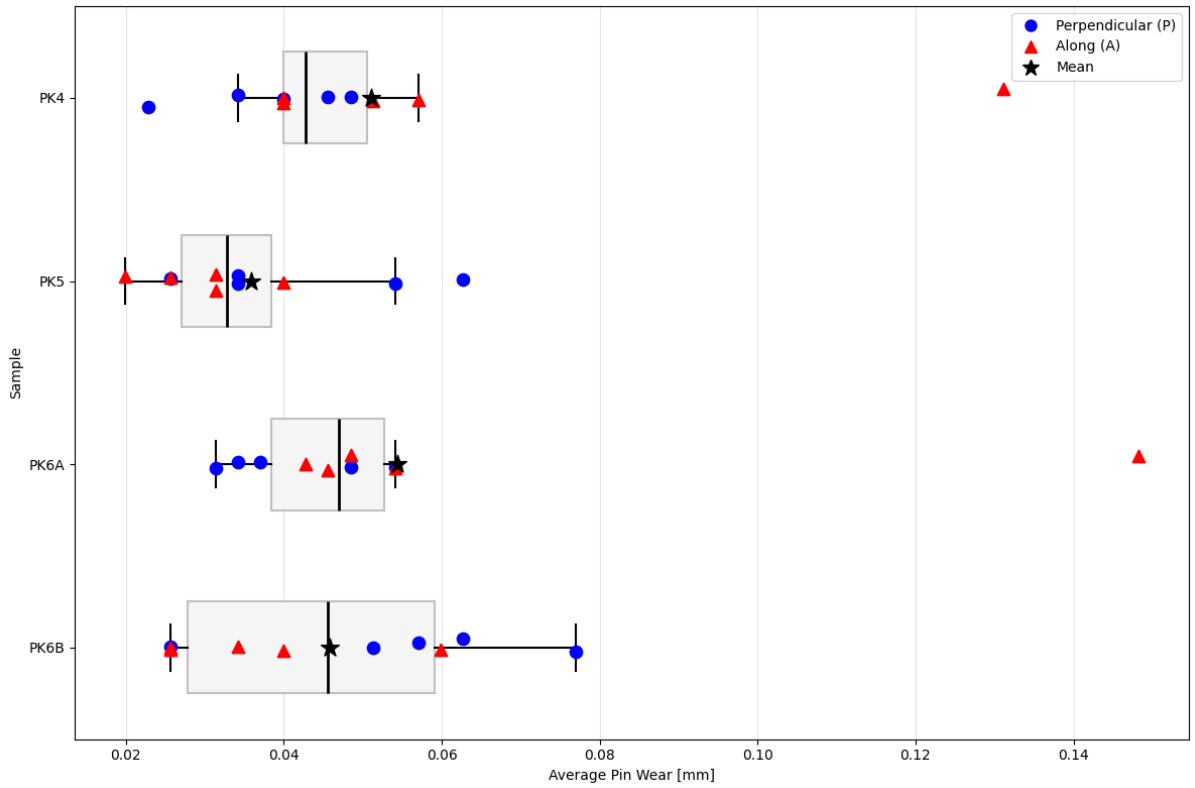

Appendix 6. Raw UCS and BTS test results

Number	Parent core	Layer	Sample site	Core direction	Sample ID	Type	Diameter (mm)	Length (mm)	Stress (MPa)	Elastic modulus (MPa)	BTS bedding orientation	Notes
1	SR25_PK4_10H	4	4	H	SR25_PK4_10H_UCS1	UCS	54	54.2	43.33	7640.84		1:1 core
2	SR25_PK4_10H	4	4	H	SR25_PK4_10H_BTS1	BTS	54.1	27.1	2.63	511.22	=	
3	SR25_PK4_10H	4	4	H	SR25_PK4_10H_BTS2	BTS	54.1	27.0	2.34	681.65	=	
4	SR25_PK4_11H	4	4	H	SR25_PK4_11H_UCS1	UCS	54	108.3	58.82	19895.81		
5	SR25_PK4_11H	4	4	H	SR25_PK4_11H_UCS2	UCS	54	54.4	50.68	12709.97		1:1 core
6	SR25_PK4_11H	4	4	H	SR25_PK4_11H_BTS1	BTS	54.0	27.0	4.10	972.56	II	
7	SR25_PK4_12H	4	4	H	SR25_PK4_12H_UCS1	UCS	53.9	108.6	29.48	13089.43		
8	SR25_PK4_12H	4	4	H	SR25_PK4_12H_UCS2	UCS	53.9	54.1	27.82	8450.96		1:1 core
9	SR25_PK4_13V	4	4	V	SR25_PK4_13V_UCS1	UCS	53.9	108.4	39.82	8951.05		
10	SR25_PK4_13V	4	4	V	SR25_PK4_13V_BTS1	BTS	54.1	27.1	3.76	536.59	II	
11	SR25_PK4_14H	4	4	H	SR25_PK4_14H_UCS1	UCS	54	54.2	62.80	14909.49		1:1 core
12	SR25_PK4_14H	4	4	H	SR25_PK4_14H_BTS1	BTS	54.0	27.1	4.05	1611	II	
13	SR25_PK4_14H	4	4	H	SR25_PK4_14H_BTS2	BTS	54.0	26.9	4.02	1186.69	=	
14	SR25_PK4_16D	4	4	D	SR25_PK4_16D_UCS1	UCS	53.9	54.3	43.90	15753.06		1:1 core
15	SR25_PK4_16D	4	4	D	SR25_PK4_16D_BTS1	BTS	54.1	26.8	2.50	745.45	II	
16	SR25_PK4_16D	4	4	D	SR25_PK4_16D_BTS2	BTS	54.1	27.0	4.00	1261.01	=	
17	SR25_PK4_17D	4	4	D	SR25_PK4_17D_UCS1	UCS	53.9	108.4	50.67	9398.22		
18	SR25_PK4_19D	4	4	D	SR25_PK4_19D_UCS1	UCS	54.1	108.6	29.68	8301.23		
19	SR25_PK4_1V	4	4	V	SR25_PK4_1V_UCS1	UCS	53.9	108.9	35.00	5869.03		
20	SR25_PK4_1V	4	4	V	SR25_PK4_1V_BTS1	BTS	54.1	27.0	2.97	896.19	II	
21	SR25_PK4_20D	4	4	D	SR25_PK4_20D_UCS1	UCS	54	54.4	40.75	6629.81		1:1 core
22	SR25_PK4_21D	4	4	D	SR25_PK4_21D_UCS1	UCS	54	54.1	62.70	11074.22		1:1 core
23	SR25_PK4_21D	4	4	D	SR25_PK4_21D_BTS1	BTS	54.0	27.1	3.93	877.95	II	
24	SR25_PK4_22D	4	4	D	SR25_PK4_22D_UCS1	UCS	54	54.4	42.64	6098.77		1:1 core
25	SR25_PK4_22D	4	4	D	SR25_PK4_22D_BTS1	BTS	54.1	27.0	3.15	1102.65	II	

Number	Parent core	Layer	Sample site	Core direction	Sample ID	Type	Diameter (mm)	Length (mm)	Stress (MPa)	Elastic modulus (Mpa)	BTS bedding orientation	Notes
26	SR25_PK4_23D	4	4	D	SR25_PK4_23D_BTS1	BTS	54.0	27.1	4.10	1652.97	=	
27	SR25_PK4_23D	4	4	D	SR25_PK4_23D_BTS2	BTS	54.1	27.1	3.36	624.86	=	
28	SR25_PK4_23D	4	4	D	SR25_PK4_23D_BTS3	BTS	54.1	27.2	3.71	957.52	II	
29	SR25_PK4_24D	4	4	D	SR25_PK4_24D_BTS1	BTS	54.0	27.0	5.21	1276.68	=	
30	SR25_PK4_24D	4	4	D	SR25_PK4_24D_BTS2	BTS	54.0	27.2	4.49	790.72	=	
31	SR25_PK4_24D	4	4	D	SR25_PK4_24D_BTS3	BTS	54.0	27.4	7.32	1560.82	II	
32	SR25_PK4_25D	4	4	D	SR25_PK4_25D_UCS1	UCS	54	108.6	35.37	12096.9		
33	SR25_PK4_26H	4	4	H	SR25_PK4_26H_UCS1	UCS	54	108.5	37.30	12274.12		
34	SR25_PK4_26H	4	4	H	SR25_PK4_26H_UCS2	UCS	54	54.3	41.78	10245.41		1:1 core
35	SR25_PK4_27D	4	4	D	SR25_PK4_27D_UCS1	UCS	54	108.3	45.05	9524.53		
36	SR25_PK4_28D	4	4	D	SR25_PK4_28D_UCS1	UCS	54	108.5	31.71	11550.77		
37	SR25_PK4_29D	4	4	D	SR25_PK4_29D_BTS1	BTS	54.1	27.0	4.77	1678.77	II	
38	SR25_PK4_29D	4	4	D	SR25_PK4_29D_BTS2	BTS	54.1	27.0	4.22	916.64	=	
39	SR25_PK4_29D	4	4	D	SR25_PK4_29D_BTS3	BTS	54.1	27.2	4.82	1265.93	=	
40	SR25_PK4_2V	4	4	V	SR25_PK4_2V_BTS1	BTS	54	27.1	3.19	857.75	II	
41	SR25_PK4_2V	4	4	V	SR25_PK4_2V_BTS2	BTS	54	26.8	6.28	1557.81	II	
42	SR25_PK4_2V	4	4	V	SR25_PK4_2V_BTS3	BTS	54	26.9	3.31	988.39	II	
43	SR25_PK4_2V	4	4	V	SR25_PK4_2V_BTS4	BTS	54.1	27.1	5.66	1519.43	II	
44	SR25_PK4_31H	4	4	H	SR25_PK4_31H_BTS1	BTS	54.1	27.2	1.94	2045.35	=	
45	SR25_PK4_31H	4	4	H	SR25_PK4_31H_BTS2	BTS	54.1	27.1	3.10	1041.38	II	
46	SR25_PK4_32V	4	4	V	SR25_PK4_32V_UCS1	UCS	53.9	108.6	38.34	8314.56		
47	SR25_PK4_33V	4	4	V	SR25_PK4_33V_UCS1	UCS	53.9	108.6	32.33	7109.11		
48	SR25_PK4_34V	4	4	V	SR25_PK4_34V_UCS1	UCS	53.9	108.7	33.64	8042.1		
49	SR25_PK4_35V	4	4	V	SR25_PK4_35V_UCS1	UCS	54	108.2	45.28	8395.72		
50	SR25_PK4_36V	4	4	V	SR25_PK4_36V_UCS1	UCS	54	108.2	33.19	7423.49		
51	SR25_PK4_3V	4	4	V	SR25_PK4_3V_UCS1	UCS	54	108.1	43.69	6445		
52	SR25_PK4_4V	4	4	V	SR25_PK4_4V_UCS1	UCS	54	107.7	54.96	10030.99		

Number	Parent core	Layer	Sample site	Core direction	Sample ID	Type	Diameter (mm)	Length (mm)	Stress (MPa)	Elastic modulus (MPa)	BTS bedding orientation	Notes
53	SR25_PK4_4V	4	4	V	SR25_PK4_4V_BTS1	BTS	54.1	27.4	4.17	1326.54	II	
54	SR25_PK4_5V	4	4	V	SR25_PK4_5V_UCS1	UCS	54	108.4	33.60	8217.28		
55	SR25_PK4_6V	4	4	V	SR25_PK4_6V_UCS1	UCS	54	108.4	40.56	7770.53		
56	SR25_PK4_6V	4	4	V	SR25_PK4_6V_BTS1	BTS	54.1	27.1	3.41	872.46	II	
57	SR25_PK4_7V	4	4	V	SR25_PK4_7V_UCS1	UCS	54	108.8	30.12	4842.49		
58	SR25_PK4_7V	4	4	V	SR25_PK4_7V_BTS1	BTS	54.1	27.2	6.22	1457.22	II	
59	SR25_PK4_7V	4	4	V	SR25_PK4_7V_BTS2	BTS	54.1	27.0	3.11	851.95	II	
60	SR25_PK4_8V	4	4	V	SR25_PK4_8V_UCS1	UCS	54	108.7	36.48	6903.25		
61	SR25_PK4_8V	4	4	V	SR25_PK4_8V_BTS1	BTS	54.1	27.0	3.20	1022.44	II	
62	SR25_PK4_9H	4	4	H	SR25_PK4_9H_UCS1	UCS	54	108.5	38.47	14338.34		
63	SR25_PK4_9H	4	4	H	SR25_PK4_9H_BTS1	BTS	54.1	27.1	5.76	1415.65	II	
64	SR25_PK5_10V	5	5	V	SR25_PK5_10V_UCS1	UCS	53.9	108.3	53.92	13320.09		
65	SR25_PK5_11V	5	5	V	SR25_PK5_11V_UCS1	UCS	53.9	108.4	48.08	12591		
66	SR25_PK5_12V	5	5	V	SR25_PK5_12V_UCS1	UCS	53.9	108.3	49.18	12276.23		
67	SR25_PK5_13D	5	5	D	SR25_PK5_13D_BTS1	BTS	54	27.0	6.92	1617.78	II	
68	SR25_PK5_13D	5	5	D	SR25_PK5_13D_BTS2	BTS	53.9	27.0	4.80	1453.68	=	
69	SR25_PK5_14D	5	5	D	SR25_PK5_14D_UCS1	UCS	53.9	108.3	43.25	9093.99		
70	SR25_PK5_15D	5	5	D	SR25_PK5_15D_BTS1	BTS	53.9	27.1	4.46	1092.72	II	
71	SR25_PK5_15D	5	5	D	SR25_PK5_15D_BTS2	BTS	54	27.2	5.57	1428.6	=	
72	SR25_PK5_16D	5	5	D	SR25_PK5_16D_UCS1	UCS	53.9	54.1	69.87	13252.65		1:1 core
73	SR25_PK5_16D	5	5	D	SR25_PK5_16D_UCS2	UCS	54	54.1	70.10	14872.32		1:1 core
74	SR25_PK5_17D	5	5	D	SR25_PK5_17D_UCS1	UCS	54	108.6	46.08	9299.05		
75	SR25_PK5_17D	5	5	D	SR25_PK5_17D_UCS2	UCS	54	54.3	60.11	13371.21		1:1 core
76	SR25_PK5_18D	5	5	D	SR25_PK5_18D_UCS1	UCS	54	54.3	62.59	16110		1:1 core
77	SR25_PK5_18D	5	5	D	SR25_PK5_18D_BTS1	BTS	54	27.1	5.27	1527.96	=	
78	SR25_PK5_18D	5	5	D	SR25_PK5_18D_BTS2	BTS	54	27.0	6.07	1565.56	II	
79	SR25_PK5_19D	5	5	D	SR25_PK5_19D_UCS1	UCS	54	54.4	65.81	19831.11		1:1 core

Number	Parent core	Layer	Sample site	Core direction	Sample ID	Type	Diameter (mm)	Length (mm)	Stress (MPa)	Elastic modulus (MPa)	BTS bedding orientation	Notes
80	SR25_PK5_19D	5	5	D	SR25_PK5_19D_BTS1	BTS	54	27.0	2.73	796.68	=	
81	SR25_PK5_1H	5	5	H	SR25_PK5_1H_UCS1	UCS	54	108.3	58.72	16019.41		
82	SR25_PK5_20D	5	5	D	SR25_PK5_20D_UCS1	UCS	54	108.6	57.40	15427.5		
83	SR25_PK5_21D	5	5	D	SR25_PK5_21D_UCS1	UCS	54	108.5	50.53	10104.81		
84	SR25_PK5_22H	5	5	H	SR25_PK5_22H_UCS1	UCS	54	108.5	55.53	16124.32		
85	SR25_PK5_23H	5	5	H	SR25_PK5_23H_BTS1	BTS	54.1	27.4	6.21	2252.29	II	
86	SR25_PK5_23H	5	5	H	SR25_PK5_23H_BTS2	BTS	54	27.0	5.20	1258.48	II	
87	SR25_PK5_23H	5	5	H	SR25_PK5_23H_BTS3	BTS	54.1	27.0	5.48	1363.17	=	
88	SR25_PK5_23H	5	5	H	SR25_PK5_23H_BTS4	BTS	54	27.2	5.91	761.64	=	
89	SR25_PK5_24V	5	5	V	SR25_PK5_24V_BTS1	BTS	54	26.8	6.57	1650.28	II	
90	SR25_PK5_24V	5	5	V	SR25_PK5_24V_BTS2	BTS	54	27.1	6.04	1720.31	II	
91	SR25_PK5_24V	5	5	V	SR25_PK5_24V_BTS3	BTS	54.1	27.0	4.63	1163.43	II	
92	SR25_PK5_24V	5	5	V	SR25_PK5_24V_BTS4	BTS	54.1	27.0	4.09	1119.86	II	
93	SR25_PK5_25V	5	5	V	SR25_PK5_25V_UCS1	UCS	54.1	108.6	66.10	13615.41		
94	SR25_PK5_26V	5	5	V	SR25_PK5_26V_UCS1	UCS	54	108.5	37.60	7967.24		
95	SR25_PK5_27H	5	5	H	SR25_PK5_27H_UCS1	UCS	54	108.5	48.73	16030.4		
96	SR25_PK5_28H	5	5	H	SR25_PK5_28H_UCS1	UCS	54	108.8	75.88	15935.76		
97	SR25_PK5_28H	5	5	H	SR25_PK5_28H_BTS1	BTS	54.1	27.1	5.79	1645.25	=	
98	SR25_PK5_29H	5	5	H	SR25_PK5_29H_UCS1	UCS	54	108.6	51.96	15822.43		
99	SR25_PK5_29H	5	5	H	SR25_PK5_29H_BTS1	BTS	54.1	27.0	5.80	1688.4	II	
100	SR25_PK5_29H	5	5	H	SR25_PK5_29H_BTS2	BTS	54.1	27.1	5.02	1126.52	=	
101	SR25_PK5_2H	5	5	H	SR25_PK5_2H_BTS1	BTS	54	27.2	3.60	1287.05	II	
102	SR25_PK5_2H	5	5	H	SR25_PK5_2H_BTS2	BTS	54	27.3	4.30	1495.84	=	
103	SR25_PK5_2H	5	5	H	SR25_PK5_2H_BTS3	BTS	54	27.1	6.55	1365.76	=	
104	SR25_PK5_30H	5	5	H	SR25_PK5_30H_BTS1	BTS	54	27.2	3.54	1173.6	II	
105	SR25_PK5_30H	5	5	H	SR25_PK5_30H_BTS2	BTS	54.1	27.2	3.49	697.05	=	
106	SR25_PK5_30H	5	5	H	SR25_PK5_30H_BTS4	BTS	54.1	27.2	3.43	805.48	II	

Number	Parent core	Layer	Sample site	Core direction	Sample ID	Type	Diameter (mm)	Length (mm)	Stress (MPa)	Elastic modulus (MPa)	BTS bedding orientation	Notes
107	SR25_PK5_31H	5	5	H	SR25_PK5_31H_UCS1	UCS	54.1	108.5	75.47	21324.66		
108	SR25_PK5_31H	5	5	H	SR25_PK5_31H_BTS2	BTS	54.1	27.2	4.65	1456.05	II	
109	SR25_PK5_32D	5	5	D	SR25_PK5_32D_BTS1	BTS	54.2	27.1	4.65	2126.2	II	
110	SR25_PK5_33D	5	5	D	SR25_PK5_33D_BTS1	BTS	54.0	26.8	5.81	2355.73	II	
111	SR25_PK5_34D	5	5	D	SR25_PK5_34D_BTS1	BTS	54.1	27.2	5.27	1259.51	=	
112	SR25_PK5_35D	5	5	D	SR25_PK5_35D_BTS1	BTS	54.1	27.4	5.61	973.79	=	
113	SR25_PK5_3H	5	5	H	SR25_PK5_3H_UCS1	UCS	53.9	108.4	57.50	20395.84		
114	SR25_PK5_3H	5	5	H	SR25_PK5_3H_BTS1	BTS	54	27	7.08	2526.43	II	
115	SR25_PK5_4H	5	5	H	SR25_PK5_4H_UCS1	UCS	53.9	108.3	48.73	17018.41		
116	SR25_PK5_6H	5	5	H	SR25_PK5_6H_BTS1	BTS	54.1	27.2	6.22	1729.62	=	
117	SR25_PK5_6H	5	5	H	SR25_PK5_6H_BTS3	BTS	54.1	27.2	4.81	986.57	=	
118	SR25_PK5_7V	5	5	V	SR25_PK5_7V_UCS1	UCS	54	108.6	65.87	12585.71		
119	SR25_PK5_7V	5	5	V	SR25_PK5_7V_BTS1	BTS	54	27.0	5.06	1555.45	II	
120	SR25_PK5_8V	5	5	V	SR25_PK5_8V_UCS1	UCS	54	108.6	60.35	11810.56		
121	SR25_PK5_9V	5	5	V	SR25_PK5_9V_UCS1	UCS	53.9	108.4	61.81	10890.41		
122	SR25_PK6_11H	6	6A	H	SR25_PK6_11H_UCS1	UCS	54	110	86.52	11231.79		
123	SR25_PK6_11H	6	6A	H	SR25_PK6_11H_BTS1	BTS	54	27.1	8.51	1502.2	II	
124	SR25_PK6_12H	6	6A	H	SR25_PK6_12H_UCS1	UCS	54	109.8	65.73	19865.32		
125	SR25_PK6_12H	6	6A	H	SR25_PK6_12H_BTS1	BTS	54	27.0	5.97	1821.15	II	
126	SR25_PK6_12H	6	6A	H	SR25_PK6_12H_BTS2	BTS	54	27.2	6.44	1006.36	=	
127	SR25_PK6_13H	6	6A	H	SR25_PK6_13H_UCS1	UCS	54	109.6	78.52	13549.31		
128	SR25_PK6_13H	6	6A	H	SR25_PK6_13H_BTS1	BTS	54	27.1	7.95	1906.52	II	
129	SR25_PK6_13H	6	6A	H	SR25_PK6_13H_BTS2	BTS	54	27.1	7.40	1928.96	=	
130	SR25_PK6_14H	6	6A	H	SR25_PK6_14H_UCS1	UCS	54	110.1	70.85	22147.53		
131	SR25_PK6_14H	6	6A	H	SR25_PK6_14H_BTS1	BTS	54	27.0	10.03	1252.04	=	
132	SR25_PK6_15H	6	6A	H	SR25_PK6_15H_UCS1	UCS	54	109.9	57.27	12259.66		
133	SR25_PK6_15H	6	6A	H	SR25_PK6_15H_BTS1	BTS	54	27.2	6.61	1403.57	=	

Number	Parent core	Layer	Sample site	Core direction	Sample ID	Type	Diameter (mm)	Length (mm)	Stress (MPa)	Elastic modulus (MPa)	BTS bedding orientation	Notes
134	SR25_PK6_16H	6	6A	H	SR25_PK6_16H_UCS1	UCS	54	110.0	40.52	11176.67		
135	SR25_PK6_16H	6	6A	H	SR25_PK6_16H_BTS1	BTS	54	27.1	6.68	2082.6	II	
136	SR25_PK6_16H	6	6A	H	SR25_PK6_16H_BTS2	BTS	54	27.2	6.49	1455.63	=	
137	SR25_PK6_17H	6	6A	H	SR25_PK6_17H_UCS1	UCS	53.9	109.7	97.49	20212.08		
138	SR25_PK6_17H	6	6A	H	SR25_PK6_17H_BTS1	BTS	54	27.0	8.32	1575.98	II	
139	SR25_PK6A_18V	6	6A	V	SR25_PK6A_18V_UCS1	UCS	54	109.6	66.50	18226.03		
140	SR25_PK6A_18V	6	6A	V	SR25_PK6A_18V_BTS1	BTS	54	27.2	2.76	743.15	II	
141	SR25_PK6A_19V	6	6A	V	SR25_PK6A_19V_UCS1	UCS	54.1	109.8	30.03	6234.56		
142	SR25_PK6A_20V	6	6A	V	SR25_PK6A_20V_UCS1	UCS	54	109.2	57.46	14897.65		
143	SR25_PK6A_21V	6	6A	V	SR25_PK6A_21V_UCS1	UCS	54	109.5	63.11	10966.16		
144	SR25_PK6A_22V	6	6A	V	SR25_PK6A_22V_UCS1	UCS	54	108.9	56.40	8459.79		
145	SR25_PK6A_23V	6	6A	V	SR25_PK6A_23V_UCS1	UCS	54	109.3	53.62	14151.65		
146	SR25_PK6A_24V	6	6A	V	SR25_PK6A_24V_UCS1	UCS	54	109.2	51.08	5952.54		
147	SR25_PK6A_25V	6	6A	V	SR25_PK6A_25V_UCS1	UCS	54	109.0	52.10	13534.86		
148	SR25_PK6A_26V	6	6A	V	SR25_PK6A_26V_UCS1	UCS	54.1	108.9	40.02	10664.35		
149	SR25_PK6A_28D	6	6A	D	SR25_PK6A_28D_UCS1	UCS	54	108.9	76.02	31449.51		
150	SR25_PK6A_28D	6	6A	D	SR25_PK6A_28D_BTS1	BTS	54.1	27.0	8.17	962.2	=	
151	SR25_PK6A_29D	6	6A	D	SR25_PK6A_29D_UCS1	UCS	54	109.0	84.40	16522.99		
152	SR25_PK6A_29D	6	6A	D	SR25_PK6A_29D_BTS1	BTS	54.1	27.2	4.05	624.83	=	
153	SR25_PK6A_30D	6	6A	D	SR25_PK6A_30D_UCS1	UCS	53.9	108.6	80.86	11689.9		
154	SR25_PK6A_30D	6	6A	D	SR25_PK6A_30D_BTS1	BTS	54	27.2	8.60	1934.91	II	
155	SR25_PK6A_32V	6	6A	V	SR25_PK6A_32V_UCS1	UCS	54	107.9	46.25	14538.37		
156	SR25_PK6A_32V	6	6A	V	SR25_PK6A_32V_BTS1	BTS	54	27.8	6.83	2318.23	II	
157	SR25_PK6A_33V	6	6A	V	SR25_PK6A_33V_UCS1	UCS	54	108.7	72.54	15784.11		
158	SR25_PK6A_33V	6	6A	V	SR25_PK6A_33V_BTS1	BTS	54	27.1	3.49	400.82	II	
159	SR25_PK6A_34V	6	6A	V	SR25_PK6A_34V_BTS1	BTS	54	27.2	7.57	1813.74	II	
160	SR25_PK6A_34V	6	6A	V	SR25_PK6A_34V_BTS2	BTS	54	26.9	5.42	921.81	II	

Number	Parent core	Layer	Sample site	Core direction	Sample ID	Type	Diameter (mm)	Length (mm)	Stress (MPa)	Elastic modulus (MPa)	BTS bedding orientation	Notes
161	SR25_PK6A_34V	6	6A	V	SR25_PK6A_34V_BTS3	BTS	54	27.0	3.39	1060.81	II	
162	SR25_PK6A_35V	6	6A	V	SR25_PK6A_35V_BTS1	BTS	54	26.8	5.96	1536.34	II	
163	SR25_PK6A_35V	6	6A	V	SR25_PK6A_35V_BTS2	BTS	54	27.1	4.76	1005.37	II	
164	SR25_PK6A_35V	6	6A	V	SR25_PK6A_35V_BTS3	BTS	54	27.2	9.57	1946.03	II	
165	SR25_PK6A_36V	6	6A	V	SR25_PK6A_36V_UCS1	UCS	54	108.3	43.28	7300.86		
166	SR25_PK6B_10H	6	6B	H	SR25_PK6B_10H_UCS1	UCS	54	110.1	43.59	12080.83		
167	SR25_PK6B_10H	6	6B	H	SR25_PK6B_10H_BTS1	BTS	54	27.1	5.32	1941.77	=	
168	SR25_PK6B_1D	6	6B	D	SR25_PK6B_1D_BTS1	BTS	54	27.1	4.27	926.81	II	
169	SR25_PK6B_1D	6	6B	D	SR25_PK6B_1D_BTS2	BTS	53.9	27.0	5.96	702.16	=	
170	SR25_PK6B_27H	6	6B	H	SR25_PK6B_27H_UCS1	UCS	54	108.9	103.97	33567.82		
171	SR25_PK6B_2D	6	6B	D	SR25_PK6B_2D_UCS1	UCS	54	108.6	60.10	16036.36		
172	SR25_PK6B_2D	6	6B	D	SR25_PK6B_2D_BTS1	BTS	54	27.1	7.93	2416.13	II	
173	SR25_PK6B_2D	6	6B	D	SR25_PK6B_2D_BTS2	BTS	54	27.1	7.11	834.56	=	
174	SR25_PK6B_37H	6	6B	H	SR25_PK6B_37H_UCS1	UCS	54	108.6	83.04	30616.09		
175	SR25_PK6B_38H	6	6B	H	SR25_PK6B_38H_UCS1	UCS	54.1	108.5	103.86	28782.82		
176	SR25_PK6B_38H	6	6B	H	SR25_PK6B_38H_BTS1	BTS	54.1	27.0	8.73	1848.21	II	
177	SR25_PK6B_39H	6	6B	H	SR25_PK6B_39H_UCS1	UCS	54	107.9	49.52	17066.88		
178	SR25_PK6B_3D	6	6B	D	SR25_PK6B_3D_UCS1	UCS	54	108.4	60.72	15372.34		
179	SR25_PK6B_40H	6	6B	H	SR25_PK6B_40H_UCS1	UCS	54	108.5	97.20	29516.93		
180	SR25_PK6B_41H	6	6B	H	SR25_PK6B_41H_UCS1	UCS	54	108.9	98.69	26016.11		
181	SR25_PK6B_42H	6	6B	H	SR25_PK6B_42H_UCS1	UCS	54	108.7	98.10	30168.11		
182	SR25_PK6B_42H	6	6B	H	SR25_PK6B_42H_BTS1	BTS	54	27.0	8.64	1556.52	=	
183	SR25_PK6B_4D	6	6B	D	SR25_PK6B_4D_UCS1	UCS	53.9	108.5	56.80	12981.28		
184	SR25_PK6B_5D	6	6B	D	SR25_PK6B_5D_UCS1	UCS	54	110.3	73.36	20665.82		
185	SR25_PK6B_5D	6	6B	D	SR25_PK6B_5D_BTS1	BTS	54.1	27	9.27	3067.01	=	
186	SR25_PK6B_6D	6	6B	D	SR25_PK6B_6D_BTS1	BTS	54.1	26.9	9.26	1460.48	II	
187	SR25_PK6B_6D	6	6B	D	SR25_PK6B_6D_BTS2	BTS	54.1	27.1	9.58	1824.38	=	

Number	Parent core	Layer	Sample site	Core direction	Sample ID	Type	Diameter (mm)	Length (mm)	Stress (MPa)	Elastic modulus (MPa)	BTS bedding orientation	Notes
188	SR25_PK6B_6D	6	6B	D	SR25_PK6B_6D_BTS3	BTS	54.1	27.4	9.16	1384.41	II	
189	SR25_PK6B_7D	6	6B	D	SR25_PK6B_7D_BTS1	BTS	54	27.2	3.32	1493.67	=	
190	SR25_PK6B_7D	6	6B	D	SR25_PK6B_7D_BTS2	BTS	54.1	27	8.39	1451.57	II	
191	SR25_PK6B_7D	6	6B	D	SR25_PK6B_7D_BTS3	BTS	54	27.2	8.77	1439.2	=	
192	SR25_PK6B_8D	6	6B	D	SR25_PK6B_8D_UCS1	UCS	54	110.1	40.69	14840.52		
193	SR25_PK6B_8D	6	6B	D	SR25_PK6B_8D_BTS1	BTS	54.1	27.2	7.45	1643.85	II	
194	SR25_PK6B_9D	6	6B	D	SR25_PK6B_9D_UCS1	UCS	54	109.7	65.64	22149.47		

Appendix 8. Raw CERCHAR pin measurements

Sample	Direction	Pin	Image	Viewing angle	Wear flat diameter (mm)	Corrected wear flat	Average pin wear	CAI
PK4	P	P_1	A	0	0.04	0.0456	0.0456	0.38
			B	90	0.04	0.0456		
			C	180	0.04	0.0456		
			D	270	0.04	0.0456		
PK4	P	P_2	A	0	0.02	0.0228	0.0228	
			B	90	0.02	0.0228		
			C	180	0.02	0.0228		
			D	270	0.02	0.0228		
PK4	P	P_3	A	0	0.04	0.0456	0.04845	
			B	90	0.04	0.0456		
			C	180	0.05	0.057		
			D	270	0.04	0.0456		
PK4	P	P_4	A	0	0.03	0.0342	0.0342	
			B	90	0.03	0.0342		
			C	180	0.03	0.0342		
			D	270	0.03	0.0342		
PK4	P	P_5	A	0	0.03	0.0342	0.0399	
			B	90	0.04	0.0456		
			C	180	0.03	0.0342		
			D	270	0.04	0.0456		
PK4	A	A_1	A	0	0.03	0.0342	0.0399	0.64
			B	90	0.03	0.0342		
			C	180	0.04	0.0456		
			D	270	0.04	0.0456		
PK4	A	A_2	A	0	0.03	0.0342	0.0399	
			B	90	0.04	0.0456		
			C	180	0.03	0.0342		
			D	270	0.04	0.0456		
PK4	A	A_3	A	0	0.11	0.1254	0.1311	
			B	90	0.1	0.114		
			C	180	0.12	0.1368		
			D	270	0.13	0.1482		
PK4	A	A_4	A	0	0.04	0.0456	0.0513	
			B	90	0.05	0.057		
			C	180	0.04	0.0456		
			D	270	0.05	0.057		
PK4	A	A_5	A	0	0.05	0.057	0.057	
			B	90	0.05	0.057		
			C	180	0.05	0.057		
			D	270	0.05	0.057		

Sample	Direction	Pin	Image	Viewing angle	Wear flat diameter (mm)	Corrected wear flat	Average pin wear	CAI
PK5	P	P_1	A	0	0.05	0.057	0.0627	0.42
			B	90	0.06	0.0684		
			C	180	0.05	0.057		
			D	270	0.06	0.0684		
PK5	P	P_2	A	0	0.05	0.057	0.05415	
			B	90	0.05	0.057		
			C	180	0.04	0.0456		
			D	270	0.05	0.057		
PK5	P	P_3	A	0	0.03	0.0342	0.0342	
			B	90	0.03	0.0342		
			C	180	0.03	0.0342		
			D	270	0.03	0.0342		
PK5	P	P_4	A	0	0.02	0.0228	0.02565	
			B	90	0.02	0.0228		
			C	180	0.02	0.0228		
			D	270	0.03	0.0342		
PK5	P	P_5	A	0	0.03	0.0342	0.0342	
			B	90	0.03	0.0342		
			C	180	0.03	0.0342		
			D	270	0.03	0.0342		
PK5	A	A_1	A	0	0.02	0.0228	0.03135	0.30
			B	90	0.03	0.0342		
			C	180	0.03	0.0342		
			D	270	0.03	0.0342		
PK5	A	A_2	A	0	0.02	0.0228	0.03135	
			B	90	0.03	0.0342		
			C	180	0.03	0.0342		
			D	270	0.03	0.0342		
PK5	A	A_3	A	0	0.02	0.0228	0.02565	
			B	90	0.02	0.0228		
			C	180	0.02	0.0228		
			D	270	0.03	0.0342		
PK5	A	A_4	A	0	0.03	0.0342	0.0399	
			B	90	0.03	0.0342		
			C	180	0.04	0.0456		
			D	270	0.04	0.0456		
PK5	A	A_5	A	0	0.02	0.0228	0.01995	
			B	90	0.02	0.0228		
			C	180	0.02	0.0228		
			D	270	0.01	0.0114		

Sample	Direction	Pin	Image	Viewing angle	Wear flat diameter (mm)	Corrected wear flat	Average pin wear	CAI
PK6A	P	P_1	A	0	0.03	0.0342	0.03705	0.41
			B	90	0.04	0.0456		
			C	180	0.03	0.0342		
			D	270	0.03	0.0342		
PK6A	P	P_2	A	0	0.03	0.0342	0.03135	
			B	90	0.03	0.0342		
			C	180	0.03	0.0342		
			D	270	0.02	0.0228		
PK6A	P	P_3	A	0	0.05	0.057	0.05415	
			B	90	0.05	0.057		
			C	180	0.05	0.057		
			D	270	0.04	0.0456		
PK6A	P	P_4	A	0	0.03	0.0342	0.0342	
			B	90	0.03	0.0342		
			C	180	0.03	0.0342		
			D	270	0.03	0.0342		
PK6A	P	P_5	A	0	0.04	0.0456	0.04845	
			B	90	0.04	0.0456		
			C	180	0.05	0.057		
			D	270	0.04	0.0456		
PK6A	A	A_1	A	0	0.04	0.0456	0.04845	0.68
			B	90	0.04	0.0456		
			C	180	0.04	0.0456		
			D	270	0.05	0.057		
PK6A	A	A_2	A	0	0.05	0.057	0.05415	
			B	90	0.04	0.0456		
			C	180	0.05	0.057		
			D	270	0.05	0.057		
PK6A	A	A_3	A	0	0.03	0.0342	0.04275	
			B	90	0.04	0.0456		
			C	180	0.04	0.0456		
			D	270	0.04	0.0456		
PK6A	A	A_4	A	0	0.13	0.1482	0.1482	
			B	90	0.13	0.1482		
			C	180	0.13	0.1482		
			D	270	0.13	0.1482		
PK6A	A	A_5	A	0	0.04	0.0456	0.0456	
			B	90	0.04	0.0456		
			C	180	0.04	0.0456		
			D	270	0.04	0.0456		

Sample	Direction	Pin	Image	Viewing angle	Wear flat diameter (mm)	Corrected wear flat	Average pin wear	CAI
PK6B	P	P_1	A	0	0.02	0.0228	0.02565	0.55
			B	90	0.03	0.0342		
			C	180	0.02	0.0228		
			D	270	0.02	0.0228		
PK6B	P	P_2	A	0	0.06	0.0684	0.07695	
			B	90	0.07	0.0798		
			C	180	0.07	0.0798		
			D	270	0.07	0.0798		
PK6B	P	P_3	A	0	0.04	0.0456	0.0513	
			B	90	0.05	0.057		
			C	180	0.05	0.057		
			D	270	0.04	0.0456		
PK6B	P	P_4	A	0	0.05	0.057	0.0627	
			B	90	0.06	0.0684		
			C	180	0.05	0.057		
			D	270	0.06	0.0684		
PK6B	P	P_5	A	0	0.05	0.057	0.057	
			B	90	0.06	0.0684		
			C	180	0.04	0.0456		
			D	270	0.05	0.057		
PK6B	A	A_1	A	0	0.05	0.057	0.05985	0.37
			B	90	0.05	0.057		
			C	180	0.05	0.057		
			D	270	0.06	0.0684		
PK6B	A	A_2	A	0	0.02	0.0228	0.02565	
			B	90	0.02	0.0228		
			C	180	0.02	0.0228		
			D	270	0.03	0.0342		
PK6B	A	A_3	A	0	0.03	0.0342	0.0342	
			B	90	0.03	0.0342		
			C	180	0.03	0.0342		
			D	270	0.03	0.0342		
PK6B	A	A_4	A	0	0.03	0.0342	0.0399	
			B	90	0.04	0.0456		
			C	180	0.03	0.0342		
			D	270	0.04	0.0456		
PK6B	A	A_5	A	0	0.02	0.0228	0.02565	
			B	90	0.03	0.0342		
			C	180	0.02	0.0228		
			D	270	0.02	0.0228		

Appendix 9. Raw Poisson's ratio results

Sample ID	Layer	Core direction	Signal Velocity (m/s)	Poisson Ratio
SR25_PK4_1V_UCS1	4	V	3428	0.21
SR25_PK4_9H_UCS1	4	H	4291	0.22
SR25_PK4_12H_UCS1	4	H	3460	0.30
SR25_PK4_13V_UCS1	4	V	3114	0.20
SR25_PK4_17D_UCS1	4	D	3964	0.23
SR25_PK4_19D_UCS1	4	D	3079	0.13
SR25_PK4_26H_UCS1	4	H	4360	0.33
SR25_PK4_27D_UCS1	4	D	3586	0.25
SR25_PK4_34V_UCS1	4	V	3206	0.22
SR25_PK5_1H_UCS1	5	H	4395	0.35
SR25_PK5_3H_UCS1	5	H	4561	0.23
SR25_PK5_10V_UCS1	5	V	3528	0.26
SR25_PK5_12V_UCS1	5	V	3586	0.13
SR25_PK5_14D_UCS1	5	D	3658	0.21
SR25_PK5_17D_UCS1	5	D	3586	0.24
SR25_PK5_20D_UCS1	5	D	3785	0.19
SR25_PK5_25V_UCS1	5	V	3586	0.16
SR25_PK5_27H_UCS1	5	H	4291	0.22
SR25_PK6A_17H_UCS1	6	H	4844	0.26
SR25_PK6A_18V_UCS1	6	V	4486	0.24
SR25_PK6A_20V_UCS1	6	V	4395	0.21
SR25_PK6A_24V_UCS1	6	V	3907	0.22
SR25_PK6A_28D_UCS1	6	D	4658	0.23
SR25_PK6B_4D_UCS1	6	D	4760	0.27
SR25_PK6B_5D_UCS1	6	D	4658	0.26
SR25_PK6B_27H_UCS1	6	H	5000	0.25
SR25_PK6B_40H_UCS1	6	H	4888	0.24

Lihtlitsents lõputöö reprodutseerimiseks ja lõputöö üldsusele kättesaadavaks tegemiseks[1]

Mina, Siim Roov

1. Annan Tallinna Tehnikaülikoolile tasuta loa (lihtlitsentsi) enda loodud teose

"Estimation of cutting feasibility on the example of Põhja-Kiviõli II mine",

mille juhendaja on Bruno Grafe,

1.1 reprodutseerimiseks lõputöö säilitamise ja elektroonse avaldamise eesmärgil, sh Tallinna Tehnikaülikooli raamatukogu digikogusse lisamise eesmärgil kuni autoriõiguse kehtivuse tähtaja lõppemiseni;

1.2 üldsusele kättesaadavaks tegemiseks Tallinna Tehnikaülikooli veebikeskkonna kaudu, sealhulgas Tallinna Tehnikaülikooli raamatukogu digikogu kaudu kuni autoriõiguse kehtivuse tähtaja lõppemiseni.

2. Olen teadlik, et käesoleva lihtlitsentsi punktis 1 nimetatud õigused jäävad alles ka autorile.

3. Kinnitan, et lihtlitsentsi andmisega ei rikuta teiste isikute intellektuaalomandi ega isikuandmete kaitse seadusest ning muudest õigusaktidest tulenevaid õigusi.

/allkirjastatud digitaalselt/ 25.05.2026

[1] *Lihtlitsents ei kehti juurdepääsupiirangu kehtivuse ajal vastavalt üliõpilase taotlusele lõputööle juurdepääsupiirangu kehtestamiseks, mis on allkirjastatud teaduskonna dekaani poolt, välja arvatud ülikooli õigus lõputööd reprodutseerida üksnes säilitamise eesmärgil. Kui lõputöö on loonud kaks või enam isikut oma ühise loomingulise tegevusega ning lõputöö kaas- või ühisautor(id) ei ole andnud lõputööd kaitsvale üliõpilasele kindlaksmääratud tähtajaks nõusolekut lõputöö reprodutseerimiseks ja avalikustamiseks vastavalt lihtlitsentsi punktidele 1.1. jq 1.2, siis lihtlitsents nimetatud tähtaja jooksul ei kehti.*